MODELLING AND FORECASTING OF CLIMATE VARIABILITY IMPACT ON SPATIO-TEMPORAL DISTRIBUTION OF STREAM FLOW IN NJORO RIVER CATCHMENT, KENYA

OTIENO EDWIN AMISI

A Thesis Submitted to the Graduate School in Partial Fulfillment of the Requirements for Master of Science Degree in Agricultural Engineering of Egerton University

EGERTON UNIVERSITY

NOVEMBER 2021

DECLARATION AND RECOMMENDATION

Declaration

This thesis is my original work and has not been presented for the award of a degree in Egerton University or any other institution.

Signature..... Date 02/11/2021

Otieno Edwin Amisi

BM11/17513/17

Recommendation

This thesis has been submitted for examination with our recommendation and approval as University supervisors.

Signature..... Date 02/11/2021

Dr. Peter M. Kundu

Department of Agricultural Engineering,

Egerton University

Signature..... Date 02/11/2021

Dr. Raphael M. Wambua

Department of Agricultural Engineering,

Egerton University

2024/1165 26

COPYRIGHT

DEDICATION

This work is dedicated to God the Almighty who is the source of my life. To my mother Dina Amisi, dearest well-wisher Mr. Steve Cochran, Mr. Gillis and Willis Onyango for continuous prayers, inspiration, support, encouragement, mentorship, love, and guidance.

ACKNOWLEDGEMENTS

My entire Master of Science (MSc) study would not have been possible without the will of Almighty God. I take this prerogative to express my humble gratitude to God for life, grace, and love. My profound appreciation also extends to Egerton University for the opportunity and learning resources provided to me by the Department of Agricultural Engineering to attain this academic objective. It is my greatest privilege to thank my supervisors Dr. Peter M. Kundu and Dr. Raphael M. Wambua for the acceptance, guidance, enthusiastic mentorship, consistent effort, inspiration, and a marvellous sense of humour for the completion of this work.

I also appreciate a lot of support from the staff of the faculty of Engineering and Technology. I acknowledge the Center of Excellence in Agriculture and Agribusiness Management (CESAAM) for financing my study. My heartfelt indebtedness also goes to Mr. Steve Cochran, Mr. Gillis, and Christs' Gift Academy for the financial support and unending aspiration. Finally yet importantly, my sincere thanks to my mother, brothers, and sisters for their support, prayers, and encouragement for the entire period.

ABSTRACT

Climate variability continues to alter hydrological regimes and response of many catchments globally thus threatening water security. Njoro River catchment has not been an exception, there is a steady recognition of climate variability adverse influences like deterioration of ecosystems, surface and groundwater sources. Therefore, the study focused on modelling and forecasting the impact of climate variability on spatial and temporal distribution of stream flow in Njoro River catchment, Kenya. Trends in climate variables from Egerton University weather station (ID: 09035092) were first analysed by the use of Mann-Kendall test for the period (1978 -2017). Then, modelling of stream flow response to climate variability using SWAT was carried out based on USGS/NASA downloaded Digital Elevation Model, FAO soil data, Landsat (MSS 1-5) LULC of 1978, and meteorological data for the period (1978 - 2017). Simulation of spatial and temporal impacts of climate variability then followed, and finally, a hybrid modelling technique of coupling SWAT and ANN models were then applied to forecast climate variability impact on stream flow for the period (2018-2037). Trend results for the period (1978-2017) showed that annual precipitation had a positive trend that was not significant at $p < 0.05$. Solar radiation, maximum and minimum temperatures had significant positive trends. Relative humidity had a negative trend that was not significant. Wind speed had a significant decreasing trend. Based on SWAT modelling, the most sensitive parameter was CN2 while the least was CANMX. Overall uncertainty analysis results indicated a good model performance value of P-factor (0.72) and R-factor (0.38). The values of R^2, NSE, and PBIAS for calibration and validation of monthly stream flow using observed data from Water Resources Authority were 0.88 and 0.77, 0.86 and 0.74, and 5.51 % and -15.42 % respectively. Spatio-temporal impacts of climate variability on stream flow revealed that on average, stream flow reduced by 30.91 % in the 2nd and increased by 5.47 % and 63.63 % in the 3rd and 4th decades respectively. The annual average temperatures and precipitation were forecasted to increase from the baseline values by about 0.6 ^{0}C and 18.99 %, and 0.85 ^{0}C and 28.26 %, respectively for the period (2018 - 2027), and (2028 - 2037). From the SWAT and ANN coupling approach, the forecasting stream flow model indicated an overall better performance of ($R^2 = 0.92$) and (NSE = 0.89). The average annual stream flow was forecasted to increase from the baseline values by about 83 % and 130 % for the periods (2018-2027) and (2028-2037) respectively. These findings provide pertinent insights, which may perhaps enlighten decision-making in designing adaptable mitigation measures, catchment rehabilitation, and strategic initiatives for the integrated management of water resources.

TABLE OF CONTENT

LIST OF TABLES

LIST OF FIGURES

LIST OF SYMBOLS

Symbol	Description
b	Bias at the cell body
CH_4	Methane
CO_2	Carbon dioxide
$f(x)$	Gamma function
$g(x)$	Gamma distribution
m	Number of hidden neurons
n	Number of input neurons
Wi	Weight attached to the input signal i
Xi	An input vector
R^2	Coefficient of Determination
α	Significance level
p	Probability values
$r\_$	Substitution of a parameter by a value
$v\_$	Relative change in a parameter
95PPU	95 % prediction boundary
f (.)	Activation function
NSE	Nash Sutcliffe model efficiency
PCPSKW(mon)	Skew coefficient for daily precipitation in all months
PR_W(1,mon)	Probability of a wet day following a dry day in the month
PR_W(2,mon)	Probability of a wet day following a wet day in a month
Sim	Simulation
CV(t-p)	Feedback delay
H_2O	Water vapour
Z_c	Calculated standard normal distribution test statistics

LIST OF ABBREVIATIONS AND ACRONYMNS

Abbreviation/Acronym	Description
ACCO	Adaptive Clustering Covering
AET	Actual Evapotranspiration
ANN	Artificial Neural Network
ARIMA	Autoregressive Integrated Moving Average
DEM	Digital Elevation Model
ENSO	El Niño Southern Oscillation
EPA	Environmental Protection Agency
ETM+	Enhanced Thematic Mapper Plus
FAO	Food and Agricultural Organization
GA	General Algorithm
GCM	General Circulation Model
GWQ	Groundwater flow
HadRM3	Hadley Centre Regional Climate Model 3
HRU	Hydrologic Response Unit
IPCC	Intergovernmental Panel on Climate Change
ITCZ	Inter-Tropical Convergence Zone
KWS	Kenya Wildlife Service
LATQ	Lateral flow
LULC	Land Use/Land Cover
MSS	Multi-Spectral Scanner
NAR	Nonlinear Autoregressive
NARX	Nonlinear Autoregressive with External (Exogenous)
NASA	National Aeronautics and Space Administration
NCAR	National Center for Atmospheric Research
NCDC	National Climate Data Center
NOAA	National Oceanic and Atmospheric Administration
PARASOL	Parameter Solution
PBIAS	Percentage Bias
PET	Potential Evapotranspiration
PPU	Percentage Prediction Uncertainty
PRECIS	Providing Regional Climates for Impacts Studies

RCM	Regional Climate Model
SCS-CN	Soil Conservation Service Curve Number
SRES	Special Report on Emissions Scenarios
SRTM	Shuttle Radar Topography Mission
SUFI-2	Sequential Uncertainty Fitting 2
SURQ	Surface Runoff
SDG	Sustainable Development Goal
SWAT	Soil and Water Assessment Tool
SWAT-CUP	SWAT Calibration and Uncertainty Programs
TM	Thematic Mapper
UNEP	United Nations Environmental Program
UNFCCC	United Nations Framework Convention on Climate Change
USGS	United State Geological Survey
UTM	Universal Transverse Mercator
WLYD	Water Yield
WMO	World Meteorological Organisation

CHAPTER ONE
INTRODUCTION

1.1 Background Information

Water is an indispensable, finite, and vital resource in all aspects of life (IPCC, 2012; Kılıç, 2020; Loucks & Van Beek, 2017). It is a key ingredient for ecosystem existence, and a major catalyst necessary for socio-economic development, and human productivity (Brown & Lall, 2006; Yıldız, 2017). However, the management of freshwater resources as pointed out by Benson et al. (2015), Murshed and Kaluarachchi (2018), USGS, U.S. EPA, NCAR, NCDC, FAO, NOAA, WMO, IPCC, and UNEP is becoming problematic. For instance, Liebscher (2009) and Hendriks (2015) elucidate that the water scarcity warning issued at the last years of 20th century has turn out to be a reality to the level of inadequate supply in most cases, which now adversely affects food security. Besides, the absolute water scarcity (a supply less than 500 m^3 per capita annually) in most of the counties in Kenya, has contributed to several conflicts, and livestock succumb to extreme hydrologic events yearly (Ochieng et al., 2016).

Many organisations (UNEP, IPCC, UNFCCC, and WMO) and researchers like Mwetu (2010), Rwigi et al. (2016), and Zhang et al. (2016) attribute the aforementioned challenges to uncertainties of environmental human interference and climate variability. The two factors as pointed out by Folland et al. (2002), IPCC (2013), and Simonovic (2017) alters the regional water cycle, hydrologic regime, and stream flow response of the catchments. Such alterations in the hydrologic processes are problematic because changes in climate and land-use system impacts operate at different temporal as well as spatial scales (Renner et al., 2014). Furthermore, the effect of land-use change and climate variability might compensate, strengthens each other, or occur in parallel (Bao et al., 2012; Tomer & Schilling, 2009). For example, Kingston and Taylor (2010), assert that disasters from climate-related natural phenomena are aggravated by other factors such as industrialization, unsustainable farming practices, and deforestation.

Climate variability has been associated with increased emission of greenhouse gases in the atmosphere according to Crowley (2000), IPCC (2007), and Allen et al. (2014). It influences changes in several components of the hydrologic system. These changes include unreliable precipitation patterns, extreme heat waves, variation of both surface and groundwater flows, soil moisture level, and changes in atmospheric water content (IPCC, 2013; Xu et al. 2013). Impacts of climate variability materialize through changes in precipitation partitioning into a

drastic increase or decline in hydrologic variables, thus, higher stream flow variability (Charlton & Arnell, 2011; Mwetu, 2010). Like the rest of the world, Njoro River catchment of Kenya is not an exception to these dynamics (Baldyga, 2005; Kundu, 2007; Mwetu, 2010; Wambua et al., 2008). For instance, in Njoro River catchment, there is a study recognition of increased water stress periods, progressive decline in surface and groundwater sources, and drying up of boreholes as well as water pans. River Njoro experiences a drastic decline in stream flow and it tends to change from permanent to seasonal along the watercourse.

The Njoro River catchment depend largely on climate-sensitive economic drivers that make food security, freshwater, and rural livelihoods exceedingly vulnerable to shifts in water availability. Therefore, a catchment monitoring initiative under integrated water resource management is of utmost importance since it is the best way for the implementation of Sustainable Development Goals (SDG No: 1, 2, 3, 6, and 13). Proper management of stream flows improves the availability of water for agricultural as well as domestic use, which then can significantly reduce the poverty levels and address Vision 2030 pillars. Moreover, UNFCCC (2005), UNEP (2009), and the environmental sector of the Vision 2030 social pillar of Kenya agitate for continuous studies to provide knowledge on how the changing climatic conditions and increasing demands on freshwater are expected to impact the available water resources.

The separation of climate variability effects from that of LULC impacts on stream flow enhances greater understanding of the catchment hydrologic processes and creation of sound water resources management strategies (Arnell & Delaney, 2006). Therefore, the study focused on modelling and forecasting the impact of climate variability on spatial and temporal distribution of stream flow in Njoro River catchment. It was accomplished by determining state of the climate, modelling stream flow response to climate variability using the Soil and Water Assessment Tool. Finally, forecasting temperature, precipitation, and stream flow using artificial neural networks in conjunction with the SWAT model.

1.2 Statement of the Problem

River Njoro originates from Mau hills which is one of the water towers in Kenya. Changes in hydrological and catchment regimes within such a water tour often result in heightened tensions among various water users especially in the event of reduced flows. The continued degradation due to the effects of land-use changes and climate variability influences the surface, subsurface, and groundwater systems, and this may eventually escalate conflicts over the water resources.

Njoro River catchment experiences reduced water yield, droughts, flash floods, and extended water stress periods causing a progressive decline in stream flow. Currently, River Njoro tends to exhibit a characteristic shift from perennial to ephemeral along the watercourse. Water resources adequacy in the catchment is becoming a matter of concern and a bigger challenge mostly during water stress periods. In response to these challenges, few studies (Baldyga, 2005; Kundu, 2007; Mwetu, 2010; Otieno & Ogalo, 2012) that have been conducted in the recent past focused mostly on LULC impacts. There is scanty quantifiable information on the response of stream flow both spatially and temporally to climate variability in the Njoro River catchment. Besides, modelling future scenarios of climate variability impact on stream flow is still a knowledge gap, thus, the need to develop appropriate forecasting techniques.

1.3 Objectives

1.3.1 Broad Objective

The broad objective of this study was to model and forecast the impact of climate variability on the spatial and temporal distribution of stream flow in Njoro River catchment of Kenya.

1.3.2 Specific Objectives

The specific objectives were to:

i) Determine trends of climate variables in Njoro River catchment from 1978 to 2017.
ii) Model stream flow response to climate variability using SWAT for the period 1978 to 2017.
iii) Simulate spatial and temporal impacts of climate variability on stream flow for the period (1978 - 2017).
iv) Forecast impact of climate variability on stream flow from 2018 to 2037 by coupling SWAT and Artificial Neural Networks.

1.4 Research Questions

i) How were the trends of climate variables in Njoro River catchment from 1978 to 2017?
ii) How is the response of stream flow to climate variability?
iii) How did climate variability affect stream flow spatially and temporally for the period (1978 - 2017)
iv) How will climate variability affect stream flow in future climatic scenarios of the period 2018 to 2037?

1.5 Justification

The impact of the changing climatic patterns on water resources sometimes can be complex and highly uncertain, since climate variability has the potential to influence the relatively stable climate to a precarious situation and jeopardize the security of energy, food, and water. Njoro River catchment water resources support a larger society and therefore, any influence on its capacity to sustain the livelihoods and socio-economic activities is of major concern. Therefore, trend analysis of climate variables is necessary for climate state assessment and provides estimates about the variations in the climate variables for accurate hydrologic modelling and forecasting. Hydrologic modelling provides information for environmental management, addressing socio-economic issues that include water excess, stress, security, and scarcity. Estimating climate variability impacts provides useful insights and data products for decision support in conjunctive water use, catchment rehabilitation, monitoring, and management. Forecasting enables the creation of a design criterion for integrated water resources management plans, thus, reducing cost of water security projects and rationally save lives. In addition, it plays a major role in measures targeting sustainability and optimization of water resources use, design of hydraulic structures, and any future water demand prediction.

1.6 Scope and Limitations of the Study

The study was carried out in Njoro River catchment and climate variables considered were from 1978 and 2017. SWAT and ANN were applied models for simulation, forecasting, and defining how hydrologic variables respond to climate variability. Hydrologic variables were simulated using the LULC of 1978 for the entire period. Hydrologic modelling was limited to the upper Njoro River catchment because of the challenges of the availability and discrepancies in hydro-climatic data in most of the weather stations and river gauging stations within Njoro River catchment. Simulated stream flow was considered to have the similar statistical attributes as the measured data, and changes in stream flow in upper Njoro River catchment were applicable to the entire Njoro River catchment.

1.7 Definition of Terms

Artificial Neural Network	A data driven process with adaptable mathematical algorithm or a similitude of the biological nervous system capable of solving complex nonlinear relationships.
Climate	The statistical description in terms of the variability as well as mean of relevant variables or average weather over a duration ranging from weeks to millions years.
Climate variability	Variation of the occurrence of extremes and standard deviations or in the mean state of the climate at all spatio-temporal scales beyond weather events.
Climate variability impact	The long-term effects or consequences of variations in the climate that last longer than individual weather events.
Forecasting	Prediction of the future states of the phenomenon, system or quantity, based on knowledge of current and past states of the system or quantity, often computed with the aid of a model.
Greenhouse gases	Are those gaseous constituents of the atmosphere, which absorb and emit radiation at specific wavelengths within the spectrum of thermal infrared radiation emitted by the Earth's surface.
Land cover	The surface cover on the ground, whether vegetation, urban infrastructure, water, bare soil or other.
Land use	The purpose the land serves, for example, recreation, wildlife habitat, or agriculture.
Soil and Water Assessment Tool	A basin-scale semi-distributed deterministic hydrologic model designed to simulate the flow of water, agricultural chemical yields, crop growth, and sediments in a watershed.
Stream flow	The channel runoff from land to water bodies, and is a major element of the water cycle.

CHAPTER TWO
LITERATURE REVIEW

2.1 Climate

Climate is the state, including a statistical description in terms of the variability as well as mean of relevant quantities over a duration extending from months to million years of the climate system (IPCC, 2012). According to the World Meteorological Organization, the classical duration for averaging these quantities is thirty years. The special fifth assessment report by IPCC (2014) explains that climate variables include surface quantities such as solar radiation, wind speed, precipitation, temperature, and relative humidity. In Kenya, some of the studies such as Mcsweeney et al. (2010), Nicholson (2017), and Ongoma et al. (2018) point out that three types of climate exist besides the country being bisected by the Equator. Namely, humid and hot along the coast, temperate in the south-west and west where there are mountains and plateaus, and hot and dry in the east and north. This implies that the climate in Kenya is generally tropical, but moderated by diverse topography in the west (Camberlin, 2018).

The wider altitudinal range from mean sea levels at the coast to mountains in the central and western region is a characteristic of the given geographical location of strong elevation gradients, which in effect influences the climate of a particular locality. For instance, Nicholson (2002) reports that the regions along the coast have higher temperatures (warmer) than the central highlands with the highest altitude areas at 29.0 ^{0}C compared with 15.0 ^{0}C at the highlands. Additionally, in Rift Valley, the average surface air temperature decrease from about 29 ^{0}C in the north to just over 16 ^{0}C around lakes Naivasha and Nakuru in the south, and with average temperatures ranging between 13 and 18 ^{0}C. The adjacent highlands are generally moderate (Camberlin, 2018; Nicholson, 2002). Nevertheless, surface air temperature in Kenya varies little throughout the year, where the coolest period is from July to August, while the warmest season is from January to March.

Studies like Kerandi et al. (2017), Mcsweeney et al. (2010), and Camberlin (2018) illustrate that seasonal precipitation in Kenya is driven mainly by the migration of the Inter-Tropical Convergence Zone. Nevertheless, Nicholson (2017) explains that the migration of ITCZ is always accompanied by a shift in the wind direction in a southerly direction in boreal summer form a northerly direction in boreal winter, which is characteristic of the monsoons. Therefore, both precipitation and temperature vary according to the predominant winds that yield two seasons. The wind movements change the exact location of the ITCZ over the year, migrating

southwards through Kenya from October to December, and returning northwards in March, April, and May (Camberlin, 2018).

ITCZ movements through Kenya cause two different wet periods in Kenya; the long rains in March to May and the short rains in September to December (Camberlin, 2018; Mcsweeney et al., 2010). From year to year, the onset, intensity, and duration of precipitation vary substantially and are irregular because of the changing global climatic patterns since the movements of ITCZ are so sensitive to variations in Indian Ocean sea-surface temperatures. El Niño Southern Oscillation (ENSO) is one of the most well documented ocean influences on precipitation in Eastern Africa region. El Niño occurrences contribute to greater precipitation in the short rainfall season (SON), whilst cold phases (La Niña) bring a drier than average season (Mcsweeney et al., 2010).

2.2 Climate Variability

IPCC's special report (2012) describes climate variability as variations in the other statistics (like the occurrence of extreme hydrological events, standard deviation) and mean climate state at all Spatio-temporal scales beyond that of weather events. IPCC (2007) explains that these are changes that occur within smaller timeframes, such as a decade, year, season, or months. Unlike climate variability, climate change refers to the state of the climate that can be detected statistically by variations in the mean of its properties and that persists for a longer duration normally decades. The interactions between the components of climate system (atmosphere, land surface, biosphere, and hydrosphere) and external forces like solar variations, volcanic eruptions, and persistent human-induced factors continue to change the climate system (Zarrin, 2018). Variability is attributed to changes in anthropogenic or natural external forcing or natural internal processes within the climate system (Verma, 2020).

2.2.1 Factors Contributing to Climate Variability

Climate variability occurs as a consequence of several variables. The variables are variations in the solar energy reaching earth's surface, climate oscillations, volcanic activities, changes in Earth's orbit, and changes in the greenhouse effect, which affects the amount of heat retained by Earth's atmosphere (IPCC Fifth Assessment Report, 2014). According to NASA, the natural mechanisms continue to influence the climate even in the present day, but their impact is too small to account for the extreme weather events and rapid warming observed in recent decades. IPCC (2013) holds that the latest observed climate variability can be attributed majorly to anthropogenic activities which appear to be the significant cause. As assessed by the IPCC

shown in Figure 2.1, the factors leading to potential vulnerability to changes in climate and variability from the human-induced activities override natural contributors.

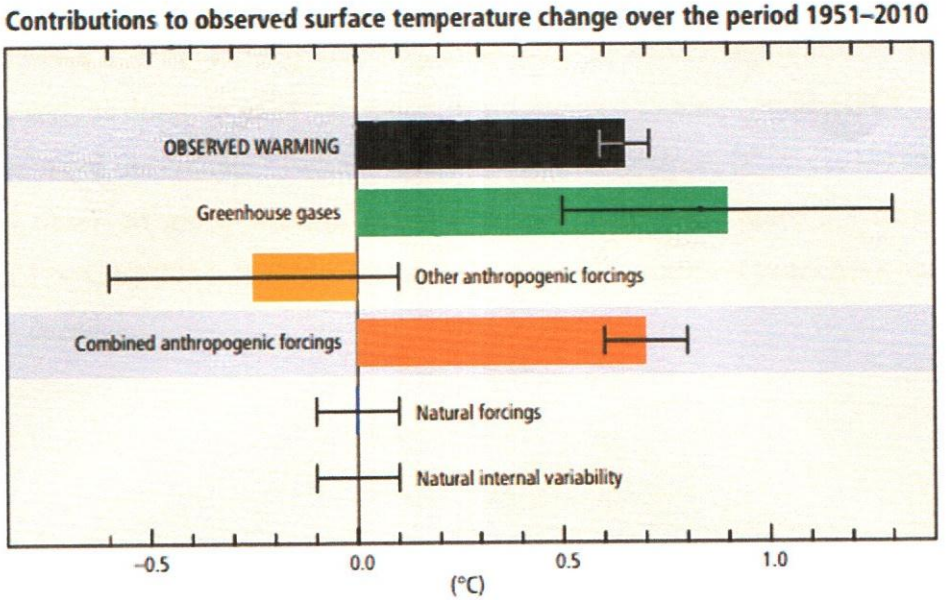

Figure 2.1: Contributors to climate variability

(Adopted from Fifth IPCC assessment report, 2014)

The greenhouse gas emissions generated specifically by humans are the primary contributors to the earth's changing climate (IPCC, 2018). Further, Skinner (2019) illustrates that greenhouse gases quantities have skyrocketed in the atmosphere. Concentrations of methane, nitrous oxides, and the Earth's leading climate change contributor CO_2 have increased to levels unprecedented since preindustrial time (Allen et al., 2014). Besides inappropriate waste management systems, poor environmental sanitation, unsustainable agricultural practices, the burning of fossil fuels for transportation, electricity, oil, coal, biogas, and heat are the major sources of human-generated emissions (Crowley, 2000). Also, it is estimated that forest degradation which includes clear-cutting, fires, and logging releases up to twenty percent of global carbon emissions due to destruction of carbon sinking zones. Industrial processes release fluorinated gases and activities like infrastructure developments aid local cooling or warming. The resulting build-up of CO_2, CH_4, fluorinated gases, and water vapour in the atmosphere absorb energy reflected from the earth's surface and preventing or limit the heat loss to space thus causing alarming fast warming worldwide what is called greenhouse effect.

2.2.2 Indicators of Climate Variability

The development of variability in climate takes a longer time, while weather can change within a few hours or minutes. There are many climate variability indicators. These entail trends in climate variables and mostly physical responses such as spatial and temporal variability in intensity as well as duration of precipitation, wind speed, and temperature (IPCC, 2007). The rate of warming of the climate system is indisputable. For instance, IPCC (2018) special report analysis on observed global surface temperatures as shown in Figure 2.2 revealed global warming of 1.5 °C by 2017. It was revealed that most of the warmest years have occurred over the last two decades.

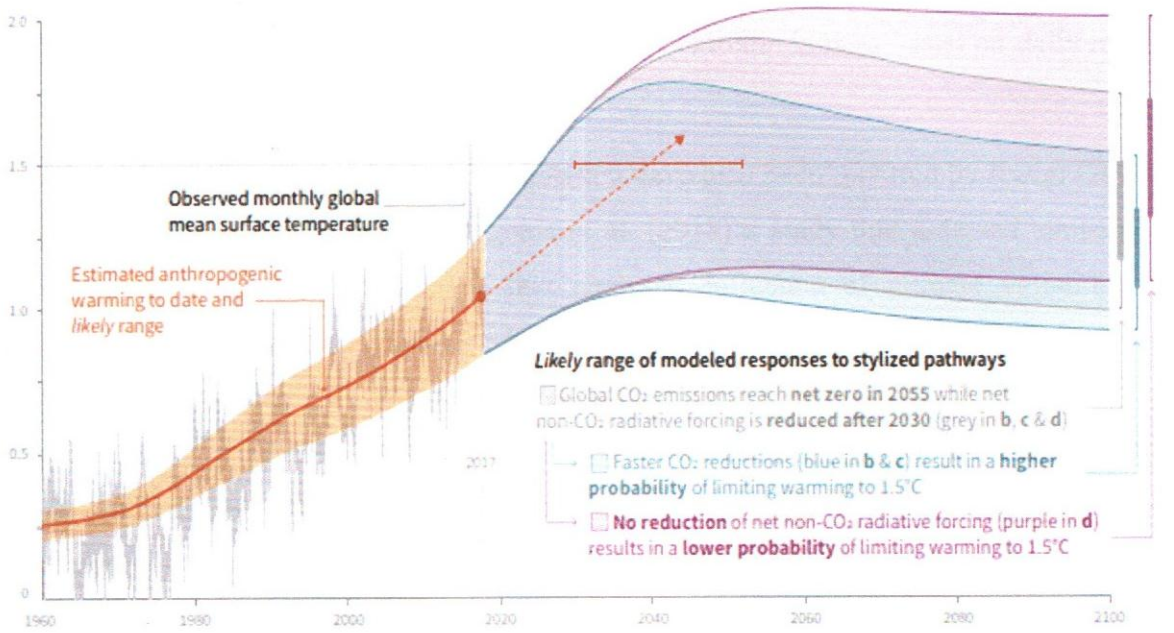

Figure 2.2: The rate of global warming relative to 1850 -1900 (^{0}C)

(Adopted from IPCC special report of 2018)

As the earth heats up, atmosphere experiences variations in movement of wind, it collects, retains, and drops more or little precipitation, altering weather occurrence and in effect increase or decrease the atmospheric capacity to hold water (Gan et al., 2016). Evapotranspiration increase may dry out some areas and retained water may fall as excess precipitation on other areas. The increase in maximum and minimum surface temperatures have been accompanied by extremes variability in precipitation in many regions. For instance, several studies reveal the positive and negative trends in precipitation in the East Africa region (Gamoyo et al., 2015; Gebrechorkos et al., 2019; New et al., 2006).

Previous research by Mcsweeney et al. (2010) found that in Kenya, annual temperature increased at an average rate of 0.21°C every ten years since 1960. The positive trend in temperature has been slowest in JJAS (0.19°C per decade) and most rapid in MAM (0.29°C per decade). Also, they report that the average number of 'hot' days annually has increased by 58 days for the period (1960 - 2003), while the average number of warmer nights increased by 114 days in the period (1960 - 2003). However, the frequency of cold nights has decreased significantly in all seasons. For instance, an average number of 'cold' nights annually has declined by 11.45% of days. This rate of decrease is most rapid in DJF season when the average number of cold DJF nights has decreased by 3.45 nights per month in the period (1960 - 2003). In their conclusion, Mcsweeney et al. (2010) stated that since 1960 precipitation trends have not been statistically significant, in that trends in the extreme indices based on daily rainfall data are mixed, and heavy events are inconsistent.

Similar trends in air temperature and precipitation have also been reported by Rwigi (2014) a study carried out in Sondu region, Ongoma et al. (2018) a study that assessed temperature trends in Kenya, and Mbote (2016) that analysed influence of climate variability on biodiversity in Lake Nakuru, Kenya. Some studies associate the current spatio-temporal precipitation variability to the increase in the intensities of floods, agricultural, and hydrological droughts (Lyon & Dewitt, 2012; Nicholson, 2017; Omondi et al., 2012). Other research such as Cubasch et al. (2013) illustrates that the higher surface air temperature is a result of greenhouse effect and depletion of ozone layer which in turn exacerbate the occurrence interval of many forms of disasters, including severe hydrological events, heat waves, storms, sea level, atmospheric water vapour deficit, land ice, and glacier.

2.3 Response of Stream flow to Climate Variability

The state of the climate is the driving force of the hydrological processes as well as the sustenance of water resources (IPCC, 2007). Climate variability, like the variations in solar energy, changes the world hydrological cycle since it alters the magnitude and frequency of precipitation, which is the primary driver of watershed processes (WMO, 2009). For instance, a warmer atmosphere escalates depletion of soil water and evaporation from the water bodies, meaning more water availability for precipitation. The atmosphere can hold around four percent more water vapour for every 0.55 ^{0}C and this may lead to intense rains and increases the risk of higher surface runoff generation and flooding of streams. Figure 2.3 shows the partitioning of precipitation and different hydrologic variables in a catchment.

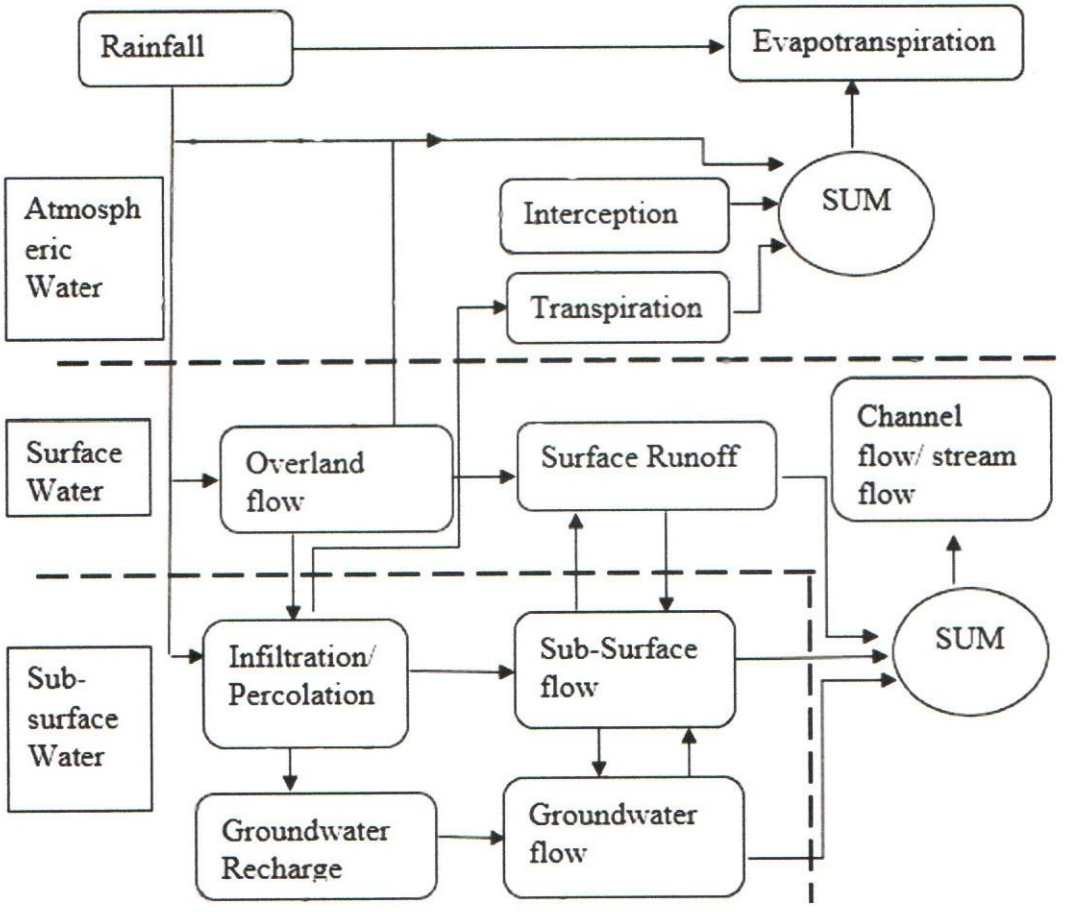

Figure 2.3: Watershed system showing hydrologic variables

It is evident from the Figure 2.3 that changes in precipitation may alter all hydrologic components of stream flow. Precipitation deficiency, drier climatic conditions, and elevated rates of evapotranspiration may exacerbate both hydrological and agricultural droughts. Persistent drought leads to reduced surface flows, subsurface flows, and groundwater flows with consequent effects of extreme decline in stream flow (Schulte et al., 2016). As shown in Figure 2.3, infiltration and percolation recharge base flow via sub-surface and groundwater storage. Where the infiltration capacity of the soil exceeds rainfall intensities, the primary mechanisms for storm water transport to streams then become interflows, which are the main component of base flow. In the event where there is little infiltration, stream flow occurs as a result of direct runoff from large storms.

Direct runoff is a result of the spikes caused by a rainstorm, which then contributes to peak flow. Besides, surface water loss and soil moisture fluctuation implications, evaporation, and transpiration reduce base flow because trees absorb water from the ground. Therefore, it is imperative to infer that the variability of climate variables (wind, precipitation, temperatures,

solar radiation, and relative humidity) causes the variation in spatial redistribution, severity, frequency, intensity, and magnitude of atmospheric, surface, sub-surface, and groundwater systems (Schulze, 2011). It means that the variations in climate have a direct influence on the surface flows, land surface energy, evapotranspiration, soil humidity, recharge of aquifers, and water yield (Milly et al., 2005). Consequently, the effects are felt in channel flows or stream flow which depend on surface runoff, lateral flows, and groundwater flow.

Although several studies have been conducted and published on the climate variability impact on hydrologic variables such as stream flow, the evidence is that some catchments experience negative trends while others have positive trends (Hagemann et al., 2013). For example, Mwangi et al. (2016) evaluated relative impact of climate variability and LULC change on stream flow of upper Mara River, Kenya. In their case, they used water-energy budget method to isolate the influence of LULC change from that of climate variability on stream flow. They found that climate variability contributed 2.5 percent of the total increment change, which was contributed by counter influence increase in potential evapotranspiration and precipitation. Their findings were consistent with studies by Mati et al. (2005) and Recha et al. (2012). A similar increasing trend in stream flow as a result of climate variability influence which encompasses the positive trends in precipitation has also been reported in some of the studies such as Githui and Mutua (2007), Mango et al. (2010), and Rwigi (2014).

Other studies that have used coupled water-energy budget technique based on the Budyko hypothesis are Tomer and Schilling (2009), Zang et al. (2012), Renner et al. (2014), and Booij et al. (2019). Though the water-energy method gives reasonable insight into climate variability's influence on stream flow, the applicability of the approach is limited. The water-energy technique is limited to account for the climate intra-annual variability that influences the quantification of surface runoff and water yield as alluded by Roderick and Farquhar (2011). It explains why Mwangi et al. (2016) recommended the application of hydrological model to compare the results obtained. According to Booij et al. (2019), the two basic assumptions of water-energy budget technique might not always be correct because changes in climate also affect actual evapotranspiration to some extent. In fact, Renner et al. (2014) found that the two assumptions might lead to an underestimation of climate variability contribution and an overestimation of the contribution of land-use change on stream flow.

Conversely, Mwetu et al. (2010) modelled response of hydrology to changes in LULC and climate variability in Njoro River catchment using SWAT. The findings according to the trend

line ($y = -1.745x + 1076.9$) used indicated a negative trend in precipitation from 1944-2004. The impact of climate variability showed a decrease of all hydrologic variables analysed between the periods (1977 - 1986) (baseline) and (1990 - 1999) climatic scenarios. The decreases were in the order of about 78 %, 62 %, 54 %, 26 %, and 17% of the total change for mean water yield, surface runoff, transmission losses, percolation, and lateral flow respectively. These findings provide useful insight into the sensitivity of Njoro River catchment to climate variability.

Mwetu's (2010) analyses provide a scenario of further exploration and future investigation of trends in changes of the hydrologic variables in Njoro River catchment due to changes in climatic patterns. For instance, to evaluate whether the negative trend in stream flow continues into the future, there would be need for at least three simulations under different climatic scenarios to be compared with the baseline climatic condition results. Again, forecasting of the stream flow changes under projected climatic scenarios would still be necessary for enriching the environment of catchment monitoring techniques. The declining trend in hydrological variables changes as a result of climate variability which involves negative trends in precipitation and positive trends in temperatures have also been reported by Zhang et al. (2016) and Omwoyo et al. (2017).

2.4 Trend Analysis of Climate Variables

Time series analysis of climate variables involves the techniques of consistency checks, estimation of missing data, and trend analysis of temporal climatic datasets to extract meaningful statistics and other characteristics of the data acquired (Shumway & Stoffer, 2017). Some of the techniques that have been applied in estimation of missing hydro-climatic datasets include inverse distance, normal ratio, linear regression, weighted arithmetic means, and spatial correlation. Out of all the methods of data consistency checks, many hydrological studies recommend the use of double mass curve approach (Gao et al., 2017; Odongo et al., 2015; Pirnia et al., 2019) because inconsistencies in a record of a particular variable can easily be detected by an apparent break in the slope of the double-mass curve.

Owing to the complexity of the interrelationship and correlation of changes in climatic patterns, and hydro-climatic variables, trend analysis is an important aspect in hydrology for the tracing of the magnitude of climate variability. Moreover, the assessments are necessary for hydrological modelling, water resources planning, and climate change impact studies. Various statistical techniques have been applied to detect the trend and shift of the trend in hydrologic

and climate variables (Gocic & Trajkovic, 2013; Jha & Singh, 2013). Out of the commonly used non-parametric and parametric approaches, the Mann–Kendall statistical test has been preferred to quantify the significance of trends in hydrologic and climate variables time series (Asfaw et al., 2018; Ongoma & Chen, 2017). This is because Mann-Kendall test accommodates missing values and outliers, and records with skewed distribution (Partal & Kahya, 2006).

2.5 Hydrologic Modelling

A hydrologic model is a simplified representation of a real system that aids simulation, prediction, understanding, planning, and management of different hydrologic variables in a particular location (Devia et al., 2015). Hydrologic modelling involves conceptual, empirical, and physical-based approaches to predict the behaviour, physical response, and hydrologic processes for a specific input like the hydro-metrological variables. The models can be classified based on inputs as well as parameters, and the extent of physical laws behind the model. Other studies such as Tricoli (2004), demonstrate that the models can further be categorized in terms of stochastic and deterministic models.

A detailed classification of the models is shown in Figure 2.4.

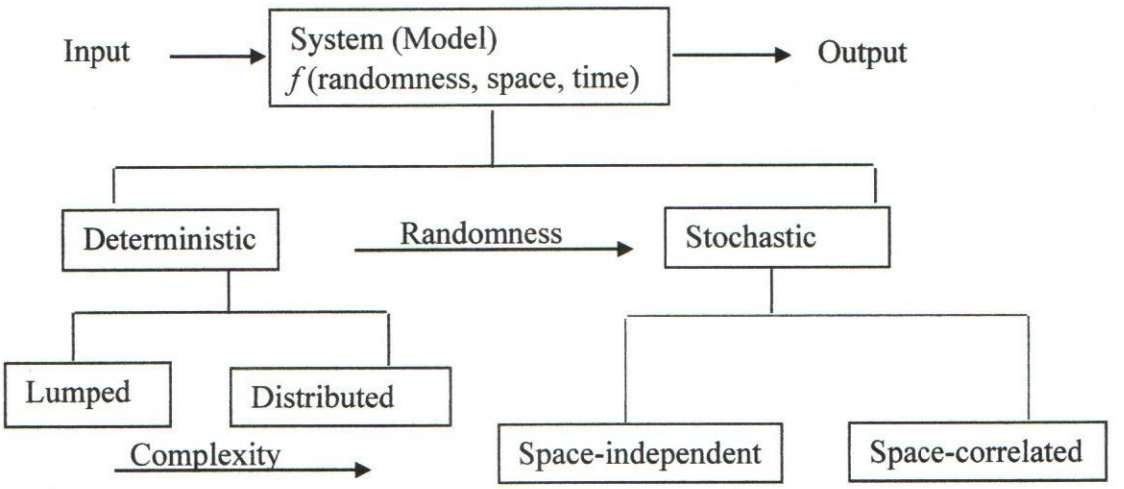

Figure 2.4: Classification of models according to how they treat the randomness and spatial variant of hydrologic phenomena.
(Modified from a study by Tricoli, 2004)

2.5.1 Stochastic Hydrologic Models

The stochastic models are widely applied in many scientific studies because they consider the occurrence of events in space and time (Azadi & Zakeri, 2010). They are mathematical models that use random variables governed by probability laws, thus classified as space independent

and space correlated. In most of the scenarios, they are used for time rainfall-runoff analysis, and their estimations have random elements. Moreover, magnitude and time of various flow processes are stochastic, whereas the movement of water in a land phase is in a deterministic path. Thus, a combination of stochastic and deterministic techniques or procedures provides an excellent modelling approach.

2.5.2 Deterministic Hydrologic Models

Deterministic hydrologic models are those that do not consider the randomness of the variables in that a particular input produces a similar output. Cunderlik (2003) categorised deterministic hydrologic models into three main categories; semi-distributed, distributed, and lumped. In the case of the lumped model, Beven (2001) illustrates that the system is regarded as a single point in space without dimensions. For example, in the case of TOPMODEL and SCS-CN based models, parameters do not represent physical features of hydrologic processes. Semi-distributed models consider input in a catchment not only to vary with time but also with space. Semi-distributed models are classified into Kinematic wave theory models, for example, HEC-HMS model (Arnold et al., 1998). Devia et al. (2015) explain that the structure of a semi–distributed model is more physically based than lumped models and less demanding on input data than distributed models, some of the examples of such models are SIMHYD, and SWAT.

In distributed models, the parameters vary in space at a resolution chosen by the user, and they require a large number of input data and hydrological records for calibration (Dingman, 2002). Additionally, they require expertise, and have higher computational time, for example, WATFLOOD, HRDROTEL, and MIKE11/SHE. Borah and Bera (2003) carried out a comparative analysis between the functionalities of SWAT, DWSM, and TOPMODEL models and found seventeen uses of SWAT among those, which include simulation of stream flow, sediment transport, impacts of changes in climate, and LULC, biomass, and channel losses. Also, they found that SWAT performance outmatched the DWSM and HSP - FORTRAN model for continuous simulations. Van et al. (2003) found that SWAT predicted stream flow better than HSPF model in estimating stream flow for different climatic conditions.

SWAT has been demonstrated to be an effective operational tool in water resource assessment at wide and small scales in various environmental conditions (Arnold et al., 2012; Mwangi et al., 2016; Mwetu, 2010). This could be so because SWAT is physically based, computationally efficient, and capable of continuous simulation over long periods. The most advantageous primary feature of the SWAT model as demonstrated by Neitsch et al. (2011) includes its ability

to perform on multiple GIS platforms like QGIS (QSWAT), Map windows (MWSWAT), and ArcGIS (ArcSWAT). Furthermore, the relative impact of alternative input data (e.g. changes in LULC and climatic scenarios) on water quantity or other variables of interest can be determined (Arnold et al., 2012; Rwigi et al., 2016; Mwetu, 2010). SWAT uses readily available inputs like climate variables, digital elevation model, soil, and land use data (Neitsch et al., 2011). The model has been applied successfully in many river basins and catchments in Kenya which include Nzoia (Githui, et al., 2009), Njoro (Mwetu, 2010), Sondu (Rwigi et al., 2016), and Mara (Mwangi et al., 2016).

The law of conservation of mass and momentum energy first proposed by St. Venant in1871 as well as several empirical relations are used in physical model development, which is fully distributed and semi-distributed. Physical modelling includes occurrence, movement, Spatio-temporal distribution, and storage of water. Physical modelling may be in 3D, 2D, or 1D. Based on requirements and data availability, overland and channel flow are the hydrodynamic modelling which is always considered by the continuity and momentum Equation 2.1 and 2.2.

$$\frac{\partial A}{\partial t}+\frac{\partial(vA)}{\partial x}-q=0\text{; Continuity equation} \tag{2.1}$$

$$\frac{\partial Q}{\partial t}+\frac{\partial(vQ)}{\partial x}+gA\left(\frac{\partial y}{\partial x}-S_0+S_f\right)=0\text{; Momentum equation} \tag{2.2}$$

The equations are applied in modelling under the assumption that the flow is unidirectional, the fluid is incompressible, vertical accelerations are negligible and hydrostatic pressure prevails. In addition, stream curvature is assumed to be small and steady uniform flow equation such as Manning's can be used to describe resistance effects. The expressions in Equation 2.3 are the terms in momentum equation.

$$g\frac{\partial y}{\partial x}-g\left(S_0-S_f\right)=0\text{; Kinematic wave} \tag{2.3a}$$

$$V\frac{\partial V}{dx}+g\frac{\partial y}{\partial x}-g\left(S_0-S_f\right)=0\text{; Diffusion wave} \tag{2.3b}$$

$$\frac{\partial V}{\partial t}+V\frac{\partial V}{dx}+g\frac{\partial y}{\partial x}-g\left(S_0-S_f\right)=0\text{; Dynamic wave} \tag{2.3c}$$

Therefore, Overland flow continuity equation can be expressed by;

$$\frac{\partial uh}{\partial x}+\frac{\partial vh}{dy}+\frac{\partial h}{\partial t}=r_e; \tag{2.4a}$$

$$r_e=r_i-f_i \tag{2.4b}$$

where, h is the depth of flow, r_e is the excess rainfall (mm), and f_i is the infiltration rate.

Momentum equation for the overland flow is given as;

$$\frac{\partial u}{\partial t}+u\frac{\partial u}{dx}+v\frac{\partial u}{\partial y}+g\frac{\partial h}{\partial x}-g\left(S_{ox}-S_{fx}\right)+r_e\frac{u}{h}=0 \tag{2.5a}$$

$$\frac{\partial v}{\partial t}+u\frac{\partial v}{dx}+v\frac{\partial v}{\partial y}+g\frac{\partial h}{dx}-g\left(S_{oy}-S_{fy}\right)+r_e\frac{v}{h}=0 \tag{2.5b}$$

where, g is the acceleration due to gravity, s_{ox} is the slope of watershed element in x direction, s_{fy} is the frictional slope in y-direction, s_{oy} is the slope in y-direction, and s_{fx} is the frictional slope in x-direction.

The equations on channel flow are given as follows;

$$\frac{\partial Q}{\partial x}+\frac{\partial(\mathrm{A})}{\partial t}-q=0\text{; Continuity equation} \tag{2.6}$$

$$\frac{\partial Q}{\partial t}+\frac{\partial}{\partial x}\frac{Q^2}{\mathrm{A}}=gA\left(S_0-S_f\right)=gA\frac{\partial h}{dx}\text{; Momentum equation} \tag{2.7}$$

With initial boundary condtions, channel/stream flow would then be expressed as;

$$Q=\frac{1}{n}R_h^{2/3}S_f^{1/2}\mathrm{A} \tag{2.8}$$

where, q is the lateral inflow, Q is the discharge in the channel (m^3/s), A is the area of flow in the channel (m^2), n is the Manning's coefficient for the channel, R_h is the hydraulic radius for a given depth of flow (m), S_0 is the bed slope (m/m), and S_f is the friction slope of channel (m/m).

2.6 Soil and Water Assessment Tool (SWAT)

SWAT is a basin-scale deterministic hydrologic model designed to simulate sediments, crop growth, hydrologic processes and variables, and agricultural chemical yields in a catchment (Douglas et al., 2010). The model runs on a daily time step and requires specific information from the input parameters about topography, soil properties, and LULC practices (Neitsch et

al., 2011). These input data are used in modelling physical processes related to nutrient cycling, crop growth, sediment, and water movement. For hydrological modelling processes, SWAT partitions a watershed into a number of sub-catchments. The sub-catchments are further subdivided into hydrologic response units. HRUs within a sub-catchment are lumped land areas that consist of unique soil, climatic condition, slope, land use, and land cover combination (Gassman et al., 2007). Modelling process using SWAT encompasses six main steps namely input data preparation, catchment delineation, hydrologic response units' definition, sensitivity analysis, calibration, validation, and uncertainty analysis.

2.6.1 Catchment Delineation and Hydrologic Response Units

SWAT uses Digital Elevation Model for the delineation of the area of interest that gives the elevation at a certain spatial resolution of precise points and this is done under the GIS platform, where drainage patterns and exploration of land surface features are derived from DEM (Neitsch et al., 2011). As demonstrated by Arnold et al. (2012), the development of physical properties of the catchment is mandatory since the direction and flow rate over the land surface are influenced by catchment's topography. Delineation is accomplished through various steps, including DEM setup, definition of stream network, inlets and outlets, catchment outlet selection, and sub-catchment parameter calculations. HRU is derived from the combination of DEM, LULC, and soil data. LULC controls hydrologic response of the sub-catchments. Soil data influence soil physical properties that in turn affects surface, subsurface transport of water, infiltration, percolation, and return flows.

2.6.2 Climate Components

Climate variables generate the energy as well as moisture inputs that control the water balance in a catchment and aid in quantification of the hydrologic variables in every HRU. SWAT requires daily precipitation, relative humidity, maximum and minimum air temperatures, solar radiation, and wind speed (Gassman et al., 2007). Daily surface air temperatures are needed for computation of daily water and soil temperatures. Precipitation data determines water balance since it is the main hydrologic cycle process via which water goes into the land phase component. The use of relative humidity, wind speed, and solar radiation in SWAT model depends entirely on the technique selected for evapotranspiration estimation.

SWAT model employs the water balance equation using the climate variables in every hydrologic response unit to estimate various hydrologic variables (Arnold et al., 1998), which is given as;

$$SW_t = SW + \sum_{i-1}^{n} \left(R_{day} - Q_i - E_a - P_i - QR_i \right) \quad (2.9)$$

where, SW is soil water content (mm), t is time (days), R_{day} is the amount of precipitation (mm) Q_i, is the amount of surface runoff (mm), E_a is the amount of evapotranspiration (mm), P is the amount of percolation (mm), and QR_i is the amount of return flow (mm).

2.6.3 Land and Routing Phase Components

According to Douglas et al. (2010), simulation of hydrologic variables in a catchment can be separated into two main categories which include the routing (water) and land phases. Land phase controls the quantity of water flow to the main channel in every hydrologic response unit. Routing phase is described as water flow through the channel networks to the catchment outlet. The hydrologic elements of the cycle comprise the routing phase of the hydrological cycle and flow processes occurring on the land and are based on the soil water balance (Equation 2.9), which forms the basis of hydrological modelling. Table 2.1 shows techniques used in SWAT for hydrologic balance simulations.

Table 2.1: Methods of determining hydrologic processes in SWAT at the HRUs

Hydrological Process	Method of Determination/ Algorithm
Canopy interception	Initial abstractions in SCS-CN equation
Surface runoff	SCS-CN method
Evapotranspiration	Penman-Monteith
Channel flow routing	Variable storage routing method
Open channel flow routing	Manning's equation
Percolation losses	Storage routing combined with a cracked flow model
Transmission losses	Lane's method
Lateral flow	Kinematic storage routing method
Recharge of groundwater	Exponential decay weighting factor
Base flow duration	Techniques of base flow and recession analysis
Groundwater routing	Groundwater storage method; re-evaporation concepts

As described in the Soil and Water Assessment Tool theoretical documentation by Neitsch et al. (2011) the following are some of the major water balance equations.

The SCS-CN method explaining the water balance equation can be expressed as;

$$Q = \frac{(P - I_a)^2}{(P - I_a) + S} \tag{2.10}$$

Where, P is the total precipitation (mm), Q is the actual Runoff (mm), S is the potential maximum retention of soil moisture after surface runoff begin and I_a is the initial abstraction (mm) which represents all losses before the runoff begins.

The Penman-Monteith form of the combination equation is:

$$\lambda ET = \frac{\Delta(R_n - G)P_a C_p \dfrac{(e_s - e_a)}{r_a}}{\Delta + \gamma\left(1 + \dfrac{r_s}{r_a}\right)} \tag{2.11}$$

where, λET is the latent heat flux density ($MJm^{-2}d^{-1}$), E is the depth rate evaporation (mmd^{-1}), H_{net} is the net radiation (MJ m^{-2} day^{-1}), Δ is the slope saturation vapour pressure-temperature curve, de/dT(kPa^0C^{-1}). G is the heat flux density to the ground (MJ m^{-2} day^{-1}), P_a is the air density (kgm^{-3}), c_p is the specific heat at a constant pressure ($MJkg^{-1}{}^0C^{-1}$), e_s is the saturation vapour pressure of air at a particular height (kPa), e_a is the water vapour pressure of air at a given height (kPa), γ is the psychometric constant (kPa^0C^{-1}), r_s is the plant canopy resistance (sm^{-1}), and r_a is the diffusion resistance of the air layer (aerodynamic resistance) (sm^{-1}).

The Variable Storage Routing method equation is expressed as;

$$Q_{in} - Q_{out} = \Delta S \tag{2.12}$$

where, Q_{in} is the catchment inflow (ms^{-1}), Q_{out} is catchment outflow (ms^{-1}), and ΔS is the change in storage (ms^{-1}).

Manning's equation for uniform flow in a channel is used to calculate the rate and velocity of flow in a channel segment for a given time step as explained in equation 2.8. Percolation is calculated for each soil layer in the profile. The equation that is used for calculation of the amount of water that percolates to the next layer is:

$$W_{perc,ly} = SW_{ly,excess}\left(1 - \exp\left[\frac{-\Delta t}{TT_{perc}}\right]\right) \tag{2.13}$$

where, $W_{perc,ly}$ is the amount of water percolating to the underlying soil layer on a given day (mmH_2O), $SW_{ly,excess}$ is the drainable volume of water in the soil layer on a given day (mmH_2O), Δt is the length of the time step (hrs), and TT_{perc} is the travel time for percolation (hrs).

The recharge to aquifers is calculated as;

$$W_{rchrg,i} = \left(1 - \exp\left[\frac{-1}{\delta_{gw}}\right]\right) W_{seep} + \exp\left[\frac{-1}{\delta_{gw}}\right] W_{rchrg,i-1} \quad (2.14)$$

where, W_{rchrg} is the amount of recharge entering the aquifers on day i (mm) is the delay time or drainage time of the overlying geological formation, W_{seep} is the total amount of water existing at the bottom of the soil profile (mm), and $W_{rchrgi-1}$ is the amount of recharge entering the aquifers (mm).

The lateral flow occurs when the storage in the soil layer exceeds field capacity after percolation. The model uses finite difference mass continuity equation, which is expressed as;

$$\frac{s - s_1}{t - t_1} = iL\frac{(q - q_1)}{2} \quad (2.15)$$

where, s is drainage volume of water stored in the saturated zone (m^3), q is lateral flow ($m^3.h^{-1}$), i is the rate of water input to the saturated zone ($m^2.h^{-1}$), and iL is the hill slope length (m).

The contribution of groundwater flow to the stream flow is estimated using the storage routing equation, which is given by Equation 2.16. However, water that recharges the deep aquifer is assumed lost from the system.

$$Q_{gw,i} = Q_{gw,i-1} * \exp^{-\alpha\Delta t} + W_{rchrg} * (1 - \exp^{-\alpha\Delta t}) \quad (2.16)$$

where, $Q_{gw,i}$ is the flow of groundwater into the main channel on day i (mm), $Q_{gw,i-1}$ is the flow of groundwater into the main channel on day i-1 (mm), and W_{rchrg} is the amount of the recharge entering the aquifer on the day i (mm). Water that recharges the deep aquifer is assumed lost from the system.

2.6.4 SWAT Sensitivity Analysis, Calibration, and Validation

SWAT operates on the sequence of sensitivity analysis, calibration, validation, and simulation (Pinto et al., 2013). Hydrologic model successful application depends on the aforementioned processes which are employed efficiently with observed data (Kouchi et al., 2017). To carry out successful calibration and uncertainty analysis of SWAT model, some techniques besides manual method have been developed. They include SWAT-CUP (including PSO, PARASOL, MCMC, GLUE, and SUFI- 2), uncertainty estimation centred on clustering and local error (UNEEC), multi-start (M-Simplex), general algorithm (GA), parameter solution (PARASOL), and Adaptive Clustering Covering (ACCO). Out of all these techniques for uncertainty analysis

and calibration, Abbaspour et al., (2007) hold that the Sequential Uncertainty Fitting 2 (SUFI-2) approach within SWAT-CUP has been most preferred and widely applied. In addition, Schuol et al. (2008) report that SUFI-2 algorithm has higher performance in terms of localizing an optimum parameter range as well as number of simulations.

Sensitivity analysis is the procedure of establishing model output rate of variation in relation to input parameters (Ma et al., 2000). It is the first step that enhances the identification and ranking of parameters having a substantial influence on specific model output. The approaches employed to undertake sensitivity analysis in SUFI-2 involves local and global analysis (Abbaspour et al., 2007; Cibin et al., 2010). Local analysis identifies the output responses by sequentially changing every parameter of the model by a particular percentage while all other parameters are held constant. However, global sensitivity analysis explores the entire interactions and effects on the output variable are established.

The challenge of SWAT calibration as a catchment model is the uncertainty in the prediction. Generally, model uncertainties can be classified into parameter uncertainty, conceptual model uncertainty, and input uncertainty (Abbaspour et al., 2007). Sequential Uncertainty Fitting 2 is a semi-automated method that makes the uncertainty analysis and calibration procedure less complex to accomplish within the practicable time limits (Narsimlu et al., 2015). The concept of the SUFI-2 uncertainty analysis routine is based on stochastic calibration processes. Where there is recognition of uncertainties and errors in SWAT modelling and the SUFI-2 applied to try to capture some degree of processes not fully understood in the natural system. It implies that uncertainty and calibration are intimately related (Abbaspour et al., 2015).

Uncertainty in parameters, given as ranges, accounts for all sources of uncertainties in SUFI-2 (Abbaspour et al., 2004). Uncertainties in the model output variables due to the propagation of the uncertainties in the parameters are expressed as 95 percent probability distributions. Using Latin hypercube sampling, the 95 percent probability distributions are computed at the 2.5 percent and 97.5 percent degrees of the cumulative distribution of an output variable and hence described as 95PPU (95 percent prediction uncertainty). SUFI-2 stochastic process provides model results (95%PU) that envelopes most of the observed data in the real system. As explained by Abbaspour et al. (2007), two statistics (R-factor and P-factor) have been developed to quantify the fit between simulation results, expressed as 95PPU and observation expressed as a single signal. R-factor is the thickness of the 95 percent prediction uncertainty while P-factor is the percentage of the observed dataset bracketed by modelling output, the

95%PU. As per Abbaspour et al. (2015) recommendations for stream flow, the uncertainty analysis and calibration (SUFI-2) modelling performance is acceptable at (P-factor > 0.7) and (R-factor of around 1).

According to Abbaspour et al. (2007) and Arnold et al. (2011), calibration is the process of minimizing the model output uncertainties before running simulations by adjusting parameters to best capture the local conditions. Validation is the running of the model with calibrated parameters in an independent data mass so that the applicability of the model can be assessed through statistical tests. The two processes are undertaken typically by dividing the available measured data into two datasets (one for calibration and another for validation). SUFI-2 algorithm executes up to several thousand iterations to obtain optimum parameters. The model parameters are adjusted within acceptable ranges until the goodness of fit to observation is achieved (Abbaspour et al., 2007; Neitsch et al., 2011). The final stage then becomes applying the model-calibrated parameters to the remaining portion of the observed data (Moriasi et al., 2007).

2.6.5 SWAT Model Performance Assessment

Several statistics have been developed and proposed to assess SWAT hydrologic predictions. The widely applied statistical techniques entail Nash Sutcliffe model efficiency (NSE), Percentage Bias (PBIAS), and Coefficient of Determination (R^2) (Abbaspour et al., 2015; Moriasi et al., 2007). The R- squared statistical performance matric measures how the observed versus simulated regression line approaches an ideal match (Van Liew et al., 2003). R^2 values range from 0 to 1, with a value closer to 0 or 0 indicates no correlation. And a value closer to 1 or 1 indicates relative perfect linear covariation between the two datasets. It implies that a correlation measurement suggests a higher accuracy of the model when the value is approaching one.

The Nash Sutcliffe model efficiency ranges from $-\infty$ to 1 and measures how well the observed and simulated data match the 1:1 line (Moriasi et al., 2007). A value of NSE closer to zero or equal to 0 indicates that the mean of the observed data is a better predictor than the model, and the values closer to one or 1 imply a perfect fit between the observed and simulated. Percentage Bias is a measure of the average tendency of the simulated values to be larger or smaller than the corresponding observed values and can indicate the level of model performance. The optimal value of PBIAS is zero, and the values closer to zero is an indicator of better model prediction performance. Negative values indicate the underestimation bias whereas positive

values indicate model overestimation bias. Considering various time steps of modelling, the performance evaluation of the hydrologic model under the defined values of NSE, R^2, and PBIAS can be rated as shown in Table 2.2 (Moriasi et al., 2007; Van Liew et al., 2003).

Table 2.2: Proposed classification of Statistical indices

NSE	PBIAS	R^2	Rating
75.0% NSE≤ 100%	PBIAS≤ ±10.0%	75.0%<R^2≤100%	Very good
60.0 %<NSE≤ 75.0%	±10.0%<PBIAS≤ ±15.0%	60.0%<R^2≤75.0%	Good
36.0%<NSE≤ 60.0%	±15.0%<PBIAS≤±25.0%	50.0%<R^2≤60.0%	Satisfactory
0.0%<NSE≤ 36.0%	±25.0%<PBIAS≤±50.0%	25.0%<R^2≤50.0%	Poor
NSE≤ 0.0%	±50.0%≤PBIAS	R^2≤25.0%	Inappropriate

Note. Adopted from a research by Moriasi et al. (2007).

2.7 Forecasting of Climate Variability Impact on Stream flow

Climate variability can severely perturb catchment hydrology and thereby affect different hydrologic variables such as stream flow and water resources in general (Teutschbein, 2013). To simulate climate variability impact in unknown future situations, hydrologic models need reliable climate variables for current and future climatic conditions. According to IPCC, future climatic scenarios can be estimated from projected or predicted reliable quantitative information on climate variables (e.g., precipitation and temperature) on their spatio-temporal distribution. IPCC (2014) defines projection as the simulated response of the climate quantities to a future scenario of the concentration of greenhouse gases, aerosols, and emissions usually derived using climate models (GCMs and RCMs). Unlike projection, prediction is based on knowledge of current and past states of the climate variables.

2.7.1 Climate Models

Several researchers have demonstrated the wider application of climate models (GCMs and RCMs) for estimation of future climate variables in many regions globally including East Africa. For instance, Githui et al. (2009) assessed future climatic impacts on western Kenya (Nzoia catchment in the Lake Victoria basin) and how they might influence stream flow. Future climate variables (temperature and precipitation) were obtained from GCMs. Results showed a progressive increase in precipitation in the 2020s and 2050s. They also reported a positive trend in temperature with highest increase in years beyond 2050s. Similar results were obtained by Rwigi (2014), a study carried out in Sondu River basin (South West Mau Forest Block).

Projections were obtained from the third generation Hadley Centre Regional Climate model (HadRM3) using PRECIS (RCM).

Ongoma et al. (2018) simulated variations in air temperature and precipitation over East Africa region using CMIP5 models. They reported a likelihood of increase in temperature and an increase in extreme precipitation events in future. However, they recommended that the results should be used with caution since they were based on course resolution models susceptible to bias. Also, Shongwe et al. (2011) based on CMIP3 models simulated increases in both intensity and mean annual rates of high rainfall beginning in the early 21st century and progressive increase in temperature in East Africa region. In a study of temperature and precipitation changes projection applying PRECIS over the horn of Africa, Omondi et al. (2014) observed the likelihood of reduced days of cold nights and increased number of warm nights and days in future. Many studies globally and even in Kenya have always use GCMs and RCMs projected climate variables to drive hydrologic models such as SWAT to estimate future impacts of climate variability on water resources (Omwoyo et al., 2017; Prusty, 2018; Rwigi et al., 2016).

Although GCMs and RCMs provide relevant datasets for future climate variability impact assessment as by Rwigi (2014) assertions, an accurate approximation, however, requires their ability to simulate climate variables at a convenient scale. As illustrated by Elgaali (2005), most climate models may not be precise because of their temporal as well as spatial resolutions. In fact, Sabiiti (2008) and Omondi (2010) noted that though PRECIS RCM performed so well in the East Africa region, the results might not be applied for hydrological modelling on a river basin scale since even within a basin, there exists a spatial variation in rainfall distribution. Jiang et al.'s (2013) results also showed the inadequacy of GCMs and RCMs for studies on extreme hydrological events that are strongly associated with multi-scale temporal precipitation variability. GCMs and RCMs predictions have uncertainties majorly from physical process parameters, scale degradation techniques, and emission scene erroneous errors (Dobler et al., 2012). After all, GCMs and RCMs are dependent primarily on scenarios of future natural and anthropogenic forcing that are uncertain (Teutschbein, 2013).

Owing to the uncertainties of the climate models, the alternative can be the integration of hydrological models for the creation of a hybrid model that is capable of estimating future stream flow. Besides, a study by Khashei et al. (2010) in their both analytical, theoretical, and empirical models coupling findings indicated that integrating models effectively improves their

predictive performance. For instance, Noor and Kalin (2016) coupled artificial neural network and SWAT models for enhanced daily stream flow forecast in unmonitored catchments of Atlanta, USA. In their findings, SWAT_ANN hybrid model created led to improved prediction of daily stream flow. Senent et al. (2019) used the same approach and recommended that the enhanced accuracy could also be realized in a wider application of hydrologic response predictions.

Climate variables predictions are highly non-linear and complicated phenomena. Their forecasting requires advanced computer modelling techniques for precise prediction. The alternative technique that has been widely applied to model the behavior of such nonlinear systems is Artificial Neural Network (Lee & Tuan, 2016; Ozoegwu, 2019; Somvanshi et al., 2006). ANN modelling approach has been ranked so higher because they are universal approximators, capable of adaptive learning, fault-tolerance, and real-time operation. Their power comes from statistical parallel processing of historical data, and ANN modelling approach needs no prior assumption (Ozoegwu, 2019).

For instance, Somvanshi et al. (2006) compared ANN and autoregressive integrated moving average (ARIMA) nonlinear statistical methods for modelling and predicting the behavioural pattern in precipitation based on past observed data. In their findings, it was revealed that ANN model outperformed ARIMA model and they proposed the use of ANN for efficient and accurate forecasting of climate variables. In addition, Ise and Oba (2019) explored the performance of a phenomenological top-down model created by artificial neural networks for prediction of monthly air temperatures. They observed that ANN successfully predicted the temporal variation of air temperature for a decade with an accuracy of 97 % after training with 30 years of historical data. The study demonstrated that the performance of ANN was notably high in comparison to methods such as earth system tools and physics-based GCMs models.

2.7.2 Artificial Neural Network

Artificial neural network is a resemblance of the biological nervous system that entails a data-driven process with a flexible mathematical set of rules proficient in solving complex nonlinear relationships between input and output data (Da Silva et al., 2017; Van & Bohte, 2017). ANNs are based on the human brain principle of communication by sending signals to each other through complex connections. Thus, ANN using complex algorithms (Hayati & Shirvany, 2007) mimics the training or learning processes of the human brain. In a neural network, neurons are the basic processing unit and can are viewed as processors that compute the sum

of weighted inputs and then apply a non-linear transfer function to the computed sums. All connections have weights attached that have either negative or positive values associated with them. Negative weights inhibit neurons while positive weights activate them. This implies that synaptic weight is the component that determines how a network behaves. Weights store the network's knowledge within interneuron connects and they determine the behaviour and performance of ANN (Vishwakarma, 2012).

Figure 2.4 shows typical artificial neurons with inputs (X_1, X_2, …, X_n) connected to neuron j with weights (W_{1j}, W_{2j}, …, W_{nj}) on each connection. With each signal being multiplied by its associated weights on the connection, the neurons sum all the signals it receives.

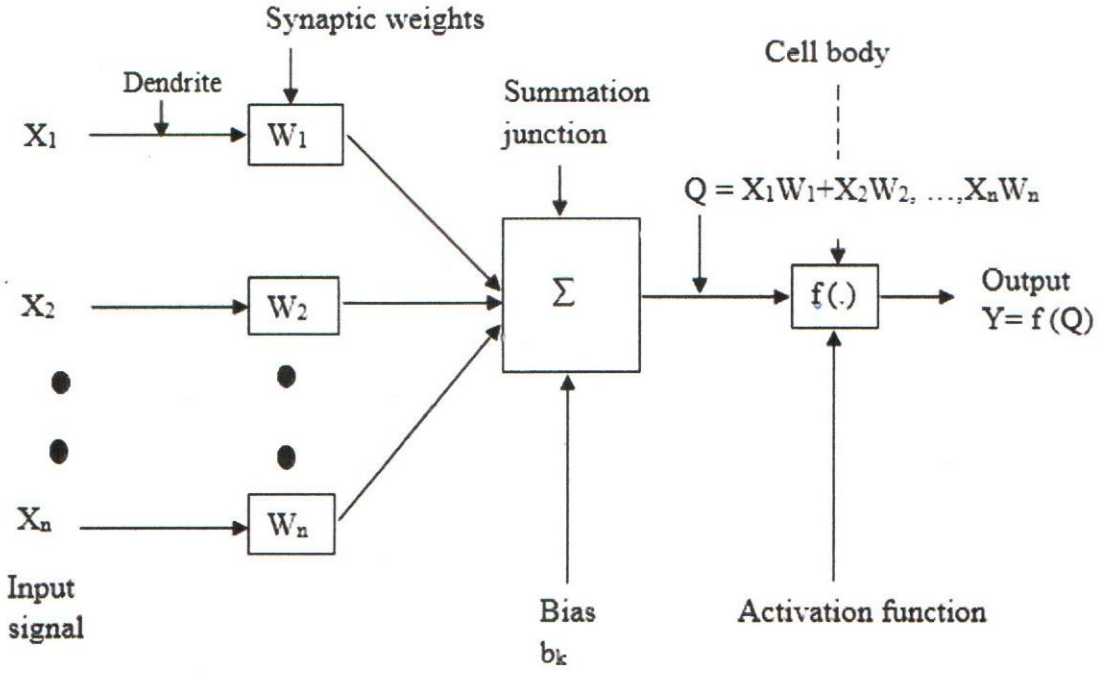

Figure 2.4: A typical artificial neurons
(Modified from a study by Da Silva et al., 2017)

The output (Q) is then processed through an activation function f (.), which is usually non-linear to give the final output (Y). As explained by Da Silva et al. (2017), input and output signal relationship within the neural networks can be expressed as expressed in the following function:

$$Y = f(Q) = f\left(\sum_{i}^{n} W_i X_i + b_k\right) \tag{2.17}$$

where, X_i is the input signal i, W_i is the weight attached to the input signal i, n is the number of input signals, b_k is the bias at cell of the body, f is the activation function, and Y is the output.

Figure 2.5 shows the most common transfer (activation) functions of artificial neural networks as illustrated by Da Silva et al. (2017).

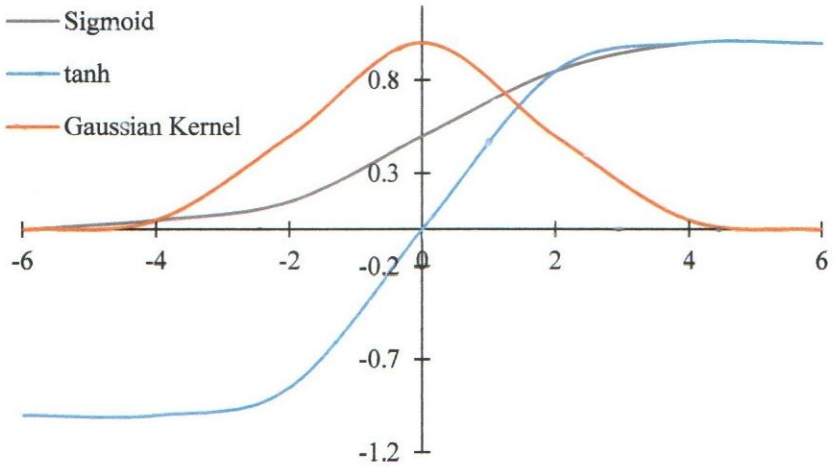

Figure 2.5: Types of ANN activation functions

The Gaussian Kernel function can be expressed as;

$$f(x)=\frac{1}{\sqrt{2\pi\sigma}}e^{\frac{-(x-\mu)^2}{2\sigma^2}} \tag{2.18}$$

where, x is an input vector.

The Hyperbolic tangent activation function can be expressed as;

$$f(x)=\left[\frac{2}{1+e^{-2(x)}}\right]-1 \tag{2.19}$$

The logistic sigmoid activation function can be expressed as;

$$f(x)=\left[\frac{1}{1+e^{-(x)}}\right] \tag{2.20}$$

The most used transfer function (Özbay & Tezel, 2010) is the sigmoid (logistic) function because of its easily differentiable properties, which is appropriate with the application of back-propagation algorithm. Logistic sigmoid function is one of the best ways to fit models for categorical data, specifically for binary response data modelling. The logistic regression model predicts P(Y=1) as a function of X. Unlike linear regression, logistic regression can directly approximate probabilities (values that are restricted to the (0, 1) interval. Nevertheless, an activation function selection may be dependent on the type of training algorithm and scaling approach applied. Some of the learning algorithms are presented in Table 2.3.

Table 2.3: Training Algorithms of ANN

Training Function	Algorithms
Trainlm	Levenberg-Marquardt
Trainbr	Bayesian Regularization
Trainbfg	BFGS Quasi-Newton
Traingdm	Gradient Descent with Momentum
Traingd	Gradient Descent
Trainoss	One Step Secant

Note. Adopted from Ruiz et al. (2016).

As discussed by Alabi (2017), feedforward and recurrent neural networks are the main categories of ANNS. Due to the feedback connections, recurrent networks are characterised by loops and encompass time series applications for prediction of future scenarios. Some of the common types of recurrent neural networks include Nonlinear Input-Out, Nonlinear Autoregressive (NAR), and Nonlinear Autoregressive with External (Exogenous) Input (NARX). The modelling power of recurrent neural networks especially the NAR makes it suitable than any other statistical tool for predictions of climate variables since weather patterns vary randomly in a real environment. NAR has been applied widely for forecasting hydro-climatic variables based on historical data series (Benmouiza & Cheknane, 2016; Wang et al., 2020) (Figure 2.6).

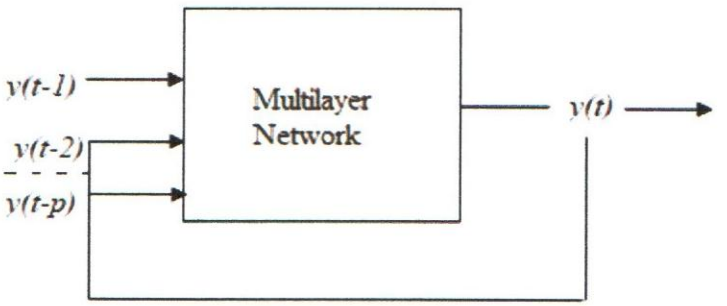

Figure 2.6: The NAR neural network
(Adopted from Ruiz et al., 2016)

It is a type of recurrent dynamic network defined by linear autoregressive model with feedback connections. NAR uses past values of the actual time series to predict next values as can be expressed in Equation (2.21) (Ruiz et al., 2016).

$$\hat{y}(t) = f\left(y(t-1) + y(t-2) +, ..., + y(t-p)\right) \tag{2.21}$$

where, f is a nonlinear function, where the future values depend only on regressed p previous values of the output signal. Levenberg-Marquardt backpropagation procedure (Alwakeel & Shaaban, 2010) is the most common training rule for NAR. Benmouiza and Cheknane (2013) assert that backpropagation technique consists of minimizing the global quadratic error between the network output and the desired target by adjusting the weight values.

Unlike the recurrent networks, the feedforward neural networks are characterized by neither cycles nor loops in the network, hence, neurons are organized into layers having unidirectional connections (Che et al., 2011). FNN major applications include data clustering, classifications, input-output curve fitting, and pattern recognition (Jun et al., 2017). Many researchers have used Feedforward neural networks widely in solving real and complex hydrologic (forecasting, modelling, and predictions) problems with great accuracy (Jun et al., 2017; Kişi, 2007; Kuok et al., 2010). The type of FNN that is relatively simpler to implement and has numerous applications where nonlinear mapping is to be done between inputs and outputs is the Feedforward backpropagation (Che et al., 2011; Li et al., 2017).

On a connection between nodes, the feedforward backpropagation takes the input variables and multiplies them by the weights. Before passing it through a threshold function to generate an output, their products are summed. The operation of backpropagation algorithm involves the processes of propagating the error back into the network, which minimises the error between the target and output. The weights on each of the connections between the neurons are changed with regard to the size of the initial error. Then, new output and error generated by the input data being few forward again. Several iterations continue until a satisfactorily reduced error is attained. The training is halted immediately after the error reaches an acceptable value since the neurons use a transfer function controlled by an objective function. Finally, the resulting model is a function that is an internal representation of the output.

A single-layer feedforward backpropagation of S logsig neurons having R inputs is as shown in Figure 2.7 in full detail on the left and with a layer diagram on the right.

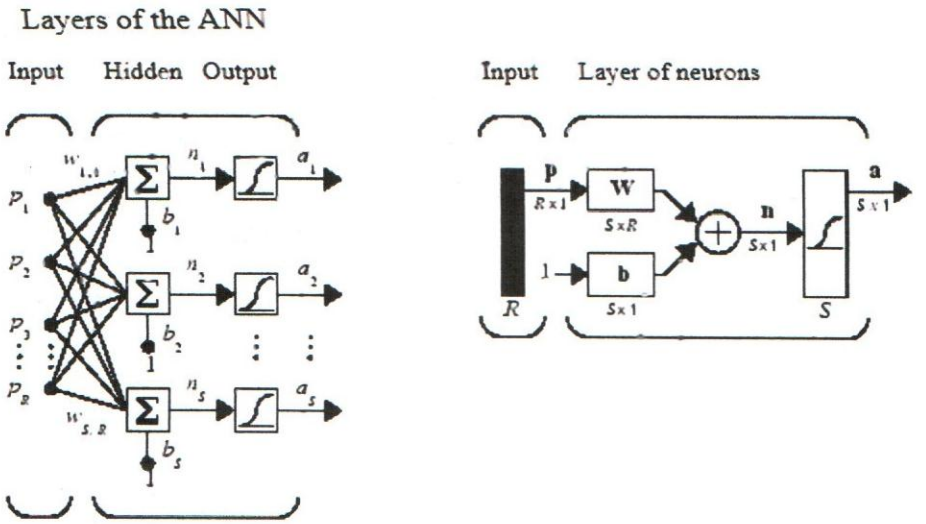

Figure 2.7: Architecture of a single layer feedforward neural network (Modified from Da Silva et al., 2017)

R is the number of components in the input vector, S is the number of neurons in the hidden layer, and connections between neurons are represented with weight factors w. b is bias, Σ indicates synapses – summation of signals from previous neurons, and a = logsig (Wp + b). FNN networks in most scenarios have one or more hidden layers of sigmoid neurons or any other transfer function followed by an output layer of linear neurons. Multiple layers of neurons with nonlinear transfer functions is key because it allows the network to learn nonlinear relationships between input and output vectors (Li et al., 2017).

CHAPTER THREE

MATERIALS AND METHODS

3.1 The Study Area

Njoro River catchment as shown in Figure 3.1 is located between longitudes 35°50'13" E - 36°3'28"E and latitudes 0.13 °13'58''S - 0°34'58''S. It is located within the Mau Forest Complex in the western rim of the East Africa Rift Valley.

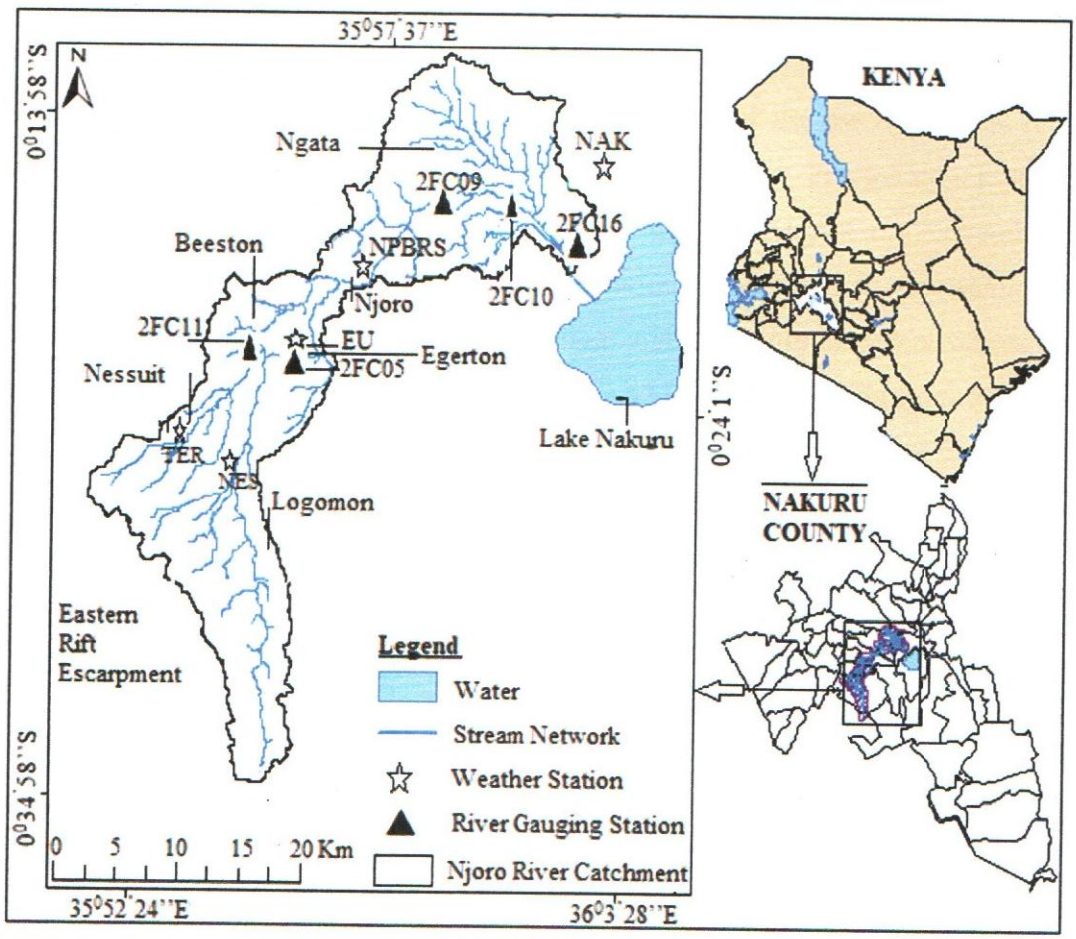

Figure 3.1: Njoro River Catchment

River Njoro run down from an altitude of about 3080 m above mean sea level (amsl) at its source in the Eastern Mau Hills to about 1755 m as it drains into L. Nakuru. The river from its source is about 60 km long to the river gauging station at the shore of L. Nakuru (2FC16), and it's enclosed in an area of about 263 km^2 which contributes channel flows. The confluence at Egerton University divides the river into almost two equal parts. Upper part of the river holds water nearly throughout the year and could be described as perennial. However, the lower part of the river has water mostly during the rainy season and could be described as ephemeral. Along the entire river, numerous rivulets are merging from the sides that have water only during

or immediately after rainstorms. Njoro River catchment originally had five river gauging stations: 2FC05 (upper Njoro River catchment outlet); 2FC09 (at Kirobon); 2FC10 (at Ronda); 2FC11 (at Little Shuru Tributary); and 2FC16 (Lake Nakuru) and 2FC19 (at Egerton University gate-bridge). Out of all the river gauging stations, it's only 2FC05 that is operational and has reasonably longer and continuous data even though a lot of data is missing.

The three registered weather stations in Njoro River catchment with World Meteorological Organization are; Njoro Plant Breeding Research Station (ID: 09035021), Nakuru Meteorological station (ID: 09036261), and Egerton University weather station (ID: 09035092). EU weather station situated at the central part of the catchment has relatively consistent meteorological data ranging from 1944 to present years. Precipitation pattern is tri-modal in Njoro River catchment with peaks currently in May, August and November. From EU weather station data, the average annual precipitation in the Njoro River catchment range between (1000 - 1029 mm), mean annual maximum and minimum air temperatures, relative humidity, wind speed are about 23.5 ^{0}C, 13.38 ^{0}C, 64.62 %, and 5.2 km/hr respectively. Other recorded average daily values of climate variables at EU weather stations are 5.4 hr.day^{-1} and 3.3 mm.day^{-1} for a mean duration of sunshine and evaporation respectively.

3.1.1 Climatic, Hydrologic, and Field Data Acquisition

The following data were obtained from Water Resources Authority located at Nakuru town and the fieldwork:

i) Historical daily climate variables: wind speed, surface air temperature, and relative humidity from EU weather station, Nakuru Meteorological and NPBRS for the period (1978-2017).
ii) Solar radiation from Egerton University weather station for the period (1978 - 2022).
iii) Mean monthly precipitation and surface air temperature were forecasted between the period 2018 and 2037.
iv) Historical daily stream flow and water level data of RGS 2FC05 from Water Resources Authority (Nakuru Office) for the period (1941 – 1999), which was required for SWAT calibration and validation.
v) Coordinates of streams, reach, and the location of river gauging stations using Global Positioning System (GPS) at different points.
vi) Coordinates of different land cover for derivation of various spectral signatures and geometric correction procedures for supervised LULC classification processes.

3.1.2 Spatial Data Acquisition

The satellite data and other geospatial data products that were downloaded and used for hydrologic modelling are presented in Table 3.1.

Table 3.1: Satellite remote sensing and Geospatial data products

Data	Source / Attribute values
Landsat imagery (1978/12/31) Scene size (185 x 185 Km)	Earth Explorer website (https://earthexplorer.usgs.gov/). Satellite (L1-5), Sensor (MSS), Grid cell size reflective (60m), Map projection level – 1 (UTM), Datum (WGS 84), WRS Path/WRS row (181/60). For raster MTL.text 4Bands (Green, Red, Near Infrared 1, Infrared 2)
Digital Elevation Model	Earth Explorer website (https://earthexplorer.usgs.gov/). The 30 m spatial resolution (SRTM - DEM)
Soil	Food and Agriculture Organisation (FAO) data

3.2 Trend Analysis of Climate Variables

The first activity carried out after the data quality checks was the computation of annual anomalies of all the climate variables using Equation 3.1 as described in the guide to climatological practices (WMO, 2011).

$$\text{Anomaly} = X - \text{Xbar} \tag{3.1}$$

where, X is actual annual value of a climate variable, and Xbar is the long-term average value of the variable (40 years).

The monthly and annual trend analysis of climate variables from 1978 - 2017 was then carried out by the use of a non-parametric Mann-Kendall trend test. MK trend analysis was the most preferred approach because it requires fewer conditions of validity and accommodates missing values as well as outliers (Ongoma & Chen, 2017; Partal & Kahya, 2006).

Climate variable (air temperature, precipitation, wind speed, relative humidity, solar radiation data) was arranged sequentially in order of (the month/year) measurement. The value for each month or year x_i (i= 1, 2, 3... n) was compared with the value of the preceding months or years x_j (j = 1, 2, 3..., j-1), ($j > i$). The sign (s) used to count the difference between the

values from the time series was obtained as Mann-Kendall statistic (S) according to the illustrations by Mann (1945) and Kendall (1975), (Equation 3.2).

$$S = \sum_{i=1}^{n-1} \sum_{j=i+1}^{n} \operatorname{sgn}\left(x_j - x_i\right) \tag{3.2}$$

where, x_i and x_j were monthly or annual values in years i j and, $(j > i)$.

The $\operatorname{sgn}\left(x_j - x_k\right)$ was a sign function expressed as;

$$\operatorname{sgn}\left(x_j - x_i\right) = \begin{cases} +1, \ if\left(x_j - x_i\right) > 0 \\ 0, \ if\left(x_j - x_i\right) = 0 \\ -1, \ if\left(x_j - x_i\right) < 0 \end{cases} \tag{3.3}$$

A positive value of S is an indicator of an increasing trend, and a negative value indicates a decreasing trend (Mann, 1945; Kendall, 1975). Under the null hypothesis of no trend and independence of the series terms, the variance of the Mann-Kendall statistic was calculated as in Equation 3.4.

$$Var(S) = \frac{n(n-1)(2n+5) - \sum_{k=1}^{m} t_k (t_k - 1)(2t_k + 5)}{18} \tag{3.4}$$

In Equation 3.4, n is the number of data points, m is the number of tied groups, and t_k denotes the number of ties of extent k. A tied group is a set of sample data having the same value. The modified Mann-Kendall trend test was also used for the estimation of variance, thus significant values of pk were considered for calculating the variance correction factor n/n^*_s as the variance of S would be underestimated for the positively auto-correlated data:

$$\frac{n}{n_s^*} = 1 + \frac{2}{n(n-1)(n-2)} \times \sum_{j=1}^{n-1} (n-k)(n-k-1)(n-k-2)\, p_k \tag{3.5}$$

where, n represents the actual number of observations, n_s^* is represented as the effective number of observations to account for the autocorrelation in the data and p_k is considered as the autocorrelation function for the ranks of the observations. The correlated variance was then calculated based on the procedure proposed by Rao et al. (2003).

$$V^*(S) = Var(S) \times \frac{n}{n_s^*} \tag{3.6}$$

Then the standard normal test statistics Z_c were computed using the following expression;

$$Z_c = \begin{cases} \frac{S-1}{\sqrt{V^*(S)}} if, S > 0 \\ 0, S = 0 \\ \frac{S+1}{\sqrt{V^*(S)}} if, S < 0 \end{cases} \quad (3.7)$$

where, Z_c followed a standard normal distribution. A positive (negative) value of Z_c signified an increasing (decreasing) trend. To quantify statistically the significance of the increasing or decreasing trends in climate variables two-tailed test was applied at the 5 % significance level. At $p < 0.05$ significance level, the null hypothesis of a trend (increasing or decreasing) not significant was rejected if $-1.96 < |Z_c| > 1.96$.

3.3 Modelling Stream flow Response to Climate Variability using SWAT

The study examined how stream flow varies both spatially and temporally under different climatic scenarios in Njoro River catchment. To achieve this, the response of hydrologic variables to climate variability was modelled by the use of SWAT. SWAT was selected because it is a semi-distributed based model, computationally efficient, and requires fewer input data (Arnold et al., 2012; Neitsch et al., 2011). SWAT input datasets were prepared, and SWAT was set up and executed, calibrated, and validated, and then applied to simulate hydrologic variables including stream flow spatially and temporally.

3.3.1 Preparation of Digital Elevation Model

Using the ArcMap version 10.4, the 30 m spatial resolution SRTM-DEM from the USGS was clipped and projected to WGS 84 / UTM (Universal Transverse Mercator) zone 36S. The projected DEM was used to parameterize the topographic attributes of the catchment in terms of the sub-catchment area, stream length, stream width, stream depth, stream flow direction, mean slope, stream network, and outlets. The prepared DEM as an input of SWAT is shown in Figure 3.2.

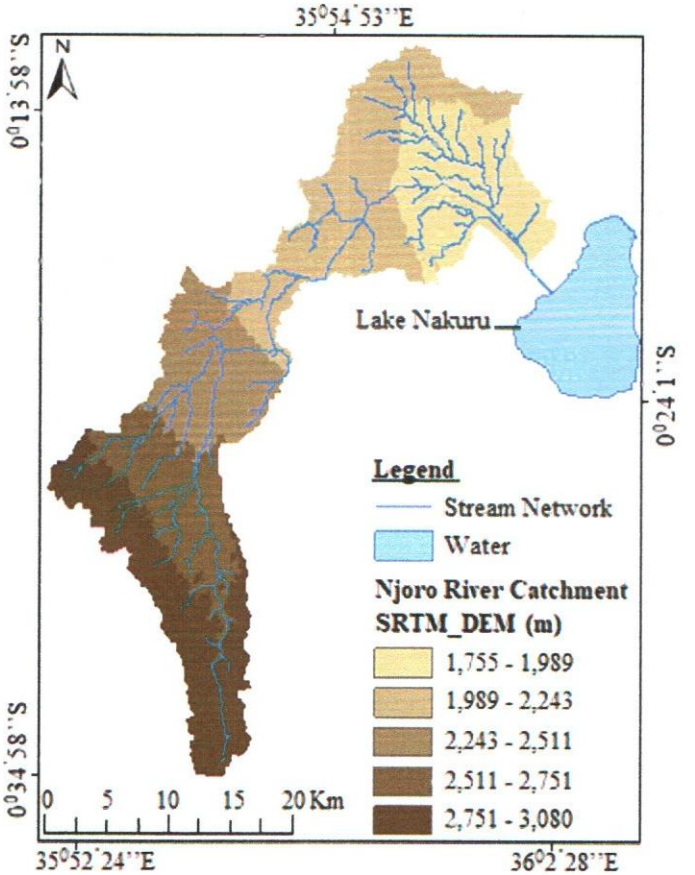

Figure 3.2: Shuttle Radar Topography Mission-DEM for Njoro River catchment

3.3.2 Preparation of Land Use-Land Cover Map

LULC is a key SWAT spatial data that was used for the derivation of hydrologic response unit parameters as expounded by Arnold et al. (2012). The imagery of LULC for classification was from Landsat 1 MSS sensor aboard having four channels, two infrared, and two visible. Downloaded satellite imagery was pre-processed (clipped and resampled). Then, it was projected to WGS 84/UTM zone 36S. Subsequent procedures undertaken using ArcMap version 10.4 to achieve supervised classification for the LULC as shown in Figure 3.3 then followed. Layer stacking, sub-setting, geometric correction (ground-truthing activities) (Table 2A, APPENDIX A), image enhancement, and Maximum likelihood classification. LULC categories classified were forest, shrubs, grassland, agriculture, buildings, and bare land. Although, the land cover map had a slight influence by a permanent defect of lines that imitated bare land class during classification at the lower part of the catchment, the effect was insignificant because hydrologic modelling only covered the upper part of the catchment.

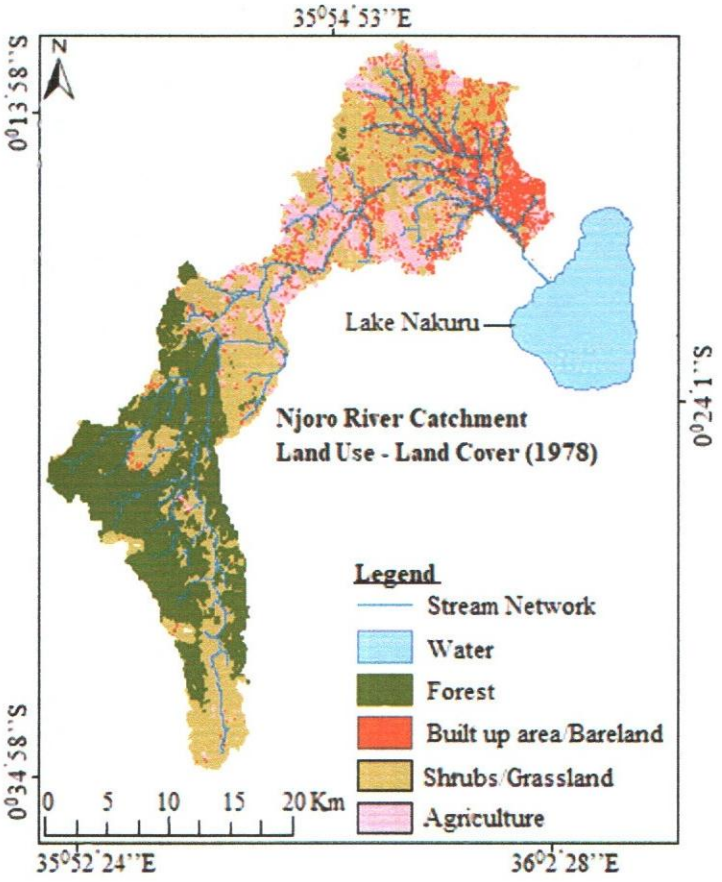

Figure 3.3: Classified Landsat MSS image of 1978 for Njoro River catchment

3.3.3 Preparation of Soil Data

Soil data is very important because its nature and condition influence how a certain precipitation event is partitioned (Mukundan et al., 2010). In this study, soil data downloaded from FAO was clipped to cover Njoro River catchment. It was then projected to WGS 84/UTM zone 36S and rasterized in ArcMap, which was the required format by the SWAT model (Figure 3.4). With regards to FAO/UNESCO soil map of the world categorisations, Njoro River catchment mainly comprises of four soil types. These are Phaozems (Gh7-29), Mollic Andosols (Tm10-2bc), Ferric Luvisols (Lf17-2ab), and Nitosols (Ne29-2bc). Soil data for SWAT as shown in Figure 3.4 was used to derive soil properties such as moisture content, infiltration capacity, bulk density, texture, chemical composition, porosity, organic carbon content water repellence, and hydraulic conductivity for each hydrologic response unit. Finally, the soil map prepared was incorporated into SWAT database user-soil by the creation of soil data lookup tables.

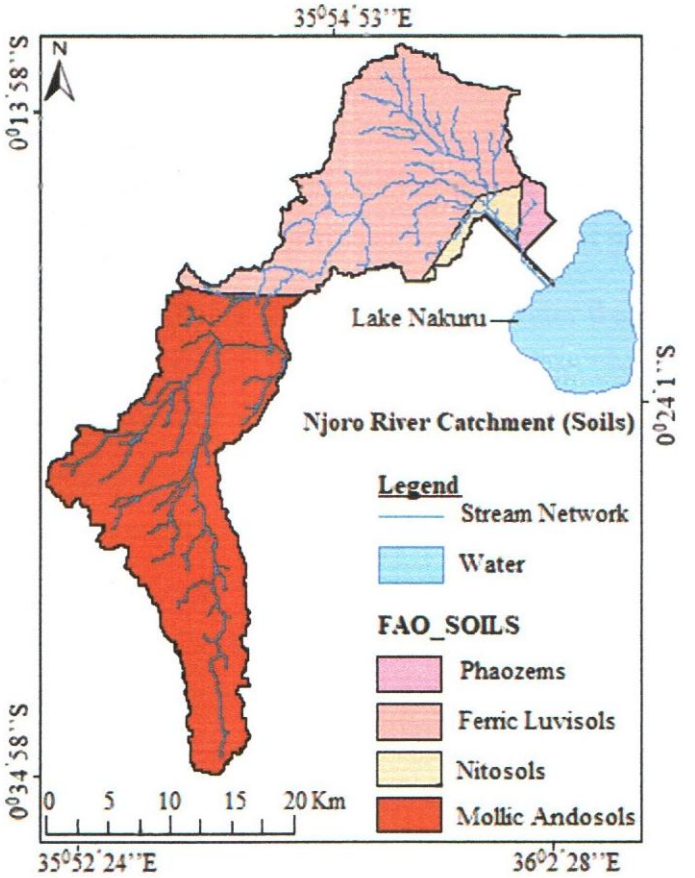

Figure 3.4: FAO soil classification at Njoro River catchment

As explained by Mainuri and Owino (2013), Njoro River catchment is under volcanic rocks varying from the tertiary quaternary to previous pyroclastic rocks. The rocks are mainly black ashes, basaltic tuffs, sanidine minerals, pumice, ciders, photo-nolites, sediments, welded tuffs, and agglomerates on the valleys, plains, plateau, and uplands, and alluvium and lacustrine sediments. Four types of the soil in the catchment as classified in Figure 3.4 have been formed on the pyroclastic rocks, and their rate of infiltration varies from poorly drained to well-drained to extremely drained, with the structures in the range of moderately strong to strong, and texture ranging from loam, clay, and loam clay (Mwetu, 2010).

3.3.4 Preparation of Climate data and Weather Generator

SWAT requires daily minimum and maximum air temperatures, relative humidity, wind speed, precipitation, and solar radiation (Arnold et al., 1998). All these climate variables' values can be read from the observed data or they may be simulated by a weather generator. The WGEN input file comprises of the statistical data required to approximate missing data and simulate representative daily climate data for the sub-catchments. In this study, observed climate data (1978-2017) from EU weather station were imported into SWAT database and then used to

define weather generator parameters in the input files. As per the requirements of WGEN_user in the SWAT database, the procedure and equations provided by Arnold et al. (2012) were used to build a weather generator for Njoro River catchment. WGEN database was developed by first generating a location table in SWAT2012 database that contained name, identification number, latitude, longitude, elevation of the station, and number of rain years.

Parameters were then computed in the subsequent columns after the column of Rain -Years; TMPMX (mon), TMPMN (mon), TMPSTDMX (mon), and TMPSTDMN (mon) for all months (^{0}C). PCPMM (mon) (mm), PCPSTD (mon), and Skew coefficient for daily precipitation (PCPSKW(mon)) in all months. The probability of a wet day following a dry day in the month (PR_W(1,mon)) and the probability of a wet day following a wet day in a month (PR_W(2,mon)). Average number of days of precipitation in month (PCPD(mon)) and the maximum 0.5 hour rainfall in entire period of record for month (RAINHHMX(mon)) (mm). The average daily solar radiation (SOLARAV(mon)) (MJ/m^2/day) for the months, mean daily dew point temperature (DEWPT(mon)) (^{0}C) for each month or relative humidity (%), and average daily wind speed (WNDAV(mon)) in all months (m/s). WGEN was used to simulate Solar radiation from 2002 to 2017.

3.3.5 Catchment Delineation

Using ArcSWAT 2012 watershed delineator, the SRTM-DEM 30 m by 30 m was applied to extract topographic parameters and the sub-catchment boundaries. Sub-catchments delineation was based on the topography using GIS algorithm. Steps under this process include filling of pits of depression by raising the elevation in the pit, calculation of each cell's flow direction using D8 algorithm, computation of each cell's flow accumulation, and definition of actual streams by a threshold of flow accumulation. Key procedures carried out entailed, loading DEM for computation of sub-catchments and reach parameters; specifying the least possible sub-catchment area for the establishment of the detail of the stream network; Reviewing and editing the stream network outlets for the determination of the optimum number of sub-catchments, and finally calculation of sub-catchment parameters.

The part of reviewing and editing of streams was guided by mosaicked three topographic map sheets of a scale of 1:50, 000 (Njoro sheet-118/4, Nakuru sheet-119/3 and Mau Narok sheet 132/2) and field GPS geo-referencing coordinates (Table 3A, APPENDIX A). Once the discretization was finished, a topographic report was added to the project and many layers were added: upper Njoro River catchment, Sub-catchments, Reach, Outlet (at point 2FC05), and

Monitoring points. The extent of delineation was then finally confined to the upper Njoro River catchment for hydrologic modelling purposes because 2FC05 river gauging station was the only outlet point where there was observed data for SWAT model calibration and validation.

3.3.6 Hydrologic Response Unit Analysis

After the discretization of the catchment, Soil and land-use system thematic maps were imported. LULC and soil layers were loaded into current project and HRU Analysis menu on the ArcSWAT was used to assess slope features and to define land use/soil/slope combination. Then areas with homogeneous soil, LULC, and slope characteristics (hydrological response units) were defined and differentiated within each sub-catchment. HRUs are always applied in SWAT as basic units for hydrological balance simulations (Abbaspour et al., 2009). The key processes undertaken to achieve HRU analysis were; defining and reclassification of LULC layer with the assistance of user lookup tables for editing the default LULC database so that local conditions were reflected, because the study area was outside the USA. Soil spatial data was also reclassified with the help of user soil lookup tables that linked the layer to the SWAT soil database. The slope was reclassified based on DEM attributes. Finally, upper Njoro catchment having only one soil type according to FAO classification, the overlaid layers were used to delineate the hydrologic response units for every sub-catchment using threshold levels of 20 % slope, 5 % land use.

3.3.7 SWAT input Tables and Editing

The command in writing input tables and editing SWAT input on the ArcSWAT were used to accomplish the following; importation and definition of climate variables, creation of the input tables, database update, editing input parameters, and rewriting of SWAT input files. Weather data (daily precipitation, relative humidity, wind speed, solar radiation, and minimum and maximum air temperature) from EU weather station for the period (1978 - 2017) were loaded under WGEN_user and assigned to the sub-catchments. The database files containing the information needed were then created to generate default input for SWAT after the successful loading of climate variables. All tables were selected and SWAT project database was written and updated. Finally, the sub-catchments input parameters were edited and saved, and SWAT input files were then rewritten.

3.3.8 Sensitivity Analysis of SWAT Parameters

After trial runs, SWAT parameters sensitivity analysis was conducted using the SUFI-2 algorithm executed by the SWAT-CUP Program software, which was based on the calibration

and validation period (1978-1990) (Figure 1B, APPENDIX B). Multiple regression systems as expressed in Equation 3.8 was used in computing parameters sensitivity guided by Latin hypercube sampling versus the objective values as described by Abbaspour et al. (2007).

$$G = \alpha + \sum i=1 m \beta i bi \quad (3.8)$$

where g is the objective function value, α is the regression constant, b is the parameter, m is the number of parameters, and β corresponds to the technical coefficient attached to the variable b.

An optimization process that reflected the sensitivity of the 18 SWAT input parameters was carried out in two sets; local and global sensitivity. Sensitivity was determined by the values of t-stat and *p*-value for 1200 iterations conducted for every change of the SWAT input parameters. The t-stat was the regression coefficient of a parameter divided by its standard error, thus, if the standard error was less than the coefficient value, then the value of t-sat would be greater than zero, hence, parameter sensitive (Abbaspour et al., 2015). It implies that the higher the absolute value of t-stat and the smaller the value of *p*-value, the more sensitive a parameter was. Nonetheless, the null hypothesis was rejected if small value of *p*-value < 0.05, which would mean that the parameter exerted a significant impact on the dependent variable, thus it was sensitive

3.3.9 Calibration and Validation of SWAT model

After parametrization, using SUFI-2 algorithm, calibration was carried out between the periods 1978 and 1984, and validation in the period 1985 to 1990 using the observed data from 2FC05 (Table 1A, APPENDIX A). In SUF-2, uncertainty in parameters expressed as ranges accounted for all sources of uncertainties. The fit between the observation expressed as a single signal (with some error associated with it) and simulation result, expressed as 95PPU, was quantified by P-factor and R-factor statistics. The bandwidth of 95PPU was determined using the relation adapted from Singh et al. (2014) defined as:

$$\overline{d_x} = \frac{1}{k} \sum_{i=1}^{k} (x_u - x_l)_i \quad (3.9)$$

where x is the simulation value of stream flow, k was the number of stream flow simulations, x_l is the lower limit of 95PPU that corresponded to the 2.5 % probability at the cumulative probability curve, and x_u is the upper limit of 95PPU which corresponded to the 97.5 % probability at the cumulative probability curve. The R-factor, which represents the ratio of the

average width of the 95PPU band to the standard deviation of the measured variables as elucidated by Abbaspour et al. (2014), is determined as given in Equation 3.10.

$$R-factor=\frac{\overline{d_x}}{\sigma_x} \tag{3.10}$$

where, σ_x is the standard deviation of stream flow observation data x.

3.3.10 Assessment of SWAT Model Performance

The performance of SWAT model was evaluated by comparing the simulated and observed stream flow datasets using three commonly applied test statistics in hydrologic modelling; Percentage Bias (PBIAS), Nash Sutcliffe model efficiency (NSE), and Coefficient of Determination (R^2) as expressed in equations (3.11), (3.12), and (3.13) respectively. The performance rating analyses were carried out in accordance to the recommendations by Van Liew et al. (2003) and Moriasi et al. (2007).

$$R^2=\frac{\left[\sum_{i=1}^{n}\left(q_i^{obs}-q_i^{avg}\right)\left(Q_i^{sim}-Q_i^{avg}\right)\right]^2}{\sum_{i=1}^{n}\left(q_i^{obs}-q_i^{avg}\right)^2\sum_{i=1}^{n}\left(Q_i^{sim}-Q_i^{avg}\right)^2} \tag{3.11}$$

$$NSE=1-\frac{\sum_{i=1}^{n}\left(q_i^{obs}-Q_i^{sim}\right)^2}{\sum_{i=1}^{n}\left(q_i^{obs}-q_i^{avg}\right)^2} \tag{3.12}$$

$$PBIAS=\frac{n\sum_{i=1}^{n}\left(Q_{obs}-Q_{sim}\right)}{\sum_{i=1}^{n}Q_{obs}} \tag{3.13}$$

where, n is the total number of observations, q_i^{obs} is observed discharge, q_i^{avg} is average of the observed data, Q_i^{sim} is the simulated discharge, and Q_i^{avg} is the average of the simulated data.

3.4 Estimating Spatial and Temporal impacts of Climate variability on Stream flow

The long-term effects of climate variability on spatial and temporal distribution of stream flow was assessed by simulating hydrologic variables (potential and actual evapotranspiration, surface runoff, and water yield) under LULC of 1978 with different climatic scenarios. Stream flow and the aforementioned hydrologic variables were therefore simulated monthly and annually in every sub-catchment under the baseline decade (Sim1 = 1978-1987) and

subsequent decades (Sim2 = 1988-1997; Sim3 = 1998-2007; Sim4 = 2008-2017). The impact of climate variability on hydrologic variables (including stream flow) was then analysed based on the percentage differences between the simulated hydrologic variables of the subsequent decades and the baseline decade in every sub-catchment.

$$\text{Climate variability impact} = \left(\frac{S_s - S_b}{S_b}\right) \times 100 \tag{3.14}$$

where, S_s was the hydrologic variable (stream flow) under the changing climate, and S_b was the hydrologic variable at the baseline decade of 1978 LULC.

3.5 Forecasting of Climate variability Impact on Stream flow

Future scenario prediction of the impact of climate variability on stream flow was done by first forecasting air temperature and precipitation for the period (2018 – 2037) using a nonlinear autoregressive neural network. Forecasted temperature and precipitation were then used as an input to the developed integrated SWAT and ANN models for annual prediction of stream flow in future. The future impact of climate variability on stream flow was then estimated based on the percentage difference between the simulated stream flow in the 5th and 6th decades and the baseline decade.

3.5.1 Forecasting of Climate Variables

Temperature and precipitation were the only climate variables forecasted for the period (2018 – 2037). Precipitation and temperature significantly influence all the hydrological processes both directly and indirectly, hence, in this study, they were selected to design future climate variability scenarios. For the comparison purposes, the selection was also guided by the fact that nearly all the GCM and RCM studies in catchments within the East Africa region have focused on the projection of temperature and precipitation for future climate change impact assessments. A nonlinear autoregressive neural network as shown in Figure 3.5 was used for the time series forecasting.

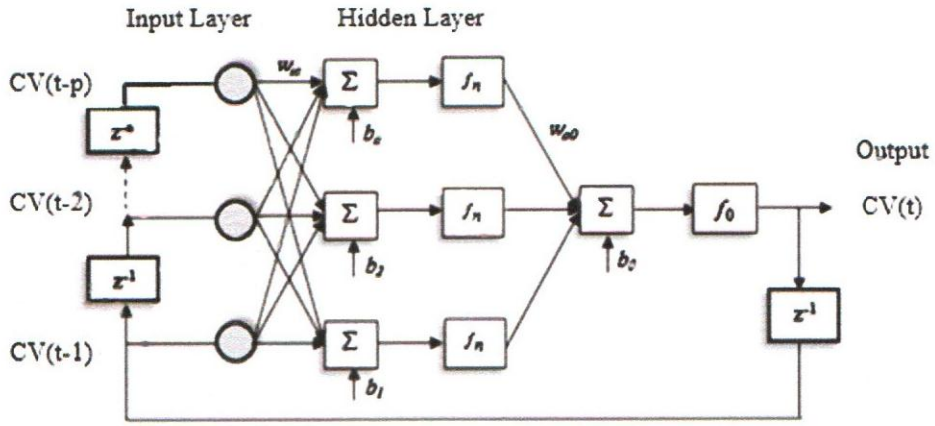

Figure 3.5: The NAR neural network used for forecasting of Climate variables

Forecasting models for annual precipitation and temperature were developed by the past values of the series for every month and this was guided by Equation (3.15) as illustrated by Ruiz et al. (2016). Levenberg-Marquardt backpropagation (Figure 3B, APPENDIX B) was adopted as the training algorithm because it is one of the most commonly applied learning procedures for the NAR networks (Alwakeel & Shaaban, 2010; Toushmalani, 2013).

$$(CV(t)) = h(CV(t-1), CV(t-2), \ldots, CV(t-p)) + \varepsilon(t) \tag{3.15}$$

The p features CV(t-1), CV(t-2),…,CV(t-p), were the feedback delays

For the forecasting, the value of a data series of a given climate variable (CV) (Temperature or precipitation) at time t, CV(t), using the p past values of the series. h(·) function was not known in advance, it was approximated by training a neural network using optimization of the network neurons and weight bias. And, ε(t) represented the error of the approximation of the series CV at time t. The objective function used was the mean square error.

$$MSE = \frac{SSE}{n} \tag{3.16}$$

$$SSE = \sum_{i=1}^{n} \left(\gamma_i - Y_i\right)^2 \tag{3.17}$$

where γ_i stands for the i-th data samples, $\bar{y}_i$ is the estimated values from the network for the value of Y_i and n the number of data samples for neural network training.

All the modelling computations and programming of the forecasting models development, training, testing, and validation were carried out in MATLAB. The model performance of comparing the trained model predictions with the actual values was carried out by the use of

statistical error indices, which included Root Mean Square Error, Mean Bias Error, and Coefficient of Determination as described in Equations (3.11), (3.18) and (3.19) respectively. Considering the monthly time step forecasting, the performance analyses of models developed was rated according to the recommendations by Nastos et al. (2014).

$$MBE = \frac{1}{n}\sum_{i=1}^{n}\left(y_i - x_i\right) \tag{3.18}$$

where, x_i is the measured average variable and y_i is the predicted average variable.

$$RMSE = \left(\frac{1}{n}\sum_{i=1}^{n}\left(y_i - x_i\right)^2\right)^{\frac{1}{2}} \tag{3.19}$$

where, x_i is the measured average variable and y_i is the predicted average variable.

3.5.2 Modelling Stream Flow in Future Scenario by Coupling SWAT and ANN

To forecast stream flow for the period (2018-2037) after the forecasting of mean annual temperature and precipitation, hybrid multivariate model based on coupling SWAT and ANN model was created. SWAT model was used as a transfer function to combine climate variables and geospatial data (Soil, DEM, and LULC) to simulate the hydrologic processes. The monthly simulated stream flow data after SWAT calibration were then used as target data against input data (historical mean monthly temperature and precipitation) for the training, testing, and development of the ANN forecasting model.

Input data (temperature and precipitation) and target data (simulated stream flow from SWAT) were first pre-processed for every month through standardization and normalization. Then, the data were divided into three samples which included 75 % for the training set, 12.5 % for validation, and 12.5 % for the test set. Finally, the programming and development of the forecasting models, training, testing, and validation were carried out in MATLAB version 2018b. Feedforward neural network trained with a backpropagation algorithm was adopted for forecasting stream flow for the periods (2018-2027) and (2028-2037). FNN was selected because it is the most popular multilayer neural network commonly used in hydrological modelling (Noor & Kalin, 2016; Senent et al., 2019; Singh et al., 2014).

The output of the FNN forecasting model could be expressed as;

Stream flow (Q) = f (n) (3.20)

Where, $n = \sum_{i=1}^{j} w_i x_i + b; x_1, x_2, ..., x_j$ were the input signals, x_1, x_2 were the inputs to the FNN model (forecasted precipitation and temperature), $w_1, w_2, ..., w_R$ were nodes synaptic weights, b was the bias value, and $f(.)$ was the FNN transfer function (Log Sigmoid).

Feedforward backpropagation neural network architecture adopted for forecasting stream flow is shown in Figure 3.6.

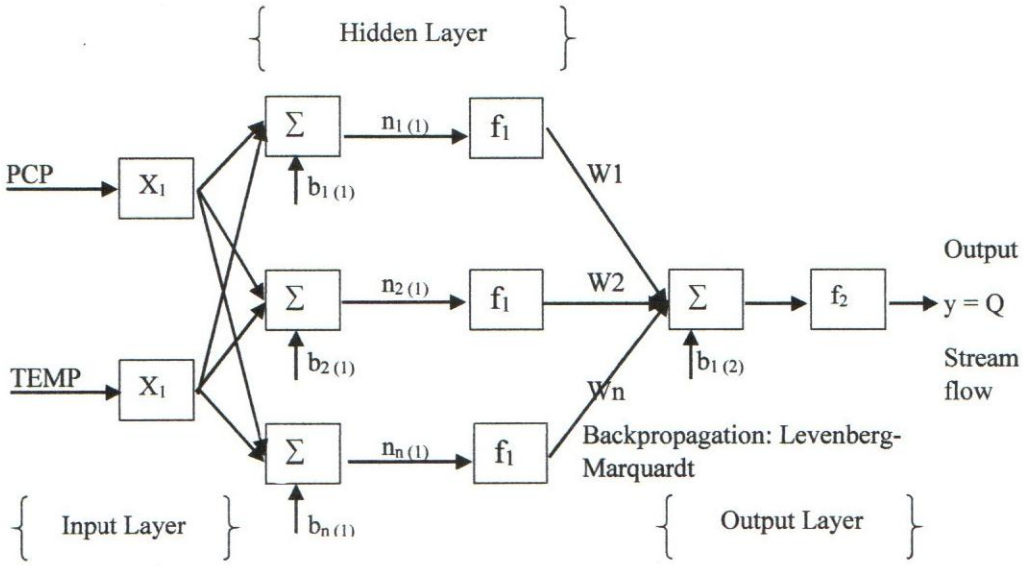

Figure 3.6: FNN-backpropagation topo logy used for stream flow forecasting

Once the training of FNN was initiated, where SWAT simulated stream flow dataset was applied as the target, the inputs were multiplied by weights and summed at each hidden unit. Then the summed input signal was mapped by the nonlinear log sigmoid activation function through several processes of iteration to target data for the creation of a forecasting model. The output was achieved according to Equations (3.21) and (3.22).

$$y = \sum_{i=1}^{j} w_{1,i(2)} \times \left(\frac{1 - \exp^{-\left(\sum_{i=1}^{j} w_{i,j(1)} x_i + b_{i(1)}\right)}}{1 + \exp^{-\left(\sum_{i=1}^{j} w_{i,j(1)} x_i + b_{i(1)}\right)}} \right) + b_{1(2),} \tag{3.21}$$

$$y_k = f_0 \left[\sum_{j=1}^{m} w_{jk} \times f_g \left(\sum_{j=1}^{n} w_{ij} x_i + b_k \right) \right] \tag{3.22}$$

Using the computations by the error backpropagation algorithm (Figure 3B, APPENDIX B), the weights were adjusted as follows;

$$E(w)=\frac{1}{2}\sum_{i=1}^{n}\left(Q_{mi}-Q_i\right)^2=\frac{1}{2}\left(Q_m-Q\right)^T\left(Q_m-Q\right) \tag{3.23}$$

where, Q_{mi} was the SWAT simulated stream flow (target data), Q_i was the network output (forecasted stream flow), and n was the number of training set elements.

Thus, the FNN biases and weights were updated as follows;

$$w=\left[\begin{array}{l} w_{1,1(1)},w_{1,2(1)},\cdots,w_{n,n(1)},b_{1(1)},b_{2(1)},\cdots,b_{n(1)},w_{1,1(2)},w_{1,2(2)} \\ ,\cdots,w_{1,n(2)},b_{1(2)} \end{array}\right]^T \tag{3.24}$$

Optimization was obtained by the use of error backpropagation algorithm in a sequential learning mode (Alwakeel & Shaaban, 2010). This successfully allowed the set of weights to be effectively modified after every exemplar processing as;

$$w_{ij}(n+1)=w_{ij}(n)+\Delta w_{ij}(n) \tag{3.25}$$

where, $\Delta w_{ij}(n)$ was the corresponding weight change, given as;

$$\Delta w_{ij}(n)=-\left(J^TJ+\varphi I\right)^{-1}.J^T\left(Q_m-Q\right) \tag{3.26}$$

where, J is the Jacobian matrix, I is the identity matrix, and φ is a scalar factor.

The convenient objective function adopted for the modelling process was the mean squared error (MSE). Performance efficiency of the model was analysed by comparing ANN predicted and SWAT simulated stream flow using R^2 and NSE as expressed in Equations (3.11) and (3.12). Rating for satisfactory performance analysis was then done as per Moriasi et al. (2007) and Nastos et al. (2014) recommendations. Using developed SWAT_ANN model with forecasted temperature and precipitation, stream flow was then predicted annually for the subsequent future decades (D5-(2018-2027); D6-(2028-2037)). The future impact of climate variability on stream flow was then evaluated as the percentage difference between the forecasted and baseline stream flow.

CHAPTER FOUR

RESULTS AND DISCUSSION

4.1 Trends of Climate Variables in Njoro River Catchment

Climate variables, which include precipitation, minimum and maximum air temperatures, relative humidity, wind speed, and solar radiation trends were determined both annually and monthly for the period 1978 to 2017 and each of the four decades (1978-1987, 1988-1997, 1998-2007, and 2008-2017) using Mann-Kendall trend analysis. The quantified significance of trends in climate variables was based on a two-tailed test at $p < 0.05$.

4.1.1 Trend Analysis of Annual Precipitation

The annual anomalies and temporal variation of precipitation analysed for the forty years as presented in Figure 4.1 revealed that the anomalies in precipitation over Njoro River catchment ranged between -36.0 % and +59.54 % of the long-term average. In this context, as pointed out by Rwigi (2014), values beyond + 24 % anomalies threshold were considered extreme wet while those beyond -24 % considered extreme dry climatic conditions.

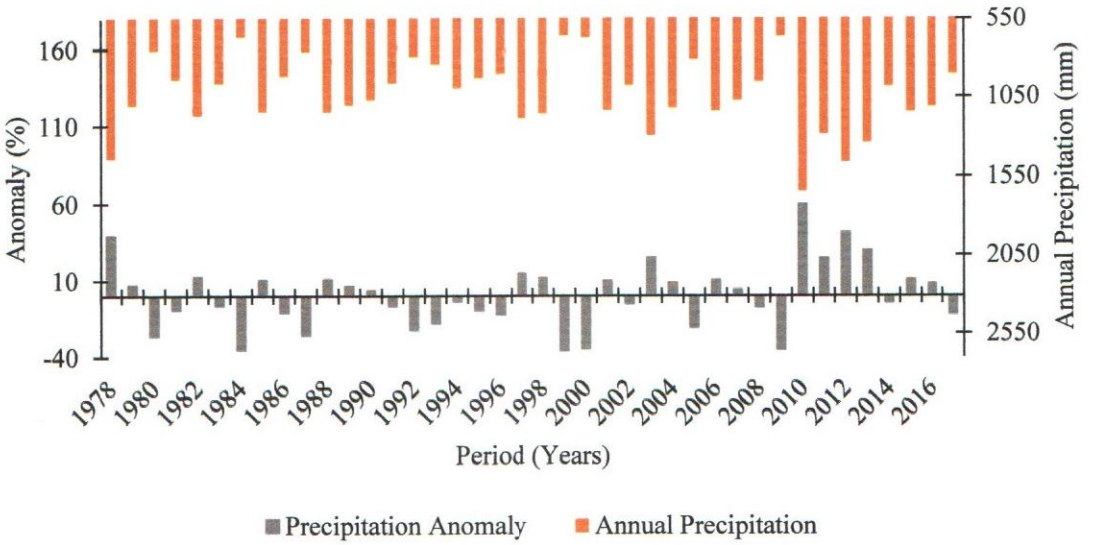

Figure 4.1: Mean annual anomaly and temporal variation of Precipitation at Egerton University weather station for the period (1978-2017)

As indicated in Figure 4.1, average precipitation for the 40 years was 1029.6 mm. Total number of days of precipitation changed from the baseline decade by 17.61 %, 15.65 %, and 10.51 % in the 2nd, 3rd, and 4th decades respectively. The lowest and highest recorded annual precipitations were 658.8 and 1642.6 mm in the years 1999 and 2010 respectively. According to the Mann-Kendall statistical analysis (S = 96 and Z_c = 1.12), annual precipitation had an

increasing trend in the forty-year period, which was not significant at $p < 0.05$. Mann-Kendall trend analysis results for individual four decades as shown in Table 4.1 further revealed a downward trend in annual precipitation in all four decades except for the 3rd decade. Both positive and negative precipitation trends (Table 4.1) were not significant at $p < 0.05$.

Table 4.1: MK trend results for annual Precipitation for the 4 Decades

Decade	Z_c	P-Value	Trend	Significance at $p < 0.05$ (two-tailed test)
1978-1987	-1.25	0.210	Decreasing	Not significant
1988-1997	-0.89	0.371	Decreasing	Not significant
1998-2007	0.36	0.721	Increasing	Not significant
2008-2017	-0.54	0.592	Decreasing	Not significant

It was noted that for the 40-year period, precipitation between July and December had a significant positive trend; nonetheless, precipitation between January and June had a downward trend that was not significant at $p < 0.05$ (Table 4A, APPENDIX A). The trend analysis results agreed with findings by Herrnegger et al. (2021), a study that reported annual precipitation increasing trends of the data obtained from Nakuru weather station (ID NO: 9036261) between the year 1980 and 2021. Also, annual precipitation of the data obtained at KARI, Njoro for the period 2009 to 2016 had an upward trend as reported by Mbote (2016). In contrast, Mwetu (2019) reports that annual precipitation between periods (1977-1984 & 1992-2000) in Njoro River catchment had a negative trend that was not significant at $p < 0.05$.

Although annual precipitation trends were not significant in any of the periods, the anomalies, temporal variation, and MK statistics for the periods (Jan-Jun & Jul-Dec) showed the manifestation of variability. The variability would affect the spatial as well as temporal response of inflow, storage, and outflow in a catchment hence changes in quantity and dynamics of stream flow. Inter-annual and inter-decadal precipitation variability at Njoro River catchment can be linked to the migration of the ITCZ due to its proximity to the equator. The movement of the ITCZ is sensitive to the ENSO (El Niño and La Niña) events and Sea Surface Temperature anomalies over the Indian Ocean (Mcsweeney et al., 2010; Ummenhofer et al., 2009). This implies that as the sea and ocean warming rates increase due to heat from the greenhouse gas emissions as elucidated in IPCC (2013), the time, intensity, distribution, and frequency of annual precipitation continue to greatly vary thus the trends as observed in Figure 4.1, Table 4.1, and Table 3A (Appendix A).

4.1.2 Trend Analysis of Monthly Precipitation

Monthly precipitation variation for the four decades at Njoro River catchment was computed as shown in Figure 4.2.

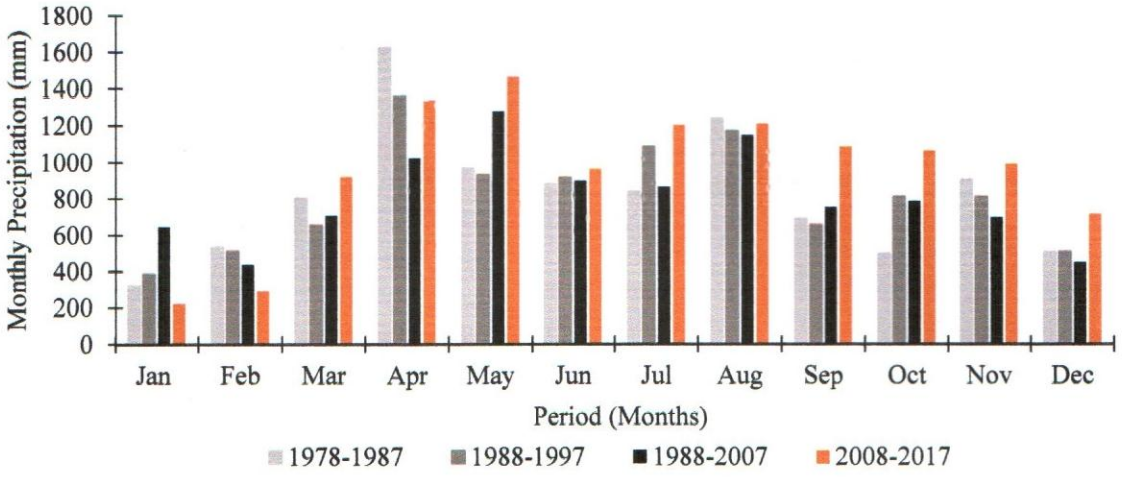

Figure 4.2: Monthly Precipitation variation for 4 decades

Monthly precipitation within a decade was lowest in January and highest in April at 392 and 1337 mm respectively (Figure 4.2). From the baseline decade, DJFM season precipitation changed by -4.91%, 3.61%, and -5.41% in the 2nd, 3rd, and 4th decades respectively, representing the largest precipitation decrease within a season. In the SON season, the precipitation changed in the 2nd, 3rd, and 4th decades by 8.62 %, 6.89 %, and 50.14 % respectively from the baseline decade representing the largest increase. A higher progressive increase in precipitation was observed in May, September, and October.

The monthly and seasonal variations of precipitation at Njoro River catchment could be associated with variations in the Hadley circulation that implies a twice-a-year relocation of ITCZ. The movements of the zone southwards over the equator through Kenya from October to December and returning northwards in March to May explains why Njoro River catchment experiences two distinct wet seasons with peaks currently in May and August. Dry season and months (DJFM) are associated with the effects of low-level north-easterly winds from Egypt and the Arabia Sea over equatorial East Africa in January and February (Camberlin, 2018). Mann-Kendall trend analysis results for monthly precipitation for the period (1978 - 2017) as shown in Figure 4.3 indicated that for the 40 years, precipitation in all the months had an increasing trend except in January, February, March, April, and December. Monthly

precipitation increasing trends were significant at $p < 5\%$ in May ($Z_c = 1.96$), September ($Z_c = 2.19$) and October ($Z_c = 2.21$).

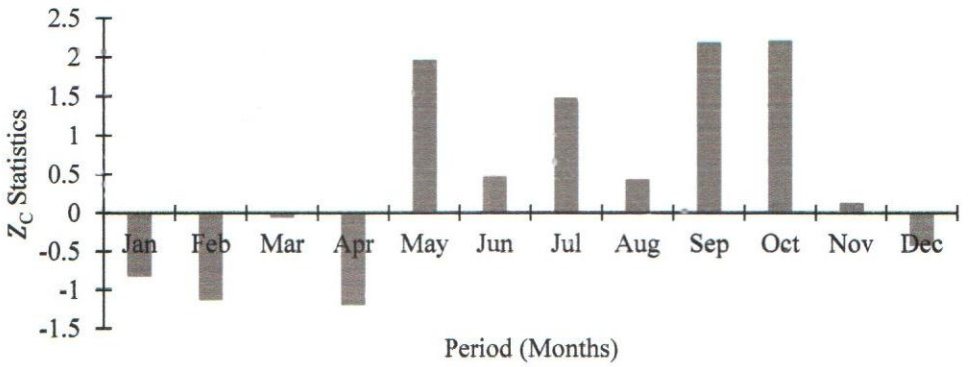

Figure 4.3: MK trend results for Monthly Precipitation in the period (1978-2017)

Precipitation negative trends in April and the significant positive trends in May were an indication of a shift of long-rain peaks. Also, the significant increasing trend in September was an indication of a probable future shift of precipitation peaks from August to September. The Z_c values for both dry and wet months (Figure 4.3) implied that the intensity and severity of dryness in future climatic scenarios are likely to intensify in DJFM and wetness in MJJ and SON seasons. In the case of each decade (Figure 4.4), precipitation trends for the baseline decade in all the months were not significant at $p < 0.05$ with the upward trends in May, September, and November.

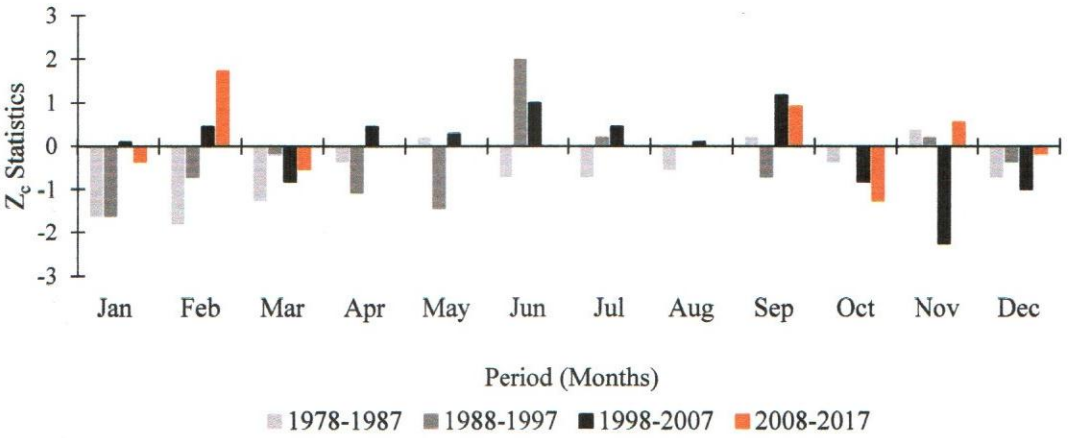

Figure 4.4: Monthly Precipitation Mann-Kendall Zc values for four decades

Monthly precipitation trends in the 2nd decade were all negative statistically not significant except for a significant upward trend in June. Z_c statistics revealed positive trend that was not significant in all the months except March, October, November, and December in the 3rd

decade. Only November had a significant negative precipitation trend at $p < 0.05$. The values of S and Zc statistics for the monthly precipitation in the 4th decade indicated that all the months had increasing trend which was not significant except declining trends in January, March, June, October, and December. The characteristics exhibited by the monthly precipitation variability from one decade to another (Figure 4.4) were sufficient evidence of unreliable changing weather patterns hence climate variability. The monthly precipitation variability showed a likelihood of changes in precipitation partitioning, where some months would experience extreme or declined runoff, subsurface flow, recharge, and return flow, thus stream flow variation.

4.1.3 Trend Analysis of Mean Annual Air Temperature

Mean annual temperature anomalies over Njoro River catchment as shown in Figure 4.5 for the forty years varied between -1.65 ^{0}C and +1.35 ^{0}C of the long-term average. The anomalies observed from the baseline decade to the last decade revealed a gradual rise in warming rates.

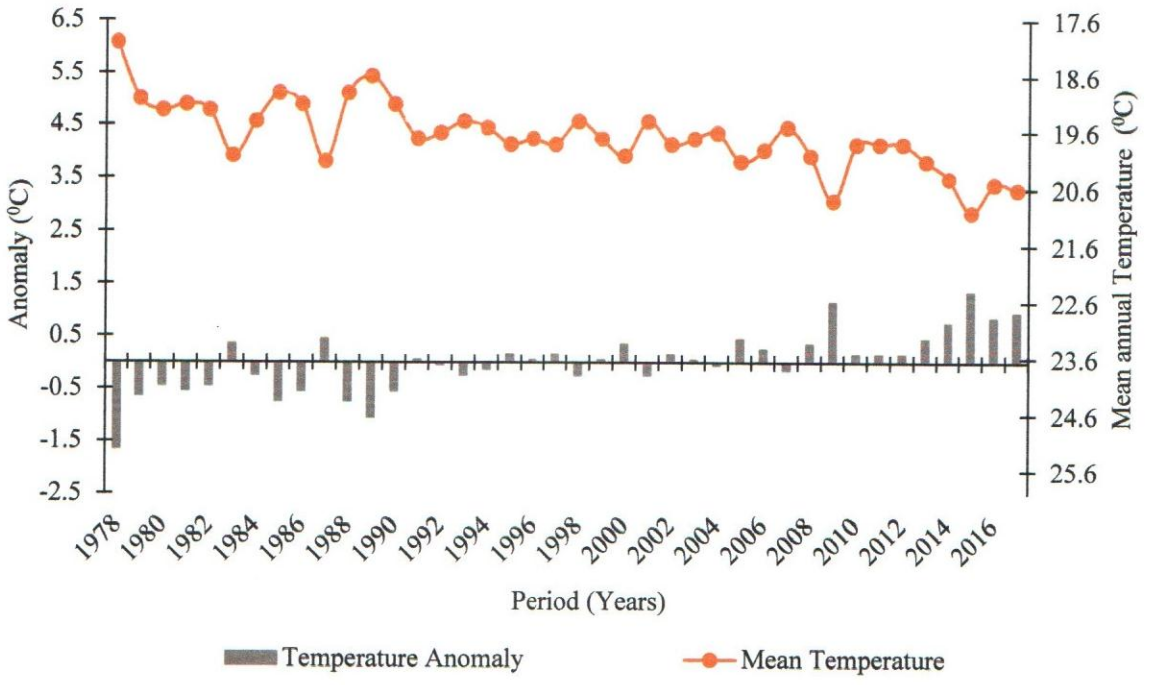

Figure 4.5: Mean annual anomalies and temporal variation of air Temperature at Egerton University weather station for the period (1978-2017)

From the results (Figure 4.5), it was revealed that the year 1987, 1997, 2005, and 2015 exhibited the highest temperature in the 1st, 2nd, 3rd, and 4th decades respectively, and this was attributed to the fact that the aforementioned four years were the driest in the 40 years. The lowest mean temperatures were recorded in the same years (1978 and 1989), which had higher

precipitation. Over the four decades, the mean annual air temperatures ranged from 18 ^{0}C to 21^{0}C. Mann-Kendall statistics (S = 419 and Z_c = 5.083) for mean annual temperature for the forty years revealed a positive trend that was statistically significant at $p < 0.05$.

The findings were consistent with global and regional surface temperature trends observations by IPCC (2014). Wambui et al. (2018) and Mwetu (2019) have also reported similar results of mean annual temperature trends at the Njoro River catchment. From the results, there was sufficient evidence of climate variability manifestation since the rate of warming increased from one decade to another. Warming rates due to the annual rise of mean temperature were attributed to variations in electromagnetic energy reaching earth's surface and alterations in the greenhouse effect as explained by (IPCC, 2014).

4.1.4 Trend Analysis of Annual Maximum Air Temperature

For the period (1978 - 2017), maximum air temperature anomalies over Njoro River catchment varied between -1.77 ^{0}C and +1.74 ^{0}C of the long-term average as given in Figure 4.6.

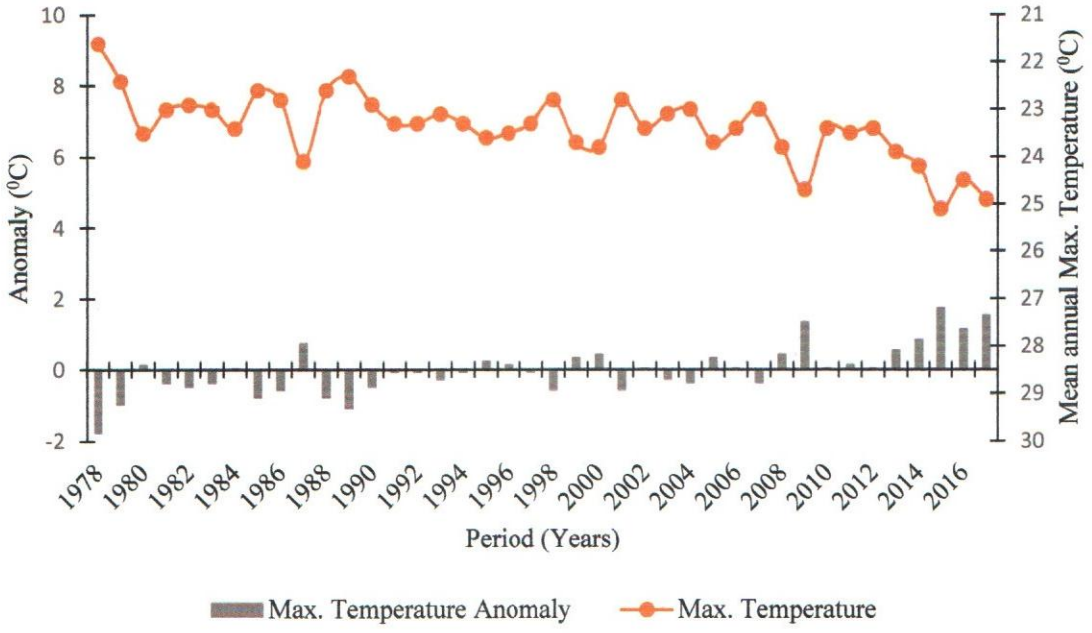

Figure 4.6: Mean annual anomalies and temporal variation of Max. Air Temperature at Egerton University weather station for the period (1978-2017)

The lowest (21.6 ^{0}C) and (25.1 ^{0}C) highest maximum air temperatures were in the years 1978 and 2015 respectively. Annual maximum air temperature for the forty years had a significant upward trend (S = 385 and Z_c = 4.488) at $p < 0.05$. Mann-Kendall results for individual four decades as illustrated in Table 4.2, revealed an upward trend in mean annual maximum air

temperatures in all the decades except for the third decade. Maximum air temperature variability as illustrated in Figure 4.6 and Table 4.2 implied that temperature in the daytime has been on the rise so is the soil and water resources temperatures. Warmer days due to the rising maximum air temperature may exacerbate the occurrence of extreme hydrologic events such as drought during periods of low precipitation, which would then contribute to changes in stream flow.

Table 4.2: MK trend results for annual Max. Air Temperature for the 4 Decades

Decade	Z_c	P-Value	Trend	Significance at $p < 0.05$ (two-tailed test)
1978-1987	1.17	0.243	Increasing	Not significant
1988-1997	2.41	0.016	Increasing	Significant
1998-2007	0	1	Decreasing	Not significant
2008-2017	1.71	0.087	Increasing	Significant

4.1.5 Trend Analysis of Monthly Maximum Air Temperature

Monthly maximum surface air temperature variations for the four decades were calculated as given in Figure 4.7.

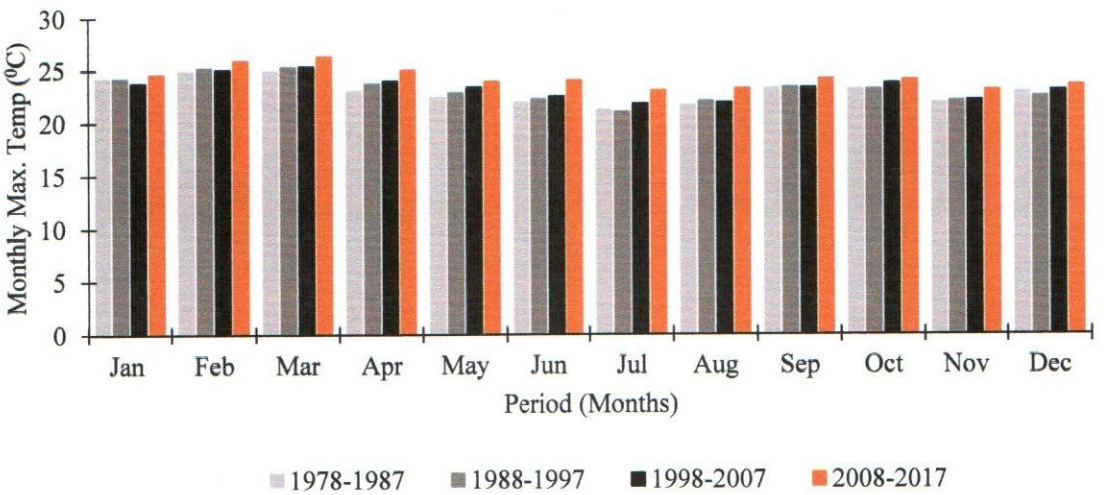

Figure 4.7: Monthly Maximum Air Temperature variation for 4 decades

Figure 4.7 results indicated that on average, February and March had the highest daytime temperature while June, July, and August had the lowest. The increment of monthly maximum air temperatures in the subsequent decades ranged from 0.04 ^{0}C to 1.1 ^{0}C. Based on Mann-Kendall results (Z_c-values) as presented in Figure 4.8, maximum air temperature had significant

increasing trend at $p < 0.05$ in all the months for the forty years except in January and February. It was noted that the months with higher maximum air temperature upward trends were the same months with higher precipitation. This could be attributed to the fact that a dry atmosphere enhances heat loss to space in the form of longwave radiation emitted by the earth, and complete coverage of clouds trap, absorb and convert most of the outgoing radiation into heat, hence increase in temperature.

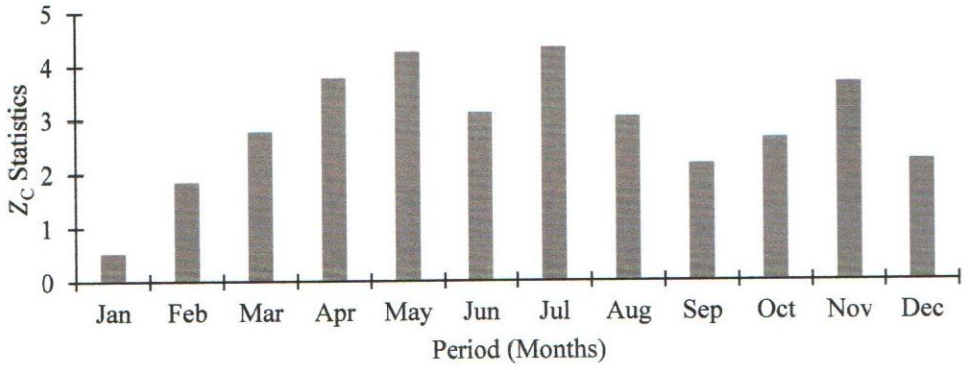

Figure 4.8: MK trend results for Monthly Max. Temperature in the period (1978-2017)

In the case of MK analysis in the four decades, maximum air temperature had an increasing trend in all the months in 1st and 2nd decades except June in the 1st decade (Figure 4.9).

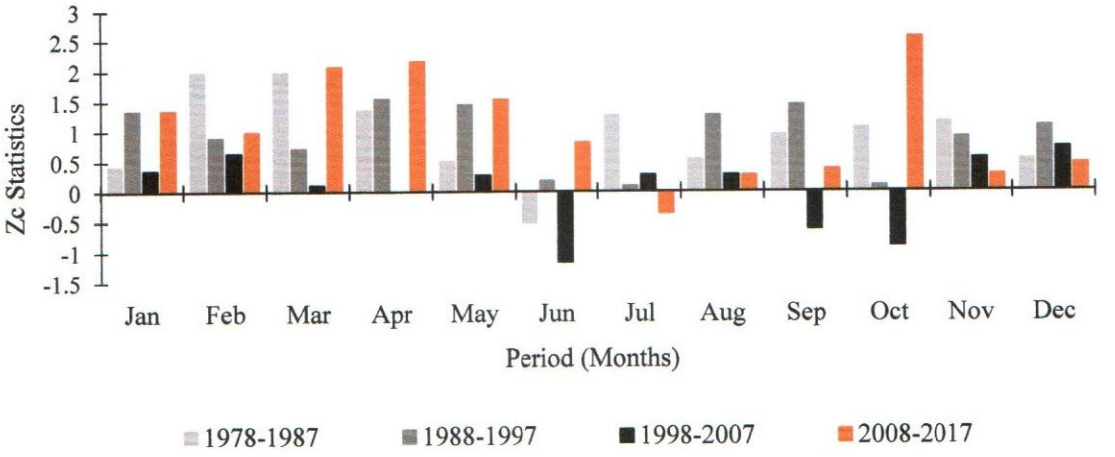

Figure 4.9: Monthly Max. Air Temperature Mann-Kendall Zc values in the four decades

Significant positive trends at 5% significance levels were only detected in the first decade in February, March, and April (Figure 4.9). Monthly maximum air temperatures for the last two decades had an upward trend with exceptions in June, September, and October for the period (1998-2007) and July for the duration (2008-2017). The positive trends of maximum temperatures in March, April, and October in the 3rd decade were significant at $p < 0.05$ (Figure

4.9). Maximum temperature changes in subsequent decades revealed the manifestation of climate variability at Njoro River catchment, thus variations in time, space, and intensity of evapotranspiration, which would then influence surface runoff and base flow.

4.1.6 Trend Analysis of Annual Minimum Air Temperature

The anomalies and mean annual minimum air temperature distribution over the Njoro River catchment for the period 1978 to 2017 is shown in Figure 4.10. The year 1979 had the lowest (9.1 ^{0}C) recorded minimum temperature while 2016 had the highest (14.8 ^{0}C). Based on the results, the anomalies in minimum air temperature varied between -4.28 ^{0}C and +1.42 ^{0}C of the long-term average.

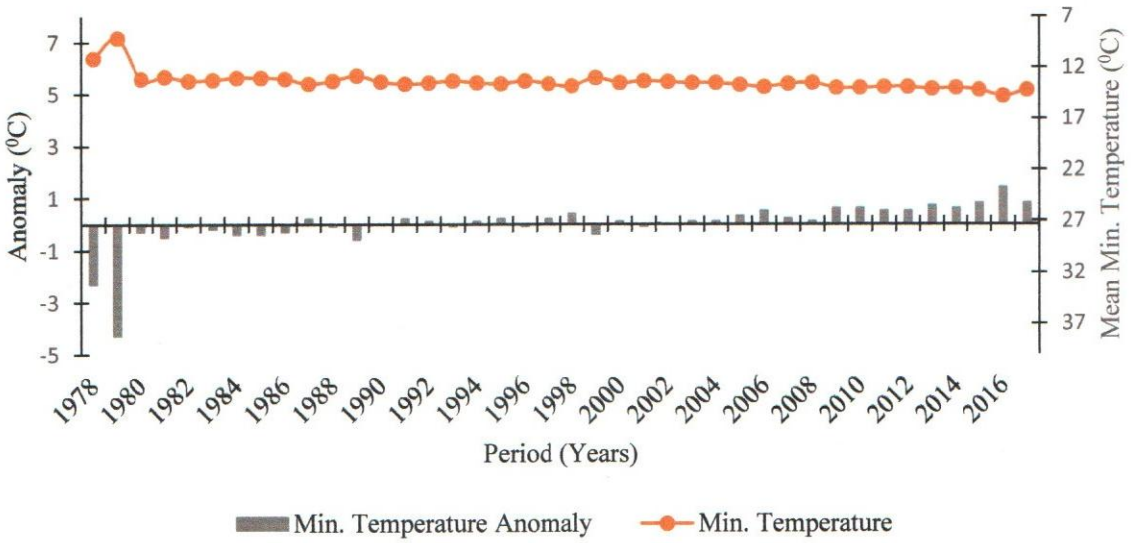

Figure 4.10: Mean annual anomalies and temporal variation of Min. Air Temperature at Egerton University weather station for the period (1978-2017)

The anomalies (Figure 4.10) indicated a progressive increase of warmer nights from the 1st decade to the subsequent decades. Results from the Mann-Kendall statistics (S = 504 and Z_c = 6.119) revealed that annual minimum air temperature for the forty years had an increasing trend that was significant at $p < 0.05$. Further, as presented in Table 4.3, the annual minimum air temperature had a positive trend in all the decades with the significant trend detected in the last decade. The temporal variation and trends as exhibited by minimum air temperature (Figure 4.10 and Table 4.3), provided statistical evidence that night temperature has been on the rise. This was associated with reduction of radiation negative balance intensity, due to an increase in invisible water vapour as well as greenhouse gases in the atmosphere hence climate variability.

Table 4.3: MK trend results for annual Min. Air Temperature for the 4 Decades

Decade	Z_c	P-Value	Trend	Significance at $p < 0.05$ (two-tailed test)
1978-1987	1.80	0.071	Increasing	Not Significant
1988-1997	1.39	0.163	Increasing	Not Significant
1998-2007	1.54	0.123	Increasing	Not Significant
2008-2017	2.47	0.013	Increasing	Significant

4.1.7 Trend Analysis of Monthly Minimum Air Temperature

Monthly minimum air temperature variation for the four decades as presented in Figure 4.11 showed that months with higher precipitation had warmer nights than months with lower precipitation, and July had the coolest nights. These observations were associated with the seasonal variability of negative radiation balance.

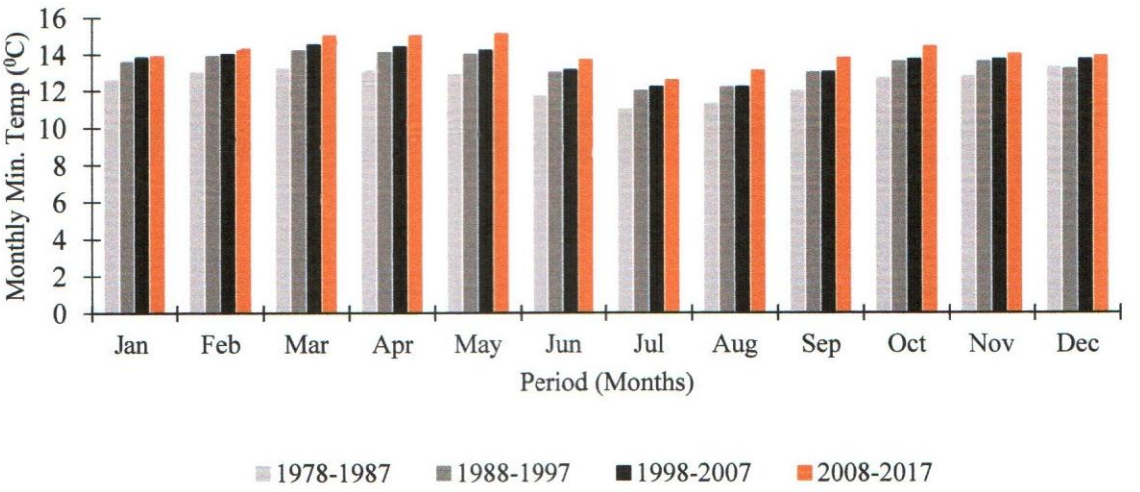

Figure 4.11: Monthly Min. Air Temperature variation for 4 decades

Mean monthly minimum temperatures (Figure 4.11) ranged from about 11 ^{0}C (July) to about 15 ^{0}C (March). The monthly minimum air temperature progressive increase in the subsequent decades varied from 0.1 ^{0}C to 1.0 ^{0}C. According to Mann-Kendall statistics (Z_c) for the forty years, as shown in Figure 4.12, the minimum air temperature had a significant increasing trend at $p < 0.05$ in all the months. Such observations of monthly minimum air temperature may hint at a declining rate of heat loss to space and variability of atmospheric water content.

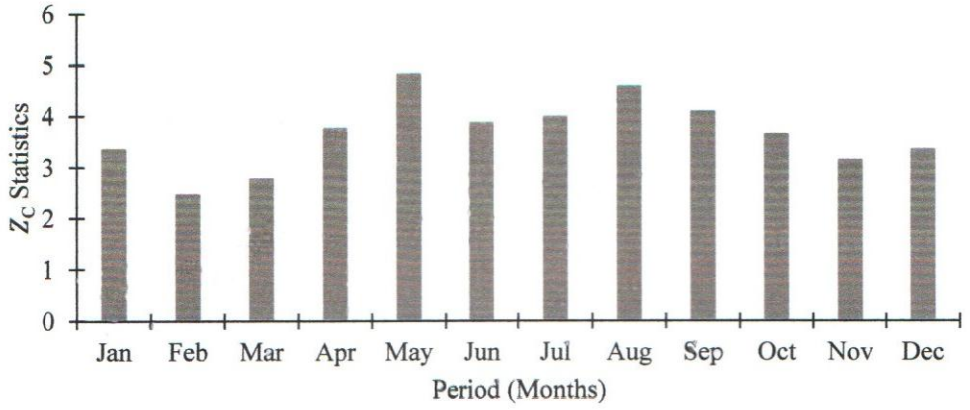

Figure 4.12: MK trend results for Monthly Min. Temperature in the period (1978-2017)

In the case of the individual four decades (Figure 4.13), Mann-Kendall statistics (Z_c) show that minimum air temperatures in all the months of the baseline decade had an upward trend that was not significant at $p < 0.05$.

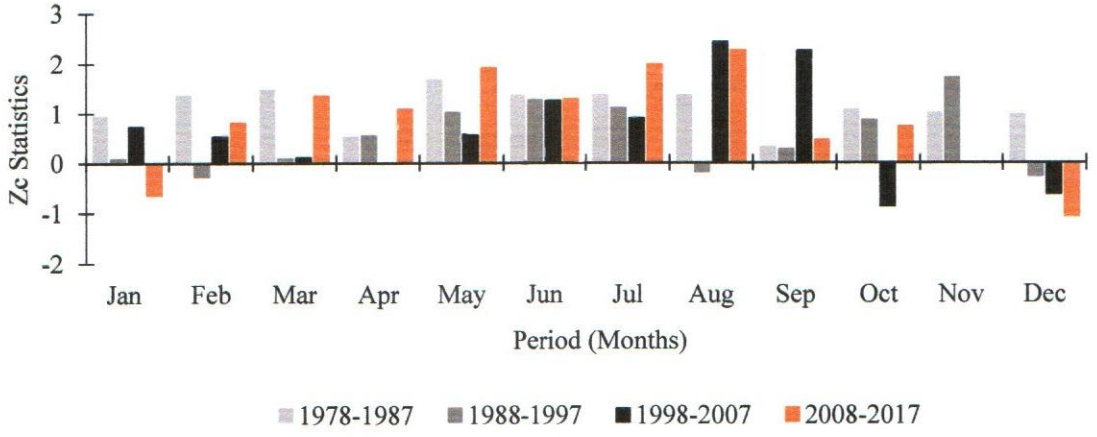

Figure 4.13: Monthly Min. Air Temperature Mann-Kendall Zc values in the four decades

Minimum air temperature had a positive trend in the 2nd decade in all the months except February, August, and December, and the trends were not significant at $p < 0.05$ (Figure 4.13). In addition, minimum temperature had an upward trend in all the months of the third decade except October and December. In the same decade, the minimum air temperature in August and September had a significant positive trend $p < 0.05$. A positive trend in minimum air temperatures also existed in all months of the fourth decade except January and December. However, a significant upward trend of minimum air temperature in the 4th decade was detected in May, July, and August $p < 0.05$.

4.1.8 Trend Analysis of Annual Relative Humidity

Mean annual anomalies and temporal variation of relative humidity analysed for the forty years (1978-2017) are presented in Figure 4.14.

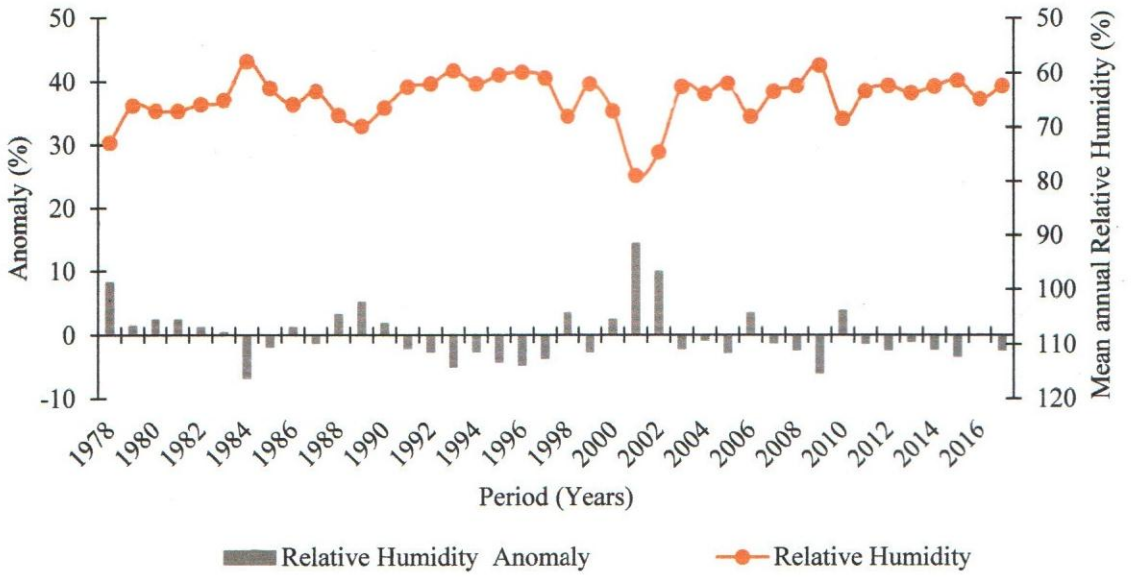

Figure 4.14: Mean annual anomalies and temporal variation of Relative Humidity at Egerton University weather station for the period (1978-2017)

From Figure 4.14 it was noted that between 1978 and 2017 the anomalies in relative humidity over Njoro River catchment ranged between -6.71 % and +14.38 % of the long-term average. Average relative humidity for the 1st, 2nd, 3rd, and 4th decades was, 65.48 %, 63.18 %, 67.32 %, and 62.93 % respectively. Maximum and minimum recorded relative humidity in the forty years were 79 % (year-2001) and 57% (year-1984). Mann-Kendall trend analysis for the forty years revealed that annual relative humidity had a decreasing trend ($S = -122$ and $Z_c = -1.411$), which was not significant at $p < 0.05$. Although the relative humidity negative trend was not significant, the slight temporal variations (Figure 4.14) were indications of the changing atmospheric saturation deficit.

Mann-Kendall trend analysis results of relative humidity for individual four decades is shown in Table 4.4.

Table 4.4: MK trend results for annual Relative Humidity for the 4 Decades

Decade	Z_c	P-Value	Trend	Significance at $p < 0.05$ (two-tailed test)
1978-1987	-2.344	0.019	Decreasing	Significant
1988-1997	-2.604	0.009	Decreasing	Significant
1998-2007	0.628	0.53	Decreasing	Not Significant
2008-2017	0.090	0.927	Increasing	Not Significant

Table 4.4 results indicated that the annual relative humidity in the baseline and second decade had a significant downward trend while the third and fourth decades had negative and positive trends respectively that were not significant at $p < 0.05$. The Z_c values revealed the variability of both humid and dry air for the four decades over Njoro River catchment, which implied changes in evapotranspiration. Moreover, the transportation of vapour away from the evaporative surfaces depends on the specific humidity gradient in the air above it.

4.1.9 Trend Analysis of Monthly Relative Humidity

As shown in Figure 4.15 the lowest and highest average monthly relative humidity within a decade was in February (51.50 %) and July (75.25 %) respectively.

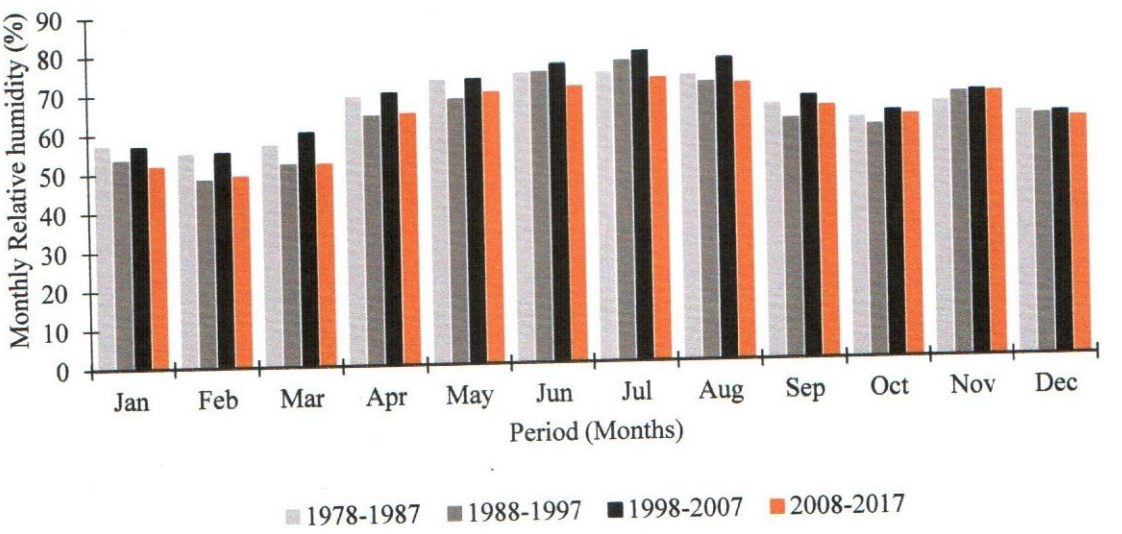

Figure 4.15: Monthly Relative Humidity variation for the 4 decades

Dry months (DJFM) had the lowest average relative humidity while the coolest months (JJA) had the highest (Figure 4.15). The progressive decline of relative humidity as exhibited in all months except in July, October, and November was not significant at $p < 0.05$ (Figure 4.16).

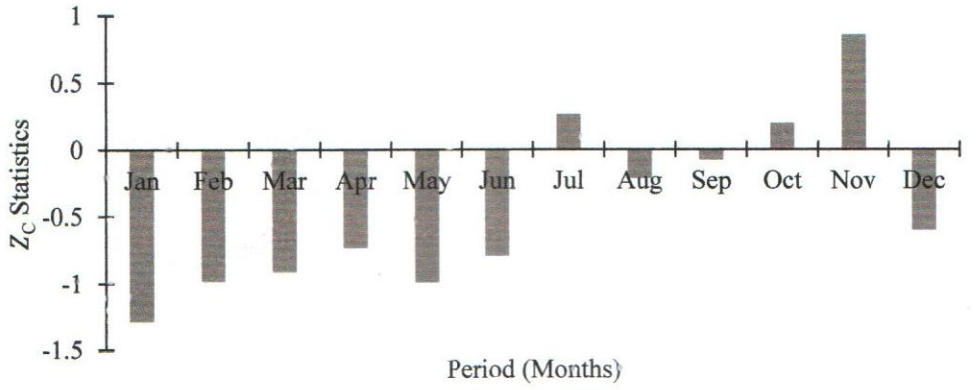

Figure 4.16: MK trend results for Monthly Relative Humidity in the period (1978-2017)

Extreme declining trends experienced in nearly all dry months were an indication of the continued presence of dry air in the dry season. Relative humidity in November showed an extremely positive trend out of all the months, and this was consistent with the fact that November also had a high positive trend in precipitation. The Mann-Kendall Z_c statistics for monthly trend analysis in each decade as shown in Figure 4.17 indicated that in the baseline decade, relative humidity had a negative trend in all the months except April, and the decreasing trend was significant at $p < 0.05$ only in February.

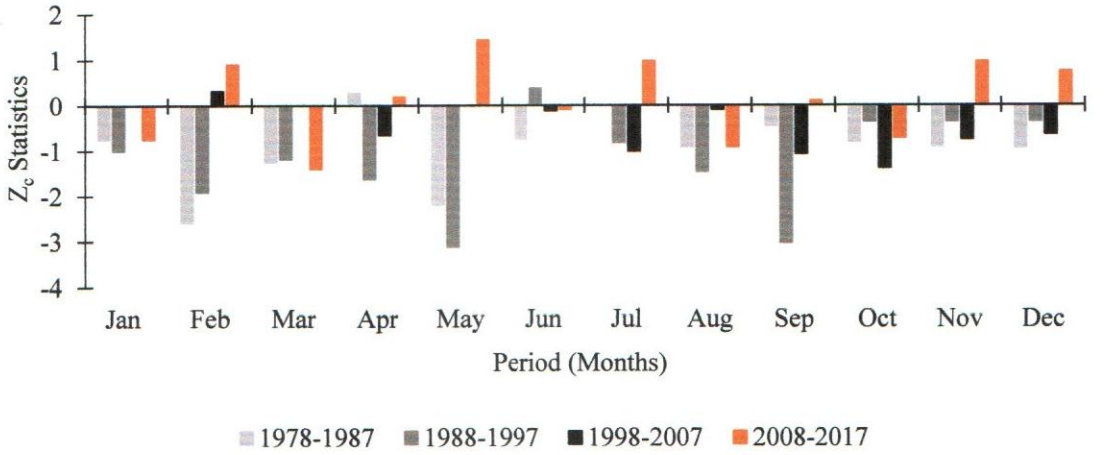

Figure 4.17: Monthly Relative Humidity Mann-Kendall Zc values for the four decades

Monthly relative humidity had a declining trend in all months in the second decade except in June, where the negative trends were significant in May and September. In the third decade, January and May recorded no trend, and the remaining months had a downward trend, which was not significant at $p < 0.05$ (Figure 4.17). The monthly relative humidity in the last decade

exhibited no significance where February, April, May, July, September, November, and December had upward trends and the remaining months had a downward trend.

4.1.10 Trend Analysis of Annual Wind Speed

Mean annual anomalies and temporal variation of wind speed results is given in Figure 4.18. Wind speed anomalies for the period (1978-2017) ranged between -2.32 and 1.53 km/h of the long-term average.

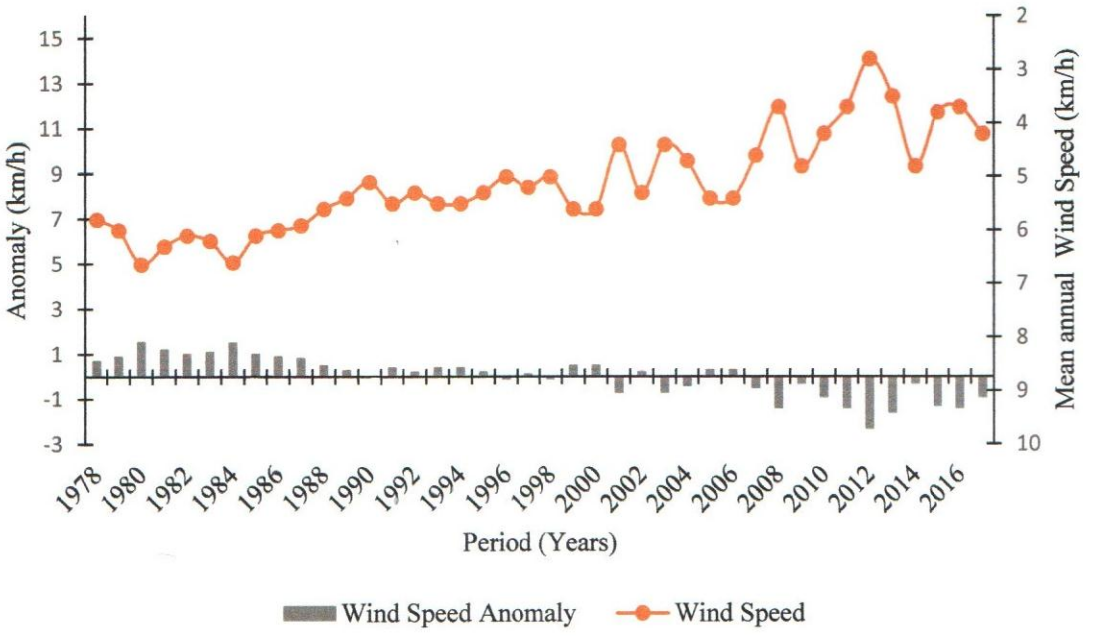

Figure 4.18: Mean annual anomalies and temporal variation of Wind Speed at Egerton University weather station for the period (1978-2017)

Based on Figure 4.18 results, the average wind speed for the forty years was 5.11 km/h. Average wind speed for the 1st, 2nd, 3rd, and 4th were, 6.17 km/hr, 5.34 km/hr, 5.04 km/hr, and 3.92 km/hr respectively. Annual average minimum and maximum wind speeds were 2.8 km/h in 2012 and 6.64 km/h in 1980. Annual wind speed was higher in the baseline years than the years in the subsequent decades. Mann-Kendall statistics ($S = -543$ and $Z_c = -6.33$) for the forty years indicated that the wind speed decreasing trend was statistically significant at $p < 0.05$. Further, Mann-Kendall trend statistics of the annual wind speed for each of the four decades as presented in Table 4.5 showed a declining trend in all the decades except the last decade, which had no trend. However, the negative trends were not significant at $p < 0.05$. The annual wind speed variability as showed in Figure 4.18 and Table 4.5 implied a likelihood of changes in

evapotranspiration since the transportation of vapour away from the land and vegetation surfaces primarily depends on wind velocity.

Table 4.5: MK trend results for annual Wind Speed for the 4 Decades

Decade	Z_c	P-Value	Trend	Significance at $p < 0.05$ (two-tailed test)
1978-1987	-0.36	0.718	Decreasing	Not Significant
1988-1997	-0.45	0.646	Decreasing	Not Significant
1998-2007	-0.45	0.650	Decreasing	Not Significant
2008-2017	0	1	-	-

4.1.11 Trend Analysis of Monthly Wind Speed

Monthly wind speed variation for the four decades as presented in Figure 4.20 indicated that August had the lowest average wind speed (4.5 km/h) and February had the highest (6.02 km/h).

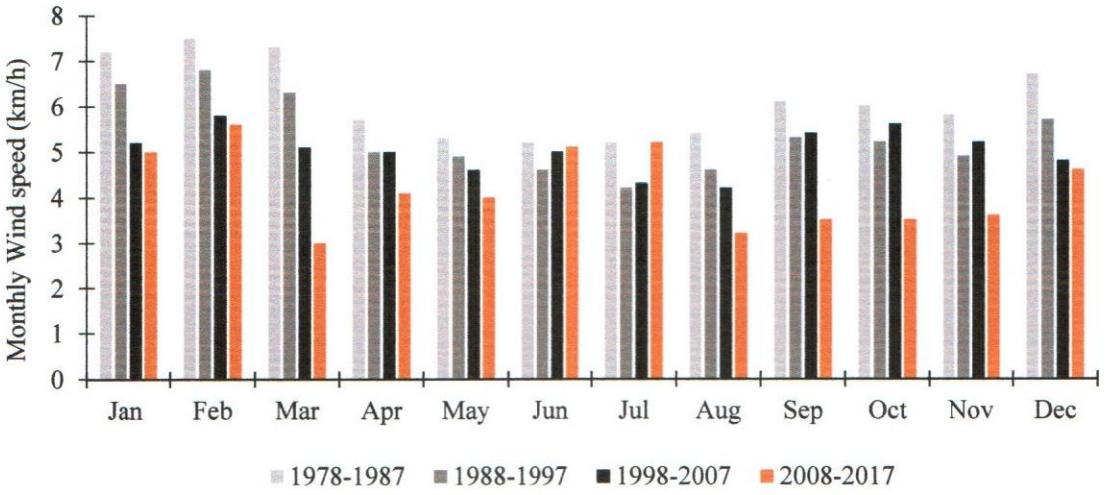

Figure 4.19: Monthly Wind Speed variation for the 4 decades

It was also noted that the dry months had a higher wind speed than the wet months (Figure 4.19). The lowest wind speed was experienced within the coolest months (June and July). Average monthly wind speed was higher in the baseline decade than in three subsequent decades. The monthly wind speed Mann-Kendall trend results for the forty years as presented in Figure 4.20 showed that the progressive decreasing trend exhibited in all months was significant at $p < 0.05$.

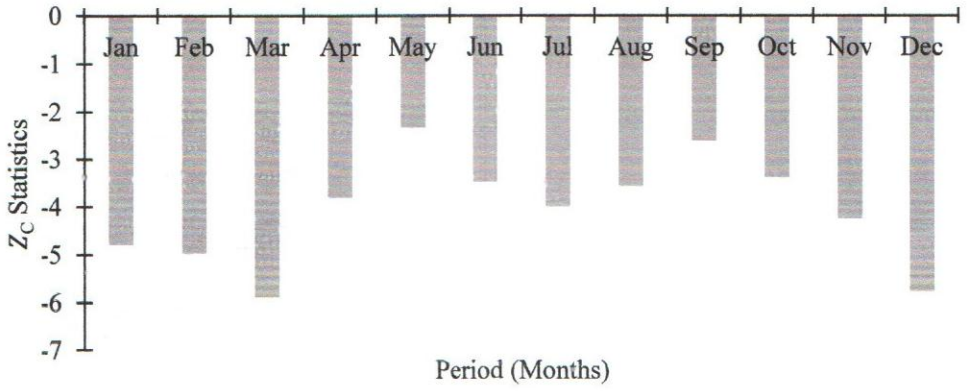

Figure 4.20: MK trend results for Monthly Wind Speed in the period (1978-2017)

The declining trend of wind speed was extreme in dry months. It implied that DJFM season had higher variabilities in the ability to transport the vapour away from the evaporative surfaces hence changes in both potential and actual evapotranspiration. In the case of individual decades, Mann-Kendall Z_c-values as illustrated in Figure 4.21 for monthly wind speed trend analysis indicated that the first decade experienced negative trends in all months except February, March, April, and August.

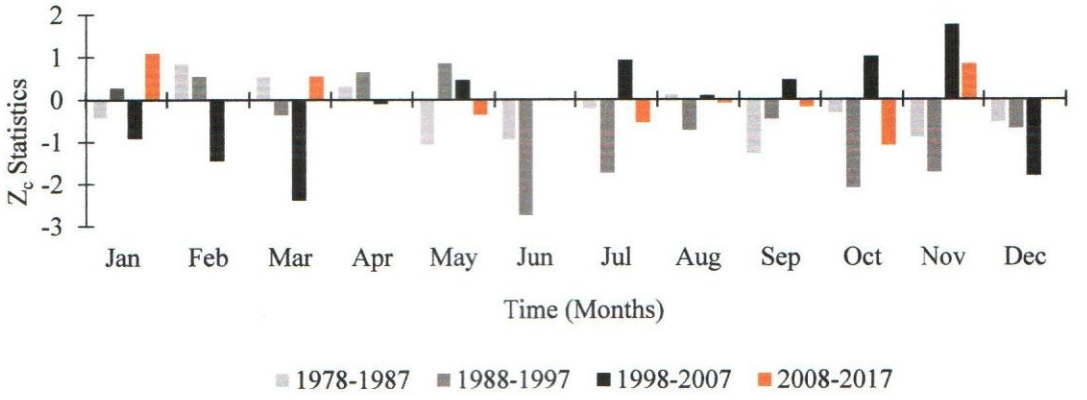

Figure 4.21: Monthly Wind Speed Mann-Kendall Zc values for four decades

Further, all the monthly wind speed trends were not significant in the baseline decade. Monthly wind speed in the 2nd decade had a statistically significant (at $p < 0.05$) downward trend in June and October (Figure 4.21). Also, wind speed in April and May showed a positive trend which was not significant. The Mann-Kendall Z_c statistics in the 3rd decade revealed an increasing trend in all the months except January, February, March, April, and December. Z_c statistics in the 4th decade showed that wind speed in all the months had a decreasing trend that was significant except in January, March, and November and no trend in April and December.

4.2 Modelling Stream flow Response to Climate Variability

The results obtained from SWAT Hydrological Modelling were divided into six areas as presented in the following sub-sections. They included catchment delineation and parameterization, parameters sensitivity analysis, calibration and validation, and spatial and temporal simulation of hydrologic variables.

4.2.1 Catchment Delineation

Based on the projected DEM at WGS_1984_UTM_Zone_36s, the catchment was divided into discrete land areas and streams reach that drain to a single outlet (at 2FC05-RGS), which in turn enabled the establishment of the upstream-downstream geospatial relationship. ArcSWAT watershed delineator demarcated a total area of 11493.96 ha, which was partitioned into 23 sub-catchments as shown in Figure 4.22.

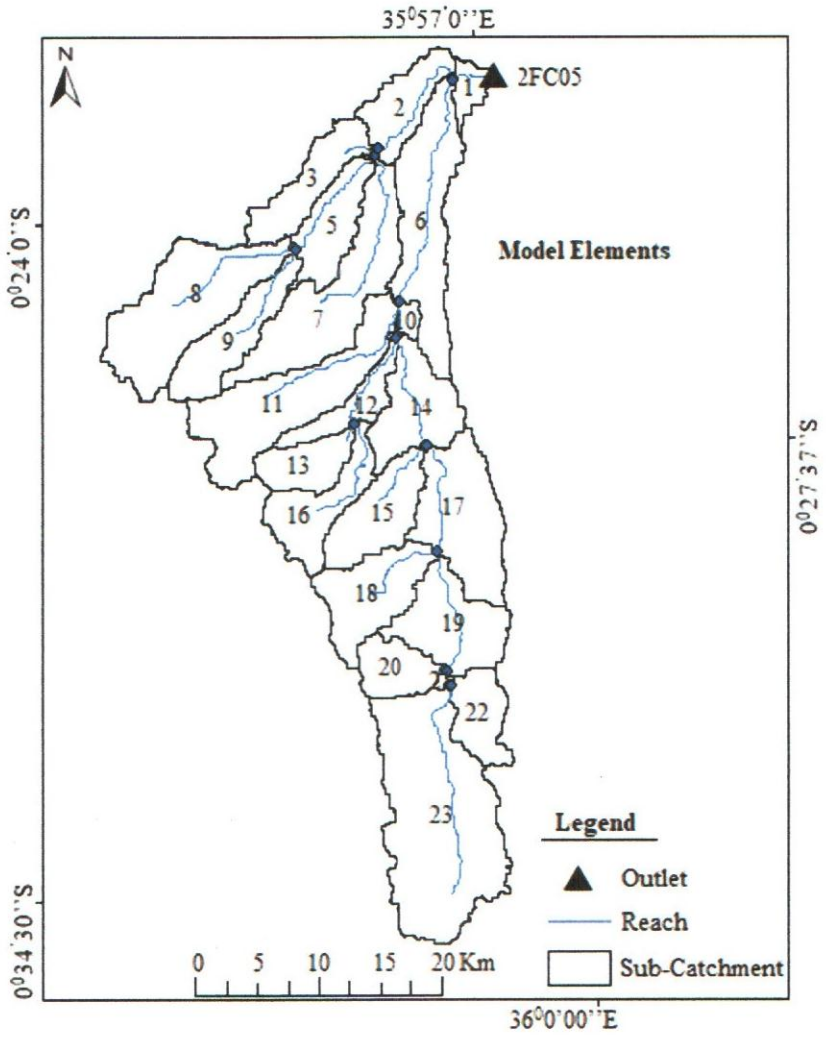

Figure 4.22: Stream distribution in the delineated Sub-catchments

Delineation extent was confined to upper Njoro River catchment for hydrological modelling purposes because 2FC05 river gauging station was the only outlet point with a relatively reliable longer and continuously available discharge dataset for calibration and validation. Sub-catchment 4 was the smallest (5.8 ha) while the largest was the sub-catchment 23 with total coverage of 1549.9 ha. Sub-catchment 1, the area that encloses the outlet of upper Njoro River catchment (2FC05_RGS) and Egerton confluence was at the lowest point at 2304.0 m above sea level. However, the sub-catchment 20, which covered areas around Eastern Rift Escarpment was at the highest point at 2885.5m above sea level. Sub-catchment 4 had the least slope of 4.9 % and sub-catchment 13 had the highest slope of 24.77%. The 23 sub-catchments were further partitioned into 48 hydrological response units based on the topographic, heterogeneity of the LULC, slope, and soil type as shown in Figure 4.23.

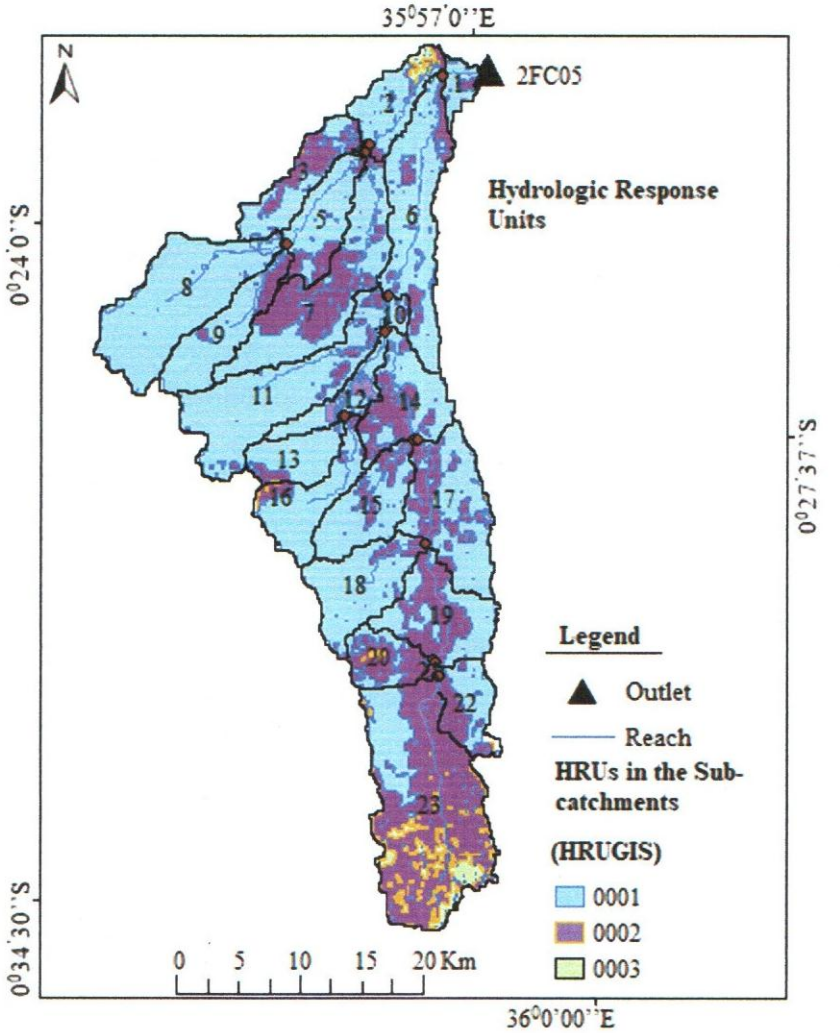

Figure 4.23: Stream distribution in the Hydrologic Response Units

Soil Conservation Service-Curve Numbers (SCS-CN) parameters were computed for each sub-catchment and hydrologic response unit. The spatial distribution of CN values for different antecedent moisture conditions as derived by ArcSWAT from the combination of topographic parameters, LULC of 1978 and rasterized Andosols soil for each sub-catchment are presented in Figure 4.24.

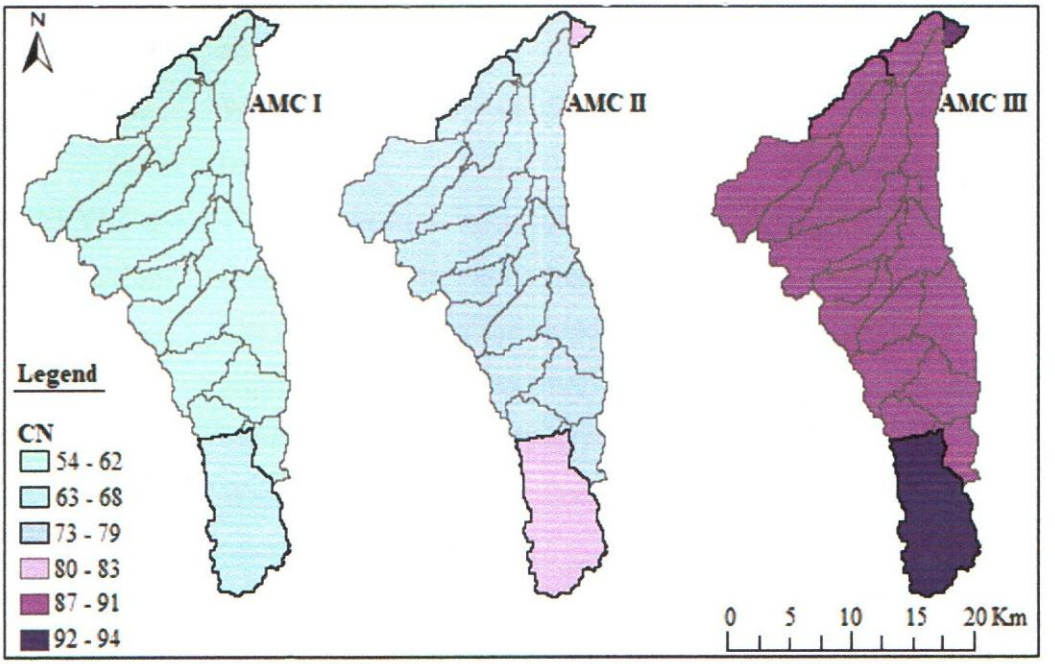

Figure 4.24: Spatial distribution of CN used for SWAT surface runoff simulations

The pattern exhibited by CN brings about the spatial disparity of simulated hydrologic variables (WYLD=SURQ+LATQ+GWQ-TLOSS) in the catchment, hence the variation in stream flow from one HRU or sub-catchment to another. Sub-catchments 1 and 23 had higher values of CN than the other sub-catchments (Figure 4.24). This was attributed to the fact that the two aforementioned sub-catchments were characterized by mainly bare and agricultural land systems. It implied that these sub-catchments had a higher potential to generate surface runoff and a lower potential for maximum water yield. On the other hand, sub-catchments 11, 13, and 16 had the lowest CN since the area was characterized by forest cover.

4.2.2 Sensitivity Analysis of SWAT Parameters

According to the results as illustrated in Table 4.6, the most sensitive parameters in Njoro River catchment were SCS curve number for antecedent moisture condition (II) (CN2) and initial depth of water in the shallow aquifer (SHALLST) ranked according to the highest sensitivity tested at $p < 0.05$.

Table 4.6: Sensitivity Analysis of Parameters

Parameter Name	Description	Degree of sensitivity		Rank
		t-stat	p-value	
v_CN2.mgt	SCS runoff curve number for moisture condition II	15.829	0.0000	1
r_SHALLST.gw	Water in the shallow aquifer initial depth (mm)	4.001	0.0000	2
v_GW_SPYLD.gw	The shallow aquifer specific yield (m^3/m^3)	3.485	0.0005	3
r_RCHRG_DP.gw	Deep aquifer percolation fraction (fraction)	3.255	0.0012	4
v_GWQMN.gw	The shallow aquifer threshold depth required for return flow (mm)	3.165	0.0016	5
r_CH_N2.rte	Manning's n value for main channel	3.120	0.0019	6
V_SOL_AWC.sol	Water storage capacity of available soil (mm H2O/mm soil)	2.95	0.0032	7
r_GW_DELAY.gw	Delay time (days) of groundwater	2.847	0.0046	8
v_SURLAG.bsn	Lag time (days) of Surface runoff	2.504	0.0126	9
r_ESCO.bsn	Compensation factor of Soil evaporation	2.367	0.0183	10
r_CH_K2.rte	The main channel effective hydraulic conductivity (mm/h)	2.092	0.0369	11
r_EPCO.hru	Compensation factor of Plant uptake	2.067	0.0392	12
v_ALPHA_BF.gw	Base flow alpha factor (days)	1.941	0.0527	13
v_SOL_K.sol	Saturated hydraulic conductivity (mm/h)	1.909	0.0567	14
v_GW_REVAP.gw	Groundwater revap. coefficient	-1.615	0.1068	15
v_DEEPST.gw	water in the deep aquifer initial depth of (mm)	1.515	0.1302	16
v_REVAPMN.gw	Water in the shallow aquifer threshold depth of for 'revap' to occur (mm)	1.308	0.1914	17
v_CANMX.hru	Maximum canopy storage (mm)	0.497	0.6189	18

These aforementioned parameters are related to direct surface water flow and groundwater response. The least sensitive parameters included initial depth of water in the deep aquifer

(DEEPST), threshold depth of water in the shallow aquifer for 'revap' to occur (REVAPMN), and Maximum canopy storage (CANMX) (Table 4.6). They are related to deep percolation losses and maximum amount of water that can be stored in the canopy and fully developed trunks. Parameters related to channel flow (CH_N2 and CH_K2) were relatively more sensitive than parameters related to vegetation water consumption (ESCO and EPCO) and water in the soil (SOL_AWC and SOL_K) (Table 4.6). Based on the sensitivity results from SUFI-2 algorithm, there was sufficient evidence that stream flow in Njoro River catchment would majorly be influenced by soil moisture condition, duration and intensity of the storm, infiltration capacity, and groundwater recharge and discharge. Findings from other studies in Njoro River catchment (Baker & Miller, 2013; Mwetu, 2010) also pointed out that subsurface response parameters such as Specific yield of the shallow aquifer (GW_SPYLD), and Deep aquifer percolation fraction (RCHRG_DP) are the most sensitive parameters after SCS curve number for antecedent moisture condition (II) (CN2).

4.2.3 Calibration and Validation of SWAT

Uncertainty analysis, calibration, and validation for the hydrologic variables simulation was done at the 2FC05-River Gauging Station. The calibration range and fitted SWAT model parameters values are presented in Table 4.7. The calibration range as shown in the 4th column in Table 4.7 represents model output, which is an envelope of good solutions from a stochastic process expressed by the 95% prediction uncertainty. From the parameter ranges, it can be inferred that there was a smaller prediction error in the SWAT model output variables propagated by uncertainties. However, the overall uncertainty analysis results indicated an acceptable performance value of P-factor (0.72) and R-factor (0.38), which revealed that SWAT model, captured the dynamics of the catchment hydrologic response very well.

Table 4.7: Calibrated values of the Parameters

Parameter Name	Initial parameter range	Calibration range	Fitted value
v_CN2.mgt_FRST	35 - 98	58 - 64	61
v_CN2.mgt_AGRL	35 - 98	83 - 85	84
v_CN2.mgt_RNGE	35 - 98	77-79	78
r_SHALLST.gw	0 - 5000	0.25 - 2.0	0.62
v_GW_SPYLD.gw	0 - 0.4	0.001- 0.003	0.003
r_RCHRG_DP.gw	0 - 1	0.000- 0.001	0.00
v_GWQMN.gw	0 -5000	35 -70	50
r_CH_N2.rte	-0.01 - 0.3	0.0 – 0.25	0.002
v_SOL_AWC.sol	0 - 1	0.178 - 0.192	0.189
r_GW_DELAY.gw	0 - 500	-7.2 - 0.35	-6.2
v_SURLAG.bsn	0 - 24	1.5 - 2.42	1.63
r_ESCO.bsn	0 - 1	-0.003 - 0.2	-0.001
r_CH_K2.rte	-0.01 - 500	0.0 – 0.5	0.001
r_EPCO.hru	0 - 1	0.25 - 0.6	0.5
v_ALPHA_BF.gw	0 - 1	0.001 - 0.24	0.045
v_SOL_K.sol	0 - 2000	24.05 - 25.35	24.73
v_GW_REVAP.gw	0.02 - 0.2	0.57 - 1.73	0.7
v_DEEPST.gw	0 - 10000	1800 - 2200	2000
v_REVAPMN.gw	0 - 1000	150 - 350	350
v_CANMX.hru	0 - 100	14 - 21	21

The qualifier (r_) described as a parameter relative change where the initial value is multiplied by one plus a value in the given rang while (v_) refers to the substitution of a parameter by a value from the given range.

As indicated in Figure 4.25, the R^2, NSE, and PBIAS values for calibration of monthly stream flow at Flow_Out_1 were 0.88, 0.86, and 5.51 % respectively.

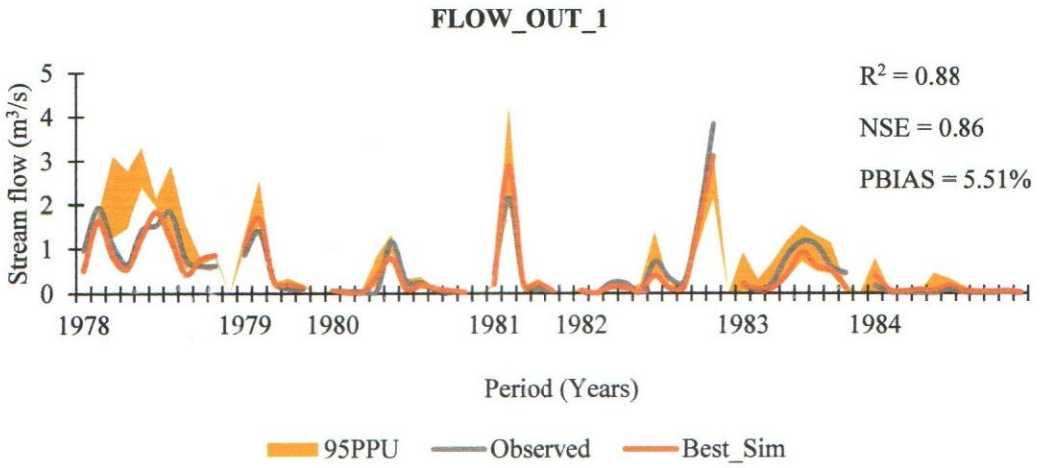

Figure 4.25: Calibration of SWAT using Stream flow data at 2FC05-RGS

As given in Figure 4.26, R^2, NSE, and PBIAS values for validation of monthly stream flow were 0.77, 0.74, and -15.42 % respectively.

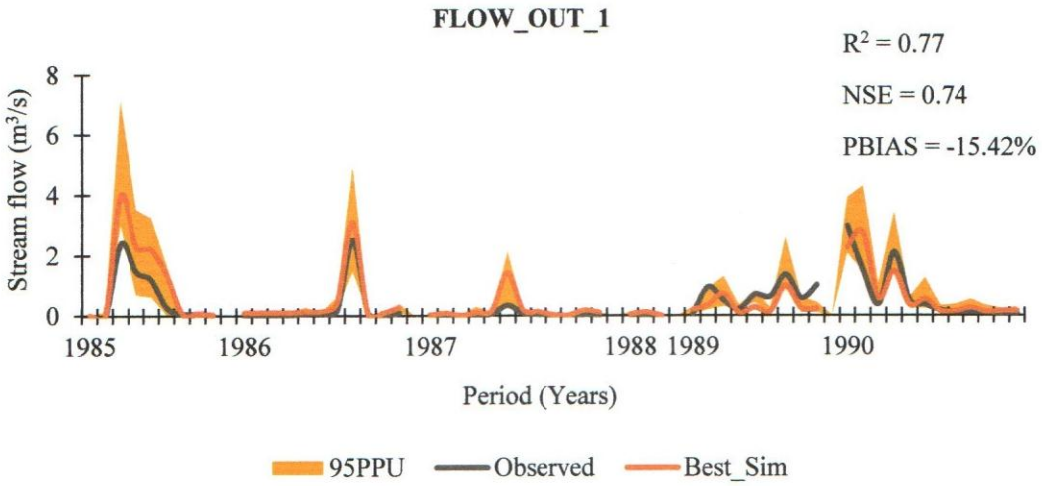

Figure 4.26: Validation of SWAT using Stream flow data at 2FC05-RGS

The calibration R^2 value of 0.88, which was a satisfactory model performance as per Abbaspour's (2007) recommendations, it was revealed that SWAT model accounted for at least 88 % of the variance of monthly flows (Figure 4.25). This implied that simulated and observed monthly stream flow had relatively similar spatial as well as temporal patterns. Since both calibration and validation values of NSE were greater than 0.5, SWAT model performance was acceptable according to Moriasi et al.'s (2007) proposed ratings (Figure 4.25 and Figure 4.26). Nevertheless, the Percentage Bias calibration and validation values indicated that there could have been a slight overestimation of monthly stream flow but this was within the limits of satisfactory model performance as supported by Van Liew et al. (2003). Hydrological

modelling by Mwetu (2010), and Baker and Miller (2013) in Njoro River catchment agrees with these SWAT model performance statistics for calibration and validation.

4.2.4 Spatial and temporal Hydrologic Components of the Stream Flow

The components of stream flow simulated spatially and temporally included surface runoff, water yield, potential, and actual evapotranspiration. Simulated monthly hydrologic variables for the period (1978 - 2017) as illustrated in Table 5A (APPENDIX A) revealed that trends of precipitation and temperature were the primary drivers of variations in water flow, circulation, and yield. It explained why dry months (DJFM) had lower actual evapotranspiration, surface runoff, and water yield than the wet months (April, May, August, and September). High amounts of water depth in the wet months were attributed to the fact that actual evapotranspiration is mainly influenced by precipitation portioning if changes in LULC are not put into consideration in a catchment.

Dry months had higher potential evapotranspiration. However, July being the month with the lowest maximum and minimum surface air temperatures, it had the lowest potential evapotranspiration. The patterns exhibited by the hydrologic variables were consistent with monthly climate variable trends as computed by Mann-Kendall's statistical analysis in the previous section. Average annual statistics revealed that for the period between 1978 and 2017, Njoro River catchment experienced 37 water stress days and 101 temperature stress days. Drier years had higher potential evapotranspiration while wetter years had higher actual evapotranspiration. Lower actual evapotranspiration in the drier years was linked to hydrologic drought due to reduced precipitation of about 24 % - 36 % anomalies. However, in wetter years where precipitation was not a limiting factor for change in evapotranspiration, the atmospheric demands and energy conditions drivers controlled by relative humidity, solar radiation, wind speed, and surface air temperatures were decisive.

For instance, the high actual evapotranspiration experienced in 1978 than in 2010 was associated with a significant decline in wind speed. As presented in Table 4.8, average annual potential and actual evapotranspiration for the 1st, 2nd, 3rd, and 4th were, 1524 and 816, 1458 and 862, 1458 and 841, and 1487 and 868 mm respectively. The balance between evapotranspiration and precipitation recharges groundwater and supports stream flow (Hamilton et al., 2018). Hence, the simulation of evapotranspiration was crucial because spatial variation of vegetation cover influences response of stream flow. Further to an extent control of evapotranspiration, precipitation remains the most dominant element of the hydrological

cycle and determines the water supply conditions in the catchment. It is the reason why on average May had the highest soil water content, lateral flow, water yield, surface runoff, and total recharge from the aquifers hence higher stream flow than any other month.

Table 4.8: Simulated Hydrologic variables on annual average basis

Simulation	Climate Data	PET (mm)	AET (mm)	SURQ (mm)	WYLD (mm)
Sim1	1978-1987	1524	816	106	163
Sim2	1988-1997	1458	862	69	114
Sim3	1998-2007	1458	841	111	170
Sim4	1998-2017	1487	868	142	261

Average surface runoff, lateral flow, groundwater return flow from the shallow aquifers, total recharge from the aquifers, and water yield for the period 1978 to 2017 was 107, 24, 45, 52, and 177mm respectively. For the 1st, 2nd, 3rd, and 4th decades, average surface runoff was 106, 69, 111, and 142 mm while the average water yield for the same decades was 163, 114, 170, and 261 mm (Table 4.8). Wetter years had high water yield and surface runoff, and this was associated with increased precipitation by 10 % - 59 % anomalies. From the spatially simulated results as given in Figure 4.27, it was noted that the actual evapotranspiration was higher in the sub-catchments where forest cover was dominant. Such sub-catchments were areas, which enclosed Njoro cave, the upper part of Nessuit, part of Mau forest, the flower farm areas, around Eastern Rift Escarpments, and Logomon.

Sub-catchments around Ahero, Njokerio, Wright, Egerton, and Beeston that were dominated by mixed agricultural, grassland, and bare land systems had lower actual evapotranspiration.

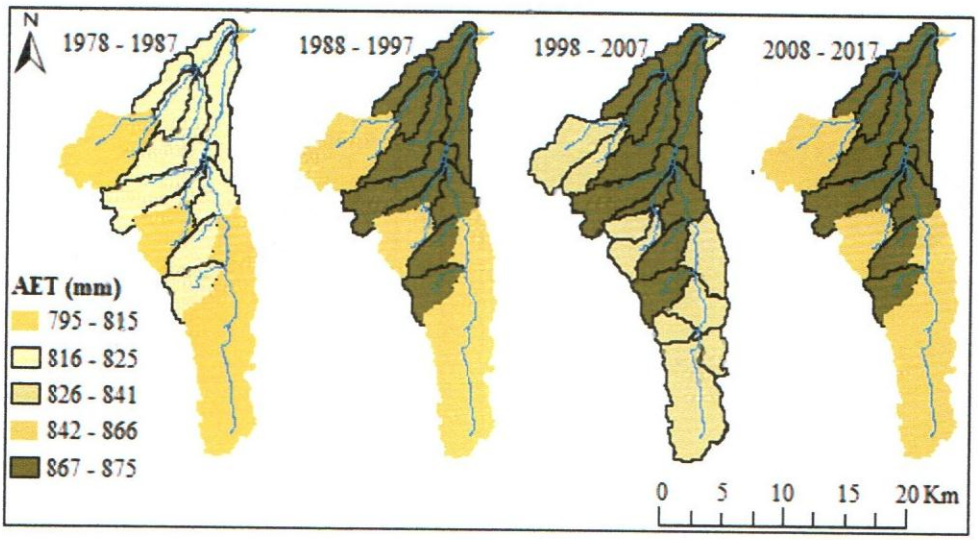

Figure 4.27: Spatio-temporal variation of actual evapotranspiration for the four decades

The lower AET values for sub-catchments under agriculture and bare land-use system was attributed to limited energy transformation in the form of sensible heat exchange because of the lower soil moisture availability (li et al., 2004). Trees exert a stronger control on the actual evapotranspiration because of their leaf area index, access, transport, and capacity to intercept. Moreover, forest canopies capturing of high advective energy under a sufficient water supply translates into higher evaporative water losses than those achieved by shorter herbaceous canopies. In the event of drought, forests may maintain higher evapotranspiration rates than any other vegetation cover because they tend to have deeper roots than herbaceous plants for trapping of groundwater. It explains why forested sub-catchments had higher available water for transpiration and evaporation more than any other LULC system. The best inference for this spatial simulation revealed that avoiding deforestation in the tropics could cool the climate through evapotranspiration.

Spatio-temporal simulations as presented in Figure 4.28 showed that the sub-catchments (1, 2, 3, 5, 6, 10, 21, and 23) around Ahero, Njokerio, Wright, Egerton, and Beeston that were dominated by mixed agricultural, grassland, and bare land systems had a higher surface runoff. Areas under forest cover had low surface runoff. High surface runoff was associated with the high values of Soil Conservation Service CN. However, sub-catchments (8 and 9) around the upper part of Nessuit bordering Mau forest, which enclosed forest as the only land-use system had a higher water yield than other sub-catchments despite having lower surface runoff (Figure 4.29).

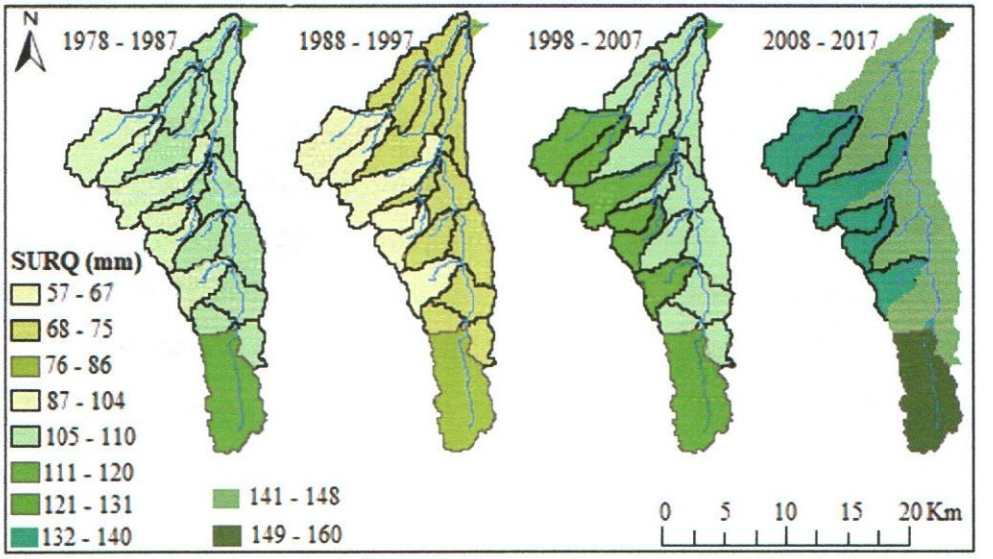

Figure 4.28: Spatio-temporal variation of surface runoff for the four decades

The sub-catchments under bare and agricultural lands excess surface runoff could be associated with the formation of soil sealing due to reduced surface cover. As pointed out by Assouline and Mualem (2000), soil sealing contributes to a significant increase in overland flow and reduced infiltration capacity due to soil compaction, pore-clogging, degradation of soil aggregates by direct rainfall impact, and slaking.

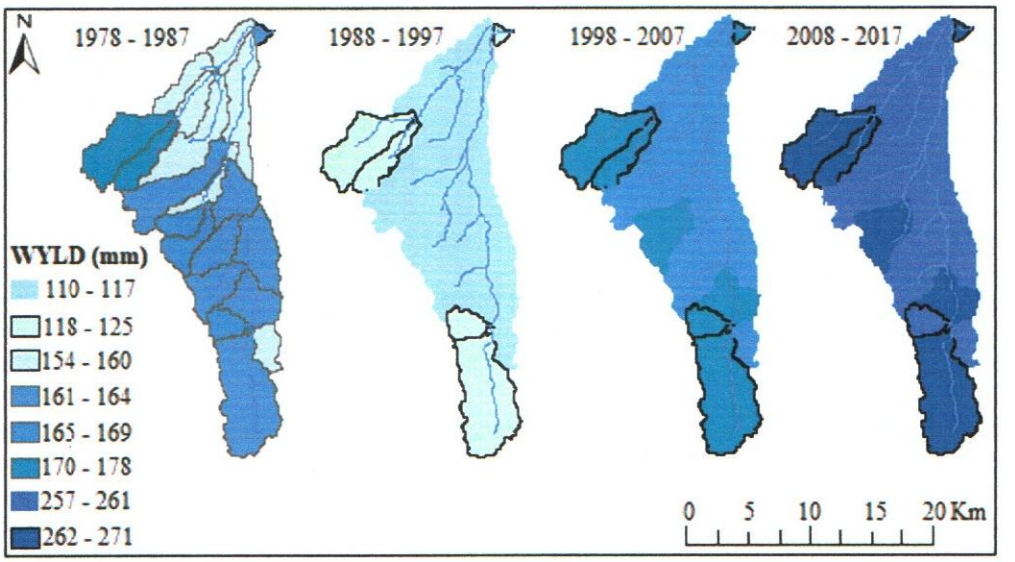

Figure 4.29: Spatio-temporal variation of water yield for the four decades

Lower water yield in Agriculture and bare land-use system than forested sub-catchments, was experienced because of lower infiltration capacity that led to reduced efficiency in storage and thus reduced recharge to channel flows. As per the Fisher and Binkley (2000) assertions, the thick Duff and O horizons underlain by deep soils in mature forests rapidly absorb water like

a sponge, and this results in delayed hydrologic response which in turn enhances frequent recharge of channel flows. Therefore, more water yield and lower surface runoff generation under forested sub-catchments could have been because of higher infiltration capacity, better soil aggregate stability, and higher hydraulic conductivity. These observations have also been reported in the Njoro River catchment by previous researchers (Amisi et al., 2018; Kundu, 2007; Mwetu, 2010). It could be inferred that planting trees, rehabilitation of the catchment, and avoiding deforestation could help in reducing the consequences of extreme hydrologic events such as floods, hydrological drought, and decline of stream flow.

4.2.5 Simulated Stream flow on Annual basis

Simulated mean annual stream flow showed a satisfactory response of peaks related to extreme occurrences of precipitation as presented in Figure 4.30.

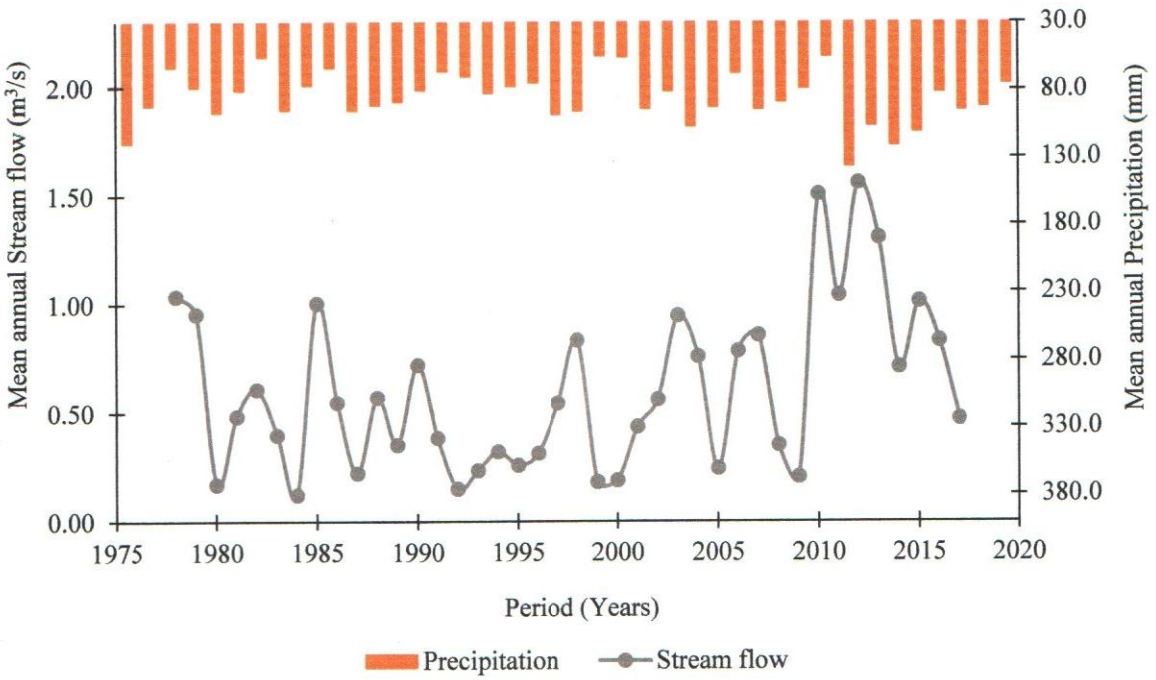

Figure 4.30: Mean annual Simulated Stream flow and Precipitation for Njoro River catchment

Stream flow satisfactory response was attributed to the fact that out of all the climate quantities precipitation dominated as an input in a catchment. For instance, it was noted that years with precipitation anomalies beyond ±24 percentage had extreme stream flow anomalies about ±57 percentage. The wet climatic conditions contributed to antecedent moisture scenarios that had the potential for high runoff and water yield generation hence increased stream flow. Mean annual minimum and maximum stream flow were 0.12 m^3/s in 1984 and 1.56 m^3/s in 2012

(Figure 4.30). Average annual stream flow for the 1st, 2nd, 3rd, and 4th decades were 0.55, 0.38, 0.58, and 0.90 m^3/s. The years 1978, 1979, 1981, 1982, 1985, 1997, 1998, 2003, 2004, 2010, and 2012 had a high stream flow, which was attributed to high surface runoff and water yield events (Figure 4.30). Lower lateral flows, soil water content, direct runoff, and return flow from groundwater sources that aggravated extreme reduction of stream flow in the years 1980, 1984, 1987, 1992, 1999, 2000, and 2009 were a result of drastic reduction of precipitation by about -36 % to -24 % of the normal annual average. These results of simulated mean annual stream flow agree with Mwetu (2010).

4.3 Spatio-temporal Effects of Climate variability on Stream Flow

Spatio-temporal impacts of climate variability on stream flow were estimated under two main analyses. The first evaluation was on spatial distribution analysis of climate variability effects on hydrological components of stream flow. Then, the second analysis was on temporal impacts of climate variability on stream flow.

4.3.1 Temporal Climate variability Effect on Hydrologic components of Stream flow

The impacts of climate variability on potential and actual evapotranspiration, surface runoff, and water yield for the four decades (1978-1987, 1988-1997, 1998-2007, and 2008-2017) are illustrated in Table 4.9.

Table 4.9: Variation of mean Hydrologic variables for the four Simulations

Hydrologic Variables Simulated using (LULC of 1978)	Climate variability Impact		
	Sim2-Sim1 (%)	Sim3-Sim1 (%)	Sim4-Sim1 (%)
Potential Evapotranspiration	-4.32	-4.33	-2.40
Actual Evapotranspiration	5.60	3.00	6.26
Surface Runoff	-34.56	4.55	34.02
Water Yield	-29.69	4.25	60.18

%(Sim2-Sim1), %(Sim3-Sim1), and %(Sim4-Sim1) = the percentage differences between the simulated hydrologic variable in the subsequent decades (2nd, 3rd, and 4th) and baseline decade.

Potential evapotranspiration under the effect of climate variability reduced by 4.32 %, 4.33%, and 2.40 % in the 2nd, 3rd, and 4th decades respectively (Table 4.9). Although temperatures had an increasing trend, the decline in potential evapotranspiration could be associated with the significant negative trends of wind speed as elaborated in Mann-Kendall trend analysis (Figure

4.19, 4.20, and 4.21). In the case of actual evapotranspiration, there was an increase of about 5.6 %, 3 %, and 6.62 % in the 2nd, 3rd, and 4th decades respectively. This was linked to the increase of more rainy years due to the gradual increase in precipitation from the baseline decade to subsequent decades. With slight changes in AET (Table 4.9), there was sufficient evidence to infer that evapotranspiration has remained to be resilient over Njoro River catchment. It further demonstrated that the influence of AET on stream flow was not significant because the depletion rate of soil moisture, subsurface water, and groundwater flows remained to be relatively constant.

The impact of climate variability contributed to a decrease in surface runoff by 34.56 % in the 2nd decade and an increase of 4.55 % and 34.02 % in the third and fourth climatic scenarios (Table 4.9). Surface runoff reduction in the second decade could have been experienced as a result of lower infiltration and percolation capacity due to higher precipitation intensity in the baseline decade. The baseline decade was characterized by large storms with short durations as compared to the 2nd decade. Increased surface runoff experienced in the 3rd and 4th decades was associated with more years with large storms than the baseline decade. The trends of surface runoff for the four decades were consistent with Mann-Kendall trend results of precipitation as illustrated in Table 4.1 and Figure 4.2. Climate variability impacts contributed to a reduction of annual water yield of 29.69 % in the 2nd decade, and an increase of 4.25 % and 60.18 % in the 3rd and 4th decades respectively (Table 4.9). Third and fourth decades relatively high increase of water yield was attributed to larger storms that led to increased groundwater flows, lateral flow, surface runoff, and soil water content. These results agreed with the findings by Baldyga (2005), Mwetu (2010), and Baker and Miller (2013).

4.3.2 Spatial Climate variability Effect on Hydrologic components of Stream flow

Analysis of Spatio-temporal distribution percentage change for actual evapotranspiration as shown in Figure 4.31 revealed that the annual actual evapotranspiration in all the sub-catchments increased under the three subsequent climatic scenarios.

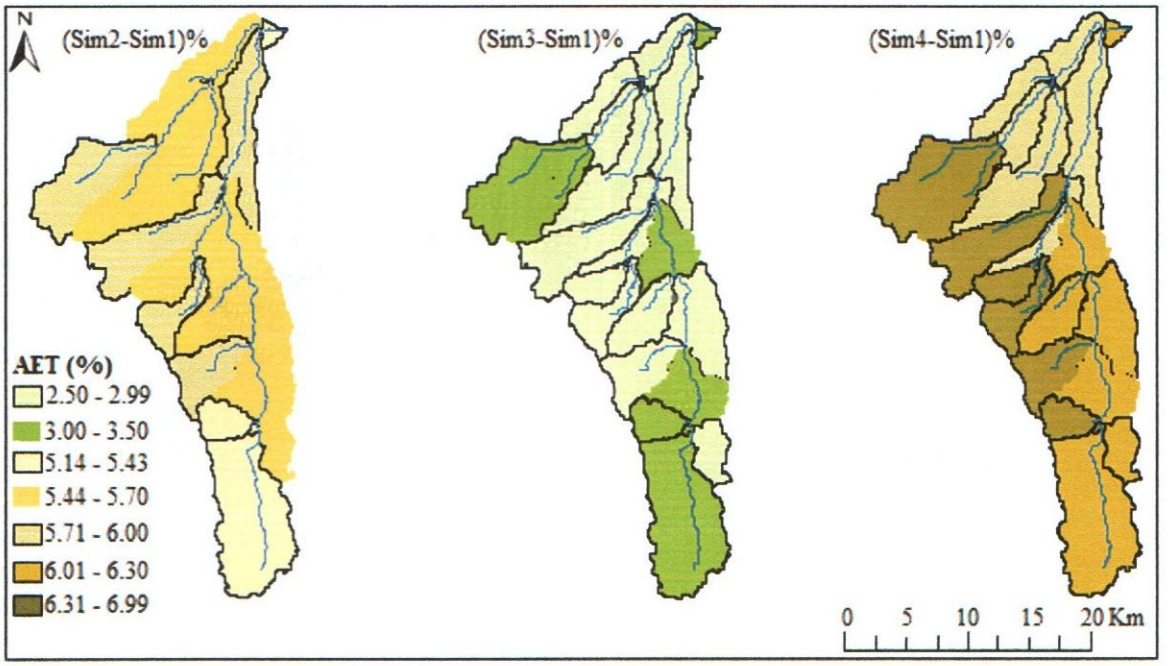

(Sim2-Sim1)%, (Sim3-Sim1)%, and (Sim4-Sim1)% = the percentage differences between the simulated Actual evapotranspiration in the subsequent decades (Sim2 = 1988 - 1997; Sim3 = 1998 – 2007; Sim4 = 2008 – 2017) and the baseline decade (Sim1 = 1978-1997).

Figure 4.31: Spatial distribution of percentage change for annual actual evapotranspiration under the effect of climate variability

Actual evapotranspiration progressive increase from the baseline decade to the subsequent decades was attributed to the positive trends of the main atmospheric demand drivers (air temperatures and vapour pressure deficit) as revealed by Mann-Kendall analyses under Figure 4.8, 4.12, 4.14, 4.16, and 4.10, and Table 4.2, 4.3, 4.4, and 4.5. The largest rate of water removal occurred in the sub-catchments under forest cover, the areas around Njoro cave, the upper part of Nessuit, part of Mau forest, the flower farm areas, around Eastern Rift Escarpments and Logomon. Precipitation partitioning variability in the catchment was evident, where more water losses showed the manifestation of soil water content, lateral flow, and groundwater for stream flow recharge in such areas. Therefore, in Njoro River catchment, recharge of stream flow that sustains River Njoro during dry seasons mainly takes place in areas dominated by forest cover where much infiltration takes place.

Analysis of the spatial distribution percentage change of annual surface runoff under the three subsequent climatic scenarios as illustrated in Figure 4.32 revealed that surface runoff reduced in the 2nd and increased in the 3rd and 4th decades for all sub-catchments.

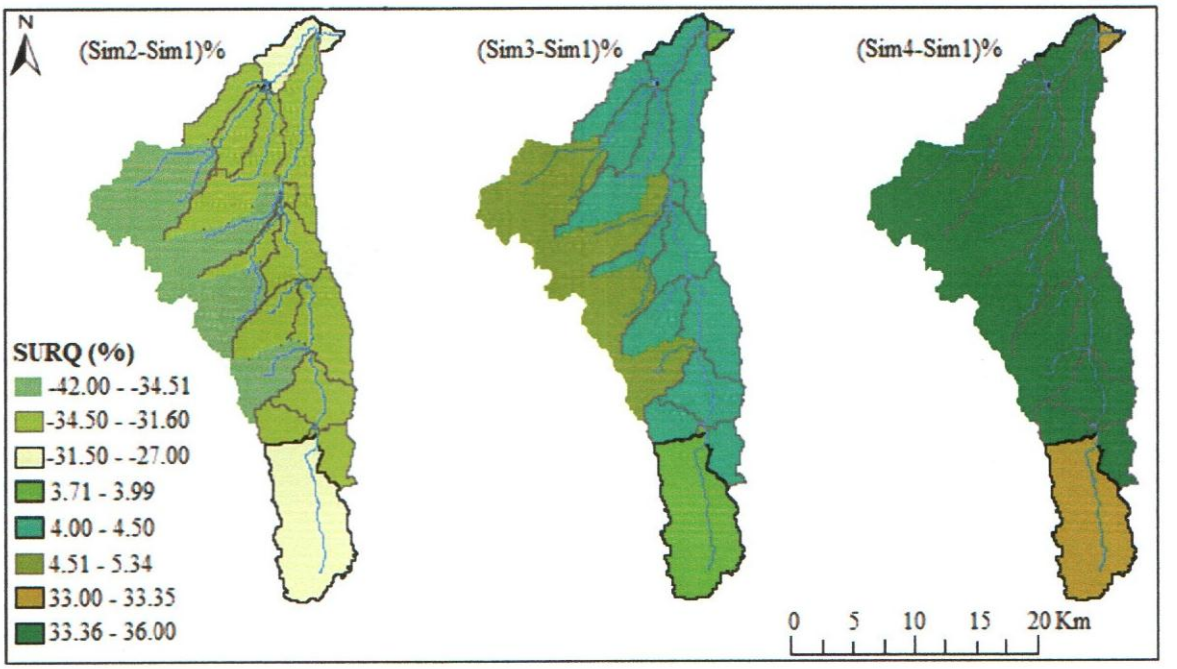

Figure 4.32: Spatial distribution of percentage change for annual surface runoff under the effect of climate variability

Surface runoff trend was consistent with the annual precipitation Mann-Kendall trend analysis results of the four decades in Table 4.1. Extreme surface runoff variability occurred in the sub-catchments (1, 2, 3, 5, 6, 10, 21, and 23) around Ahero, Njokerio, Wright, Ng'ondu, Egerton, and Beeston areas dominated by mixed agricultural, grassland, and bare land-use systems. This provided sufficient evidence of a manifestation of flush floods as the key driver of stream flow distribution in such areas. High surface runoff in the aforementioned sub-catchments implied little recharge to subsurface flows and groundwater sources because of low infiltration and percolation capacity. Also, it showed that the generation of more direct runoff during heavy storms by the areas under agricultural, settlements, and bare land-use systems in Njoro River catchment would translate to a decline in stream flow during water stress periods.

Analysis of Spatio-temporal distribution percentage change for water yield under the effect of climate variability as presented in Figure 4.33, the annual water yield in all the sub-catchments decreased in the 2nd decade, and increased in the 3rd and 4th decades.

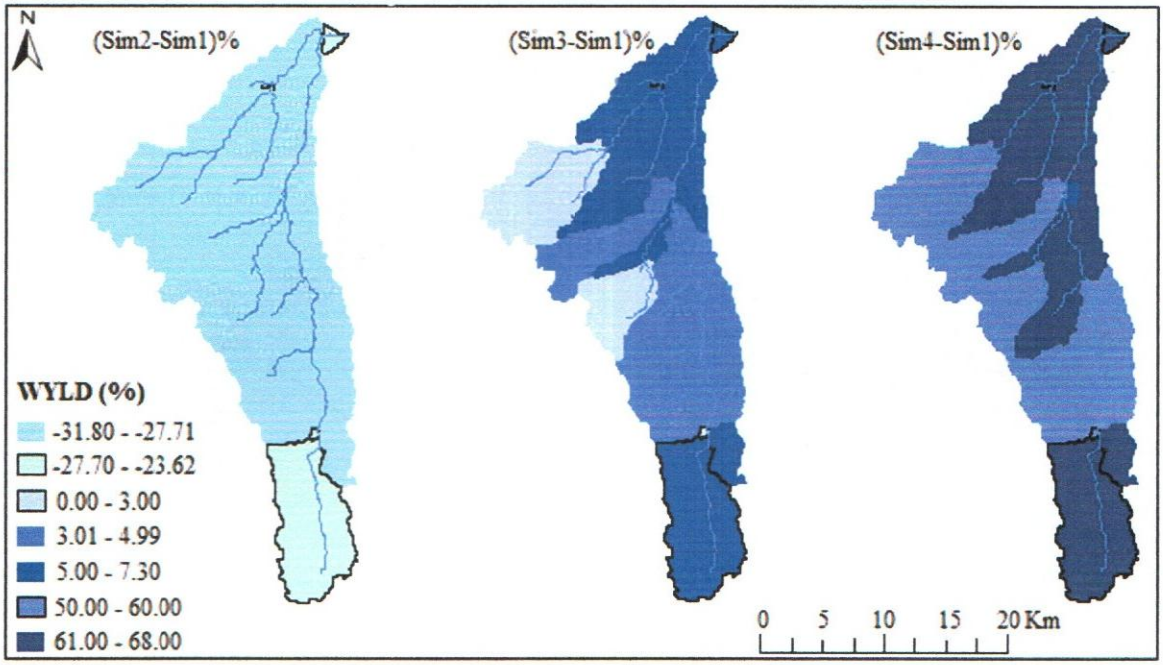

Figure 4.33: Spatial distribution of percentage change for annual water yield under the effect of climate variability

Trend exhibited by water yield was consistent with the trends of actual evapotranspiration as well as surface runoff. Water yield variability in all the sub-catchments was attributed to changes in precipitation partitioning, which included differences in percolation, actual evapotranspiration, groundwater flows, lateral flow, surface runoff, and soil water content. The results (Figure 4.33) indicated that stream flow would progressively increase in the sub-catchments under the forest LULC system because of the potential of recharge and discharge of subsurface and groundwater systems, which in effect may aid the flow of River Njoro during dry months.

4.3.3 Temporal Climate variability Effects on Stream flow

Results of climate variability impacts on annual stream flow revealed that on average, stream flow reduced by 30.91 % in the 2nd decade and increased by 5.47 % and 63.63 % in the third and fourth decades respectively (Figure 4.34).

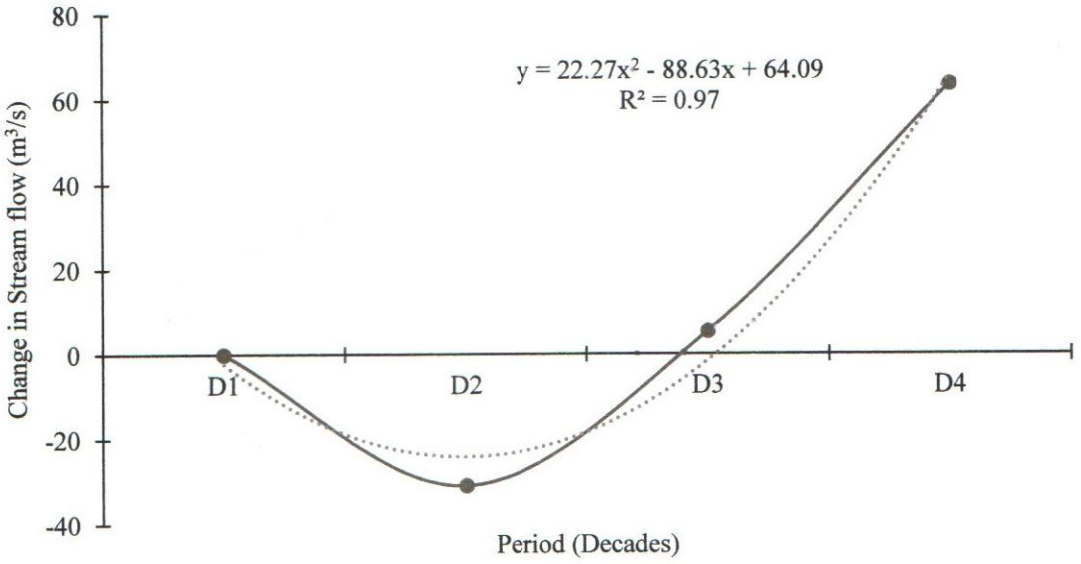

D1, D2, D3, and D4 = 1st (1978-1987), 2nd (1988-1997), 3rd (1998-2007), and 4th (2008-2017) decades respectively.

Figure 4.34: Annual change of Stream flow for the four decades at Njoro River Catchment.

Stream flow reduction in the 2nd decade was associated with the decrease of water yield as well as surface runoff due to the variations in precipitation intensities and duration and increased actual evapotranspiration. Additionally, the groundwater recharge declined consequently, leading to the low water yield in the various sub-catchments in the second decade. However, the increase of stream flow in the 3rd and 4th climatic scenarios was associated with an increase in recharge and discharge of groundwater, subsurface flows, infiltration capacity, and surface runoff leading to increased water yield in all sub-catchments. From the results in Figure 4.34, it was evident that the impact of LULC changes could be the key factor for the extreme decline in stream flow that has been witnessed in the recent past in Njoro River catchment. This was so because the effect of climate variability revealed a possibility of an increase in stream flow by over 63 %. These observations have also been pointed out by other studies (Kundu, 2007; Mwetu, 2010) in Njoro River Catchment.

4.4 Forecasted Climate variability Impact on Stream Flow

ANN models were used for forecasting of mean monthly temperature and precipitation and mean annual stream flow for the period (2018 - 2037). Nonlinear autoregressive neural networks were applied for forecasting precipitation and air temperature while the forecasted impact of climate variability on stream flow was computed based on the mean annual stream

flow predicted by Feedforward backpropagation neural networks for the two decades (2018-2027 and 2028-2037).

4.4.1 ANN Models Performance for Precipitation and Temperature Forecasting

The performance of various nonlinear autoregressive neural network models in the forecasting of precipitation and temperature varied monthly as illustrated in Table 4.10.

Table 4.10: Best ANNs for forecasting of Mean Monthly Precipitation and Temperature

	Mean monthly Precipitation				Mean monthly Air Temperature			
Month	Network Architecture	R^2	RMSE	MBE	Network Architecture	R^2	RMSE	MBE
Jan	1-25-1	0.69	1.58	0.80	1-25-1	0.86	0.45	0.07
Feb	1-20-1	0.72	0.87	0.33	1-10-1	0.83	0.67	0.12
Mar	1-20-1	0.69	1.59	0.70	1-20-1	0.86	0.42	-0.01
Apr	1-25-1	0.70	1.11	-0.41	1-30-1	0.72	0.88	0.19
May	1-20-1	0.77	0.72	0.44	1-25-1	0.75	0.75	0.03
Jun	1-25-1	0.77	0.77	0.46	1-20-1	0.86	0.42	-0.05
Jul	1-25-1	0.71	0.99	0.52	1-20-1	0.87	0.56	0.02
Aug	1-30-1	0.69	1.68	0.70	1-25-1	0.77	0.74	0.03
Sep	1-30-1	0.66	1.05	-0.67	1-20-1	0.72	0.78	0.01
Oct	1-20-1	0.70	1.61	0.70	1-10-1	0.81	0.64	0.06
Nov	1-30-1	0.73	0.86	-0.53	1-25-1	0.78	0.82	-0.01
Dec	1-20-1	0.72	0.89	0.32	1-20-1	0.83	0.48	-0.07

1-25-1 = an architecture showing that ANN model consisted of one input vector (for example, historical precipitation data), and one hidden layer having 25 neurons to forecast a single output (precipitation in future).

From the results, the highest and lowest values of R^2 (0.77 and 0.66), RMSE (1.68 and 0.72 mm), and MBE (0.32 and 70 mm) in columns 3, 4, and 5 showed that the models captured temporal mean monthly precipitation patterns at a very good level (Table 4.10). The R^2 values indicated that the forecasting models elucidated at least 66 % of the variance of precipitation values monthly. Additionally, the lowest values of RMSE (0.72 mm) and MBE (0.32 mm) portrayed a better fit between the forecasted and measured mean monthly precipitation. Nonetheless, there could have been a slight underestimation of mean monthly precipitation in

April, September, and November. The statistical indicators of best ANN for forecasting precipitation revealed a better model performance as per Nastos et al. (2014) recommendations. As presented in Table 4.10, the highest and lowest values of R^2 (0.86 and 0.72), RMSE (0.88 ^{0}C and 0.42 ^{0}C), and MBE (0.19 ^{0}C and -0.01 ^{0}C) in columns 7, 8, and 9 revealed that ANN models captured monthly temperature patterns at a satisfactory level. It was inferred that the forecasting models were capable of explaining at least 72 % of the variance of mean monthly temperature values. Besides, R^2 values for January, March, and July indicated high prediction accuracy and a relatively perfect linear covariation between the predicted and measured air temperature values. Statistically, the models performed so well in air temperature forecasting as per Fernandez et al. (2005) rating criteria.

4.4.2 Precipitation Forecasts

As given in Figure 4.35, there is a likelihood positive trend in precipitation at Njoro River catchment for the period (2018 – 2037). The highest annual precipitation forecasted was 1601 mm in the year 2030 and the lowest projected was 780 mm in 2024.

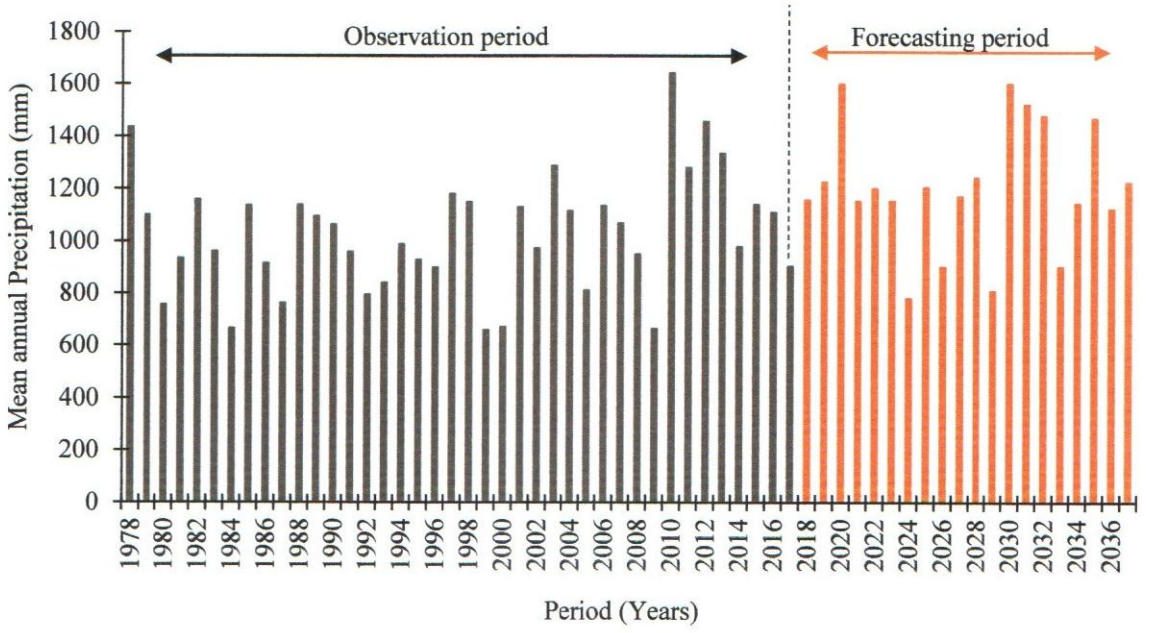

Figure 4.35: Observed and Forecasted mean annual Precipitation for Njoro River Catchment

ANN models forecasting showed that dry months (December, January, February, and March) are likely to become relatively drier. It contradicted some studies on PRECIS regional climate modelling in East Africa, for instance, Rwigi (2014) a study carried out at one of the Mau blocks (Sondu region). Perhaps, because the aforementioned study used the worst-case situation of business as usual with no envisioned changes in policy (SRES A2), which had not

Forecasted progressive positive trends of precipitation would likely continue following a polynomial trend curve of the third order. The positive trend of decadal precipitation changes was significant at $p < 0.01$, and over 95 % of the 60-year average annual rainfall variability may be described by time as the independent variable (Figure 4.36). Similar trends of likely precipitation positive trends in future climatic scenarios for East Africa region have also been reported by other studies on regional climate modelling such as Githui et al. (2009), Shongwe et al. (2011), Anyah and Qiu (2012), Rwigi et al. (2016), and Ongoma et al. (2018). There was sufficient evidence to infer that the climate around Njoro River catchment continues to become wetter. This implied that surface runoff, lateral flow, recharge of groundwater sources, and soil water content may increase significantly in the future climatic scenarios (2018-2037), hence positive trends in stream flow.

4.4.3 Surface Air Temperature Forecasts

Temperature will progressively increase in the periods (2018-2027 and 2028-2037) in all the months with a range of 1.1^{0}C to 2.5 ^{0}C, and henceforth, the air temperatures will be higher than baseline temperature by 0.5 ^{0}C to 2.5 ^{0}C in the future subsequent decades. Mean annual observed and forecasted air temperature as presented in Figure 4.37, showed a positive trend into the future climatic scenarios.

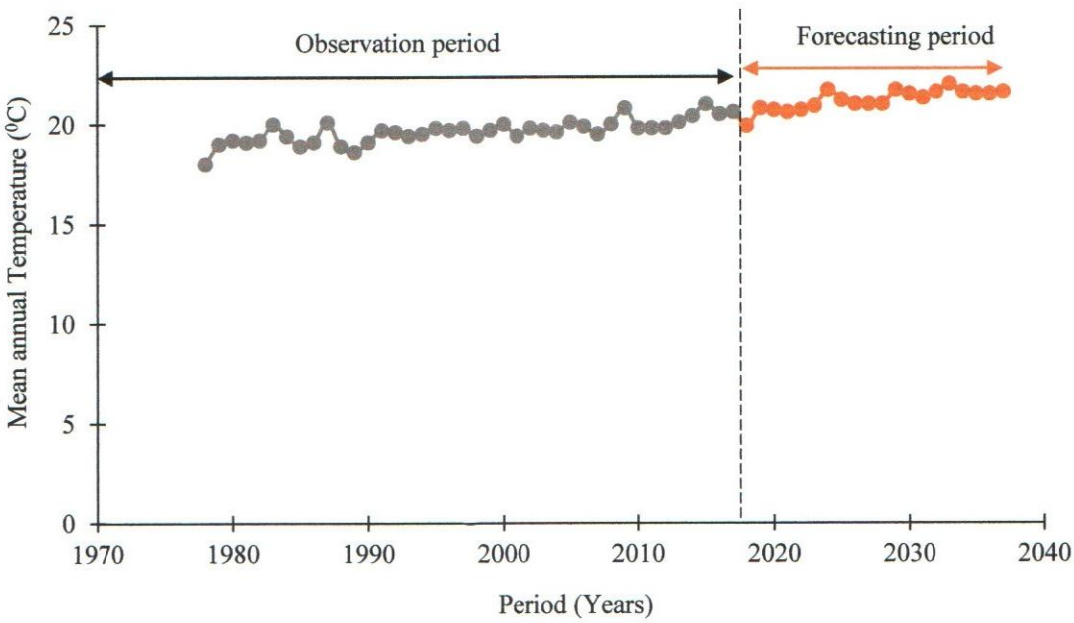

Figure 4.37: Time series of Observed and Forecasted mean annual air Temperature

The surface air temperature rise was forecasted to continue between the period 2018 and 2037 following a polynomial trend curve of the fourth order, and this corresponds to what has been

reported in recent years from regional climate modelling studies like Githui (2008) and Rwigi (2014). Moreover, these findings agree with regional as well as worldwide observations where anomalies are also largely beyond the baseline values after the mid-1980s. Forecasting further revealed that surface air temperature will largely be above the 2018 value with the highest temperature of 22 ^{0}C in 2033. Annual average air temperatures were forecasted to change by about 1.8°C and 2.4 °C by 2027 and 2037 respectively relative to the baseline decade (Figure 4.38).

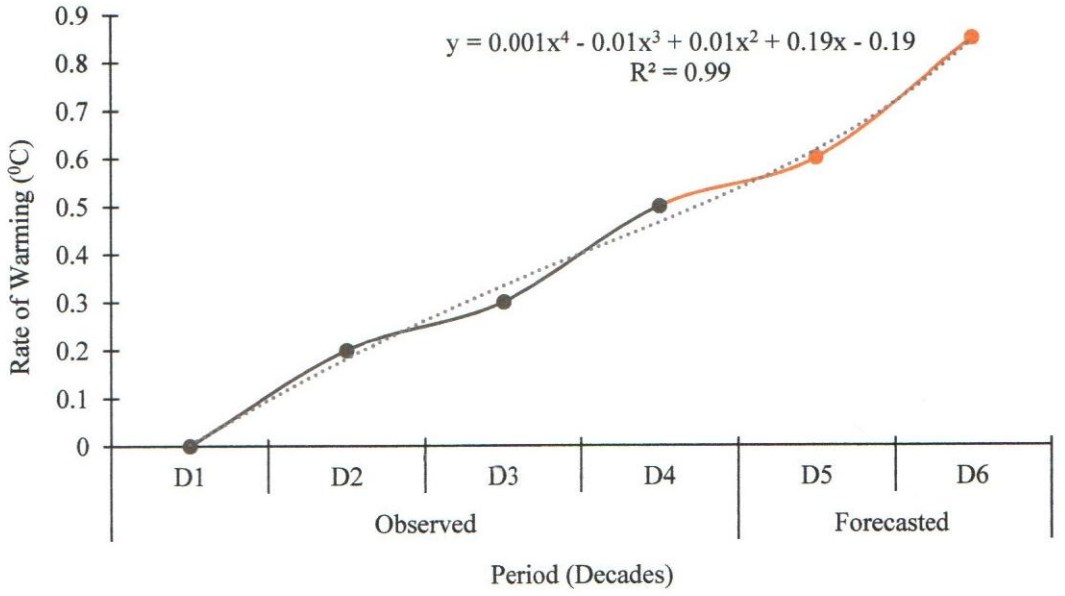

D1, D2, D3, D4, D5, and D6 = 1st (1978-1987), 2nd (1988-1997), 3rd (1998-2007), 4th (2008-2017), 5th (2018-2027), and 6th (2028-2037) decades respectively

Figure 4.38: Observed and forecasted rates of warming for Njoro River Catchment

The upward trend of decadal temperature changes was significant at $p < 0.01$, and over 99 % of the 60-year mean annual temperature variability could be explained by the independent variable (time) (Figure 4.38). From the baseline decade (D1), the rate of warming increased by 0.6 ^{0}C, and 0.85^{0}C in the 5th (2018-2027), and 6th (2027-2037) decades respectively. There was sufficient evidence to infer that climate around Njoro River catchment had become warmer with time. Where, the extreme air temperatures in the area could be experienced in the most recent and future decades (the 2020s, 2030s, and 2040s). An increasing rate of warming over Njoro River catchment was in line with the global observations as evident in the special report by IPCC (2007). There are more agreements between different climate modelling techniques over future positive trends in mean annual temperatures in nearly all the RCMs studies

(Omondi et al., 2014; Ongoma et al., 2018; Mbote, 2016). The progressive future rise in temperature would likely be linked to both negative and positive variations in radiation balance, which in effect will affect the supply of energy to provide latent heat of vaporization. Therefore, the forecasted annual air temperature indicated a likelihood of an increase of antecedent soil water content and plant biomass depletion rates.

4.4.4 Best ANN for Forecasting of Stream flow Performance Indicators

Based on the results as shown in Figure 4.39, the best forecasting performance was accomplished when the number of nodes in the hidden layer was 30. However, in all the trials, forecasting efficiency was also relatively better when neurons in the hidden layer ranged from 20 to 30.

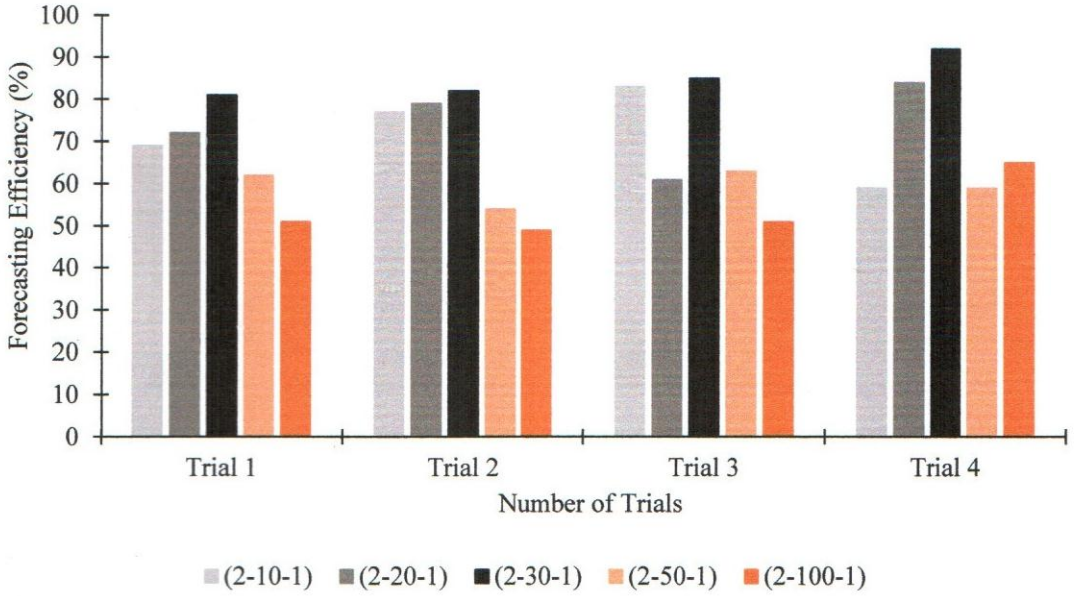

2-10-1 = this is an architecture showing that ANN model consisted of two input vectors (temperature and precipitation data), and one hidden layer having 10 neurons to forecast a single output (stream flow).

Figure 4.39: Forecasting performance Efficiency of ANNs with different neurons

As shown in Figure 4.40, correlation coefficient (R-values) of 0.95, 0.92, and 0.85 for training, validation, and testing respectively was achieved for the optimum ANN for stream flow forecasting. The correlation coefficient was necessary for the assessment of the model prediction ability. From the validation graph, the dashed line represented a perfect fit curve where observed data supplied as target dataset for training and testing were equal to forecasted data, and the coloured solid line represented the best fit between outputs and target values. The

R-value of 0.95 implied that the best ANN model for forecasting was capable of accounting for at least 95 % of the input variable, hence, a satisfactory result from 1000 iterations (Figure 4.40).

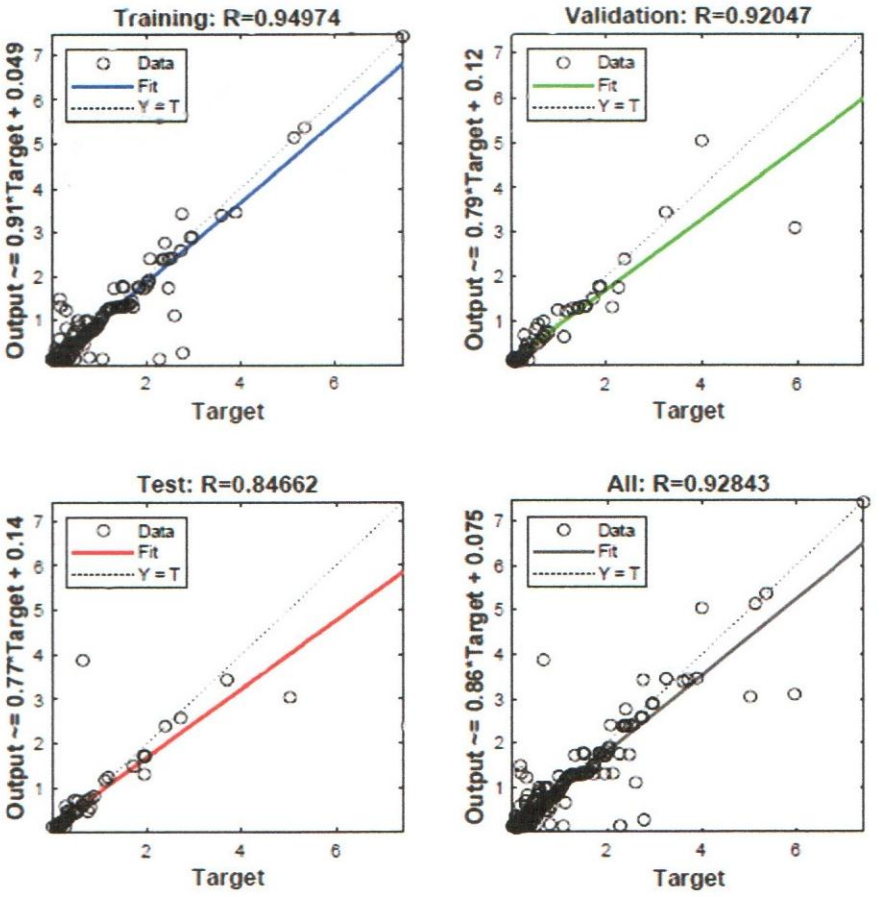

Figure 4.40: Regression of the best ANN for Stream flow forecasting

Further, Figure 4.41 portrayed the training, validation, and testing MSE values for the Levenberg-Marquardt algorithm with 2-30-1 model topology.

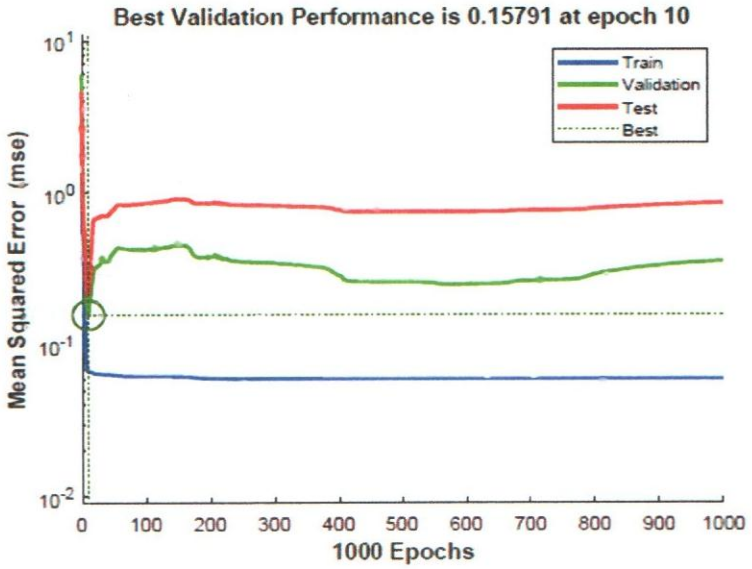

Figure 4.41: L-M algorithm MSE results for Stream flow forecasting

In this scenario of the best ANN model for stream flow forecasting, the minimum MSE values for training, validation, and testing were 0.94, 0.93, and 0.85 respectively. The best validation performance was 0.15791 at epoch 10. Predicted stream flow by best ANN model for two years with high and lower precipitation from every decade comparison with the simulated stream flow by SWAT (Figure 4.42) revealed that the R^2 and NSE were achieved at 0.92 and 0.89 respectively.

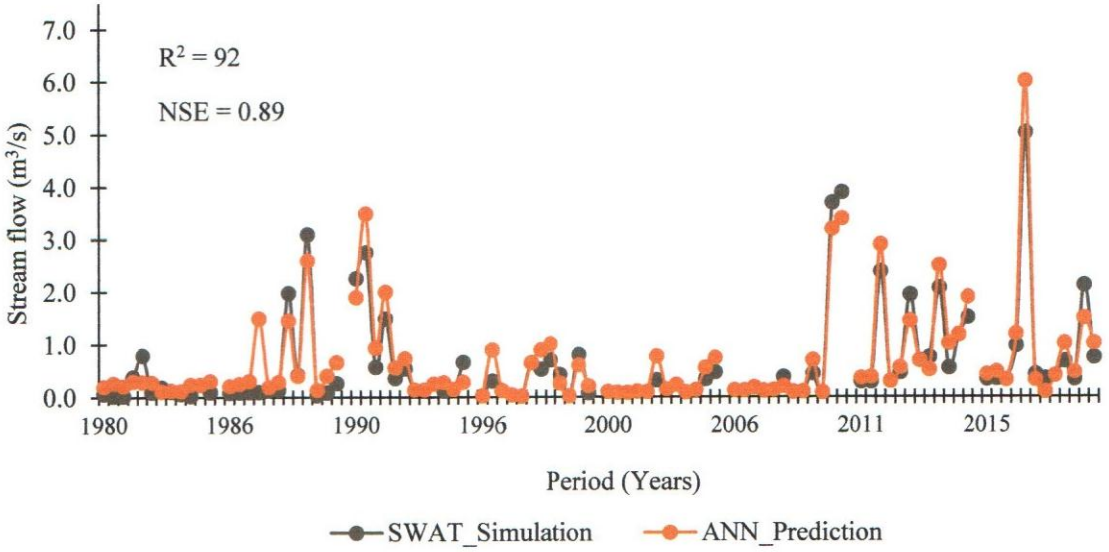

Figure 4.42: SWAT simulated Stream flow and ANN's best forecasts

The R^2 of 0.92 implied that the ANN forecasting model used was able to explain 92 % variance of stream flow monthly. From the results (Figure 4.42), the R^2 value revealed that SWAT

simulated stream flow and ANN predicted dataset had similar temporal patterns. A relatively perfect match between the SWAT and ANN outputs was realized as confirmed by the high value of Nash–Sutcliffe efficiency. The overall performance rating of the artificial neural network model was very good according to Fernandez et al. (2005) and Moriasi et al. (2007) analyses criteria.

4.4.5 Forecasted temporal Climate variability Effects on Stream flow

The time series of SWAT simulated and ANN forecasted stream flow under the effects of climate variability results for Njoro River catchment is presented in Figure 4.43. Annual stream flow in the 2020s and 2030s is likely to increase progressively as it would be supported by the precipitation positive trends for the period (2018-2037). As forecasted, the lowest mean annual flow (0.24 m^3/s) may be experienced in 2029 and the highest 1.90 m^3/s in 2030 (Figure 4.43).

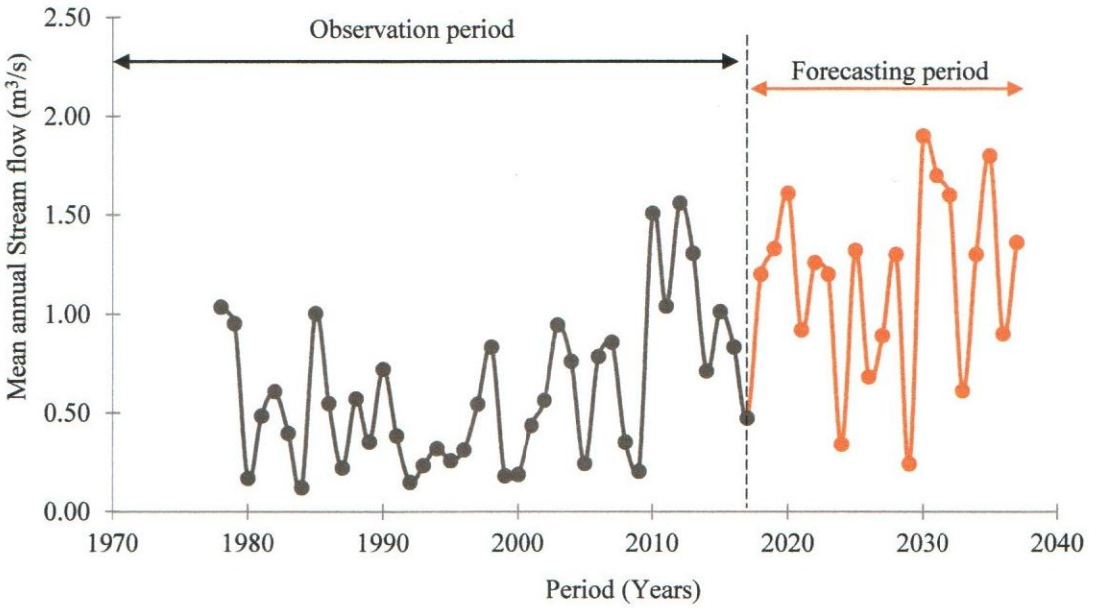

Figure 4.43: Time series of Simulated and Forecasted mean annual Stream flow

Results of the forecasted impact of climate variability as presented in Figure 4.44 indicated that on average annually, River Njoro catchment would likely experience an increase in stream flow by about 83.05 % and 130.12 % in the 5th and 6th decades respectively. R^2 of 0.99 implied that 99 % stream flow variations under climate variability alone were accounted for by the independent (time) variable. The increasing trend was forecasted to continue in polynomial trend curve configuration of the fourth order, and this corresponds to what has been reported in recent years from regional climate modelling impact studies like Rwigi (2014).

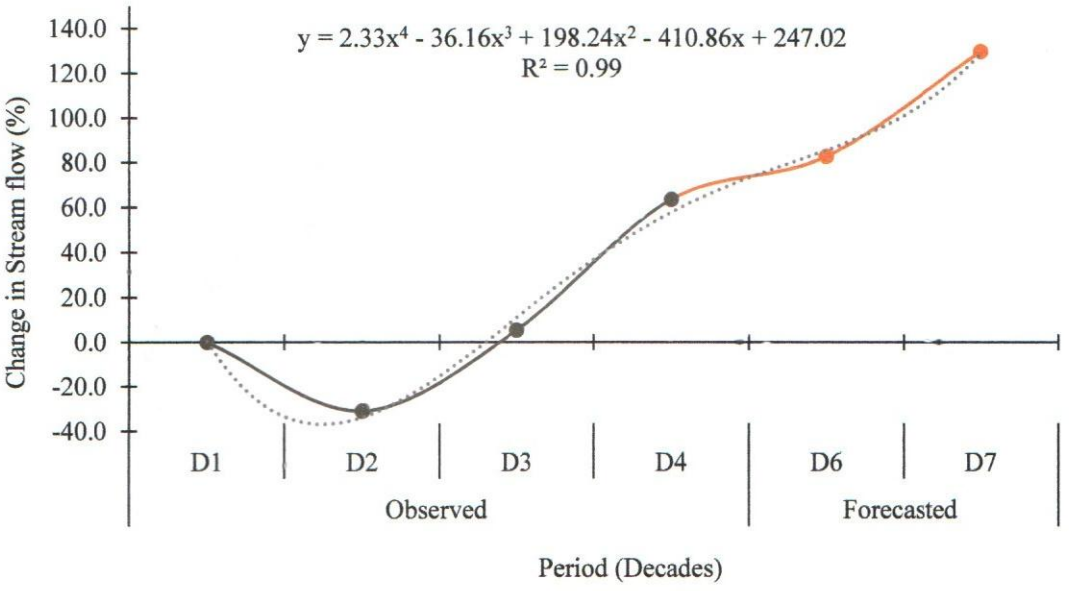

D1, D2, D3, D4, D5, and D6 = 1st (1978-1987), 2nd (1988-1997), 3rd (1998-2007), 4th (2008-2017), 5th (2018-2027), and 6th (2028-2037) decades respectively.

Figure 4.44: Time series of Simulated and Forecasted percentage change of Stream flow for Njoro River Catchment

Forecasted stream flow trend compared so well with decadal precipitation changes, and this implied that variability in forecasted stream flow could be explained by the variability in precipitation. Since LULC was assumed constant for the entire period, changes in forecasted stream flow were associated with variations of hydrologic response of the catchment due to climate variability. Forecasted stream flow results agreed with other climate variability and change impact studies from other catchments neighbouring and around Njoro River catchment such as Githui et al. (2009) in Nzoia, Rwigi (2014) in Sondu, Mwangi et al. (2016) in upper Mara River, and Mbote (2016) around Lake Nakuru. The aforementioned climate impact studies also project an increase in water yield as well as stream flow in future climatic scenarios due to projections that precipitation will increase. It was inferred that even in the future climatic scenarios, the impact of socio-economic activities at the Njoro River catchment would remain to be the dominant factor for the extreme decline of stream flow. Statistical evidence of the changing climate at Njoro River catchment points out that though there is a likelihood of surface runoff, subsurface flows, and groundwater flows progressive increase in the future, all these effects of climate variability may not override the impact of LULC changes on stream flow.

CHAPTER FIVE

CONCLUSIONS AND RECOMMENDATIONS

5.1 Conclusions

This research modelled and forecasted the spatial and temporal impacts of climate variability on stream flow in the Njoro River catchment, Kenya. The following are specific conclusions drawn from the findings;

Trends of climate variables from the period between 1978 and 2017 effectively revealed that the Njoro River catchment has been under the influence of climate variability. From the Mann-Kendall trend analyses, annual precipitation had a positive trend that was not significant at $p < 0.05$. Monthly precipitation patterns indicated a shifting tendency where precipitation peaks shifted from April to May and from August to September. Over the same period, the mean annual temperature changed by 3 ^{0}C. Solar radiation, maximum and minimum temperatures had significant positive trends at $p < 0.05$. Relative humidity had a negative trend that was not significant. Wind speed had a significant decreasing trend.

Based on modelling of stream flow response using SWAT, SUFI-2 algorithm results indicated that the most sensitive parameter in Njoro River catchment was SCS curve number for antecedent moisture condition (II) (CN2), ranked according to the highest sensitivity tested at $p < 0.05$. The least sensitive parameter was Maximum canopy storage (CANMX). Overall uncertainty analysis results showed a good performance value of P-factor (0.72) and R-factor (0.38), which revealed that SWAT captured the dynamics of the catchment hydrologic response fairly well. The values of R^2, NSE, and PBIAS for calibration and validation of monthly stream flow were 0.88 and 0.77, 0.86 and 0.74, and 5.51 % and -15.42 % respectively.

From the spatio-temporal impacts of climate variability on hydrologic variables, actual evapotranspiration increased by about 5.6 %, 3 %, and 6.62 % in the 2nd, 3rd, and 4th decades. Surface runoff decreased in the 2nd decade by 34.56 % and increased by 4.55 % and 34.02 % in the 3rd and 4th decades. Annual water yield decreased in the 2nd decade by 29.69 % and increased by 4.25 % and 60.18 % in the 3rd and 4th decades respectively. As a result of changes in the aforementioned hydrologic variables, it was inferred that on average, stream flow reduced by 30.91 % in the 2nd decade and increased by 5.47 % and 63.63 % in the 3rd and 4th decades respectively.

R^2, RMSE, and MBE values for the best nonlinear autoregressive neural network used for precipitation and temperature forecasting were 0.77, 0.77, and 0.46 and 0.87, 0.56, and 0.02, which was a satisfactory performance. The performance revealed that NAR model could be used as an alternative forecasting technique. Annual average temperature and precipitation were forecasted to increase from the baseline values by about 0.6 ^{0}C and 18.99 % respectively for the period 2018 to 2027, and by 0.85 ^{0}C and 28.26 % respectively for the period (2028 - 2037). SWAT_ANN modelling approach indicated an overall better performance for stream flow forecasting, and R^2 and NSE values were 0.92 and 0.89. The average annual stream flow was forecasted to increase from the baseline values by about 83 % and 130 % for the periods (2018 – 2027) and (2028 – 2037) respectively.

5.2 Recommendations

The following recommendations were made for future research work;

i. Assessment of effects of time-series datasets of serial correlation, identify the shifts in the climate variables and quantify the magnitude of the shifts in the variables using new techniques such as the Innovative Trend Analysis (ITA) method, and Theil-Sen approach (TSA).

ii. SWAT model should be used with data from many weather and river gauging stations to further establish the effect of spatial variability of precipitation. It may help to establish why the lower part of the Njoro River catchment appears to be drier than the upper part of the catchment.

iii. Input uncertainty analysis-to assess the sensitivity of various input data including remote sensing data on SWAT outputs to optimize the most suitable data; hydro-meteorological analysis- to evaluate the variability of extreme events, which is of utmost importance to drought and flood management.

iv. Hydrological modelling by coupling SWAT and ANN for predicting hydrologic variables in future climatic scenarios in other catchments. It should be explored further by the use of artificial intelligence, computer-based approaches, and more machine learning techniques.

REFERENCES

Abbaspour, K. C., Vejdani, M., Haghighat, S., & Yang, J. (2007, December). SWAT-CUP calibration and uncertainty programs for SWAT. In *MODSIM 2007 international congress on modelling and simulation. modelling and simulation society of Australia and New Zealand* (pp. 1596-1602).

Abbaspour, K. C., Rouholahnejad, E., Vaghefi, S. R. I. N. I. V. A. S. A. N. B., Srinivasan, R., Yang, H., & Kløve, B. (2015). A continental-scale hydrology and water quality model for Europe: Calibration and uncertainty of a high-resolution large-scale SWAT model. *Journal of Hydrology*, 524, 733-752.

Adamowski, J. F. (2008). Development of a short-term river flood forecasting method for snowmelt driven floods based on wavelet and cross-wavelet analysis. *Journal of Hydrology*, 353(3-4), 247-266.

Alabi, R. O. (2017). Prediction of recurrence and mortality of oral tongue cancer using artificial neural network (A case study of 5 hospitals in Finland and 1 hospital from Sao Paulo, Brazil).

Allen, M. R., Barros, V. R., Broome, J., Cramer, W., Christ, R., Church, J. A., & Edenhofer, O. (2014). IPCC Fifth Assessment Synthesis Report-Climate Change. *Synthesis Report*.

Alwakeel, M., & Shaaban, Z. (2010). Face recognition based on Haar wavelet transform and principal component analysis via Levenberg-Marquardt backpropagation neural network. *European Journal of Scientific Research*, 42(1), 25-31.

Arnell, N. W. & Delaney, E. K. (2006). Adapting to climate change: public water supply in England and Wales. *Climatic Change*, 78(2-4), 227-255.

Arnold, J. G., Moriasi, D. N., Gassman, P. W., Abbaspour, K. C., White, M. J., Srinivasan, R., ... & Jha, M. K. (2012). SWAT: Model use, calibration, and validation. *Transactions of the ASABE*, *55*(4), 1491-1508.

Arnold, J. G., Srinivasan, R., Muttiah, R. S. & Williams, J. R. (1998). Large area hydrologic modeling and assessment part I: model development 1. *JAWRA Journal of the American Water Resources Association*, 34(1), 73-89.

Asfaw, A., Simane, B., Hassen, A., & Bantider, A. (2018). Variability and time series trend analysis of rainfall and temperature in northcentral Ethiopia: A case study in Woleka sub-basin. *Weather and Climate Extremes*, 19, 29-41.

Azadi, M. & Zakeri, Z. (2010). Probabilistic precipitation forecasting using a deterministic model output over Iran. *Research Journal of Environmental Sciences*, 4(2), 138-I48.

Baldyga, T. J. (2005). *Assessing land cover change impacts in Kenya's River Njoro watershed using remote sensing and hydrologic modeling* (Doctoral dissertation, University of Wyoming). ProQuest Dissertations and Theses Global.

Baker, T. J., & Miller, S. N. (2013). Using the Soil and Water Assessment Tool (SWAT) to assess land use impact on water resources in an East African watershed. *Journal of Hydrology*, (486), 100-111.

Bao, Z., Zhang, J., Wang, G., Fu, G., He, R., Yan, X., & Zhang, A. (2012). Attribution for decreasing streamflow of the Haihe River basin, northern China: climate variability or human activities. *Journal of Hydrology*, (460), 117-129.

Bao, Z., Zhang, J., Liu, J., Fu, G., Wang, G., He, R., & Liu, H. (2012). Comparison of regionalization approaches based on regression and similarity for predictions in ungauged catchment s under multiple hydro-climatic conditions. *Journal of Hydrology*, 466: 37-46.

Benmouiza, K., & Cheknane, A. (2013). Forecasting hourly global solar radiation using hybrid k-means and nonlinear autoregressive neural network models. *Energy Conversion and Management*, 75: 561-569.

Benmouiza, K., & Cheknane, A. (2016). Small-scale solar radiation forecasting using ARMA and nonlinear autoregressive neural network models. *Theoretical and Applied Climatology*, 124(3-4), 945-958.

Benson, D., Gain, A. K., & Rouillard, J. J. (2015). Water governance in a comparative perspective: From IWRM to a'nexus' approach. *Water Alternatives*, 8(1), 756-773.

Beven*, K. (2001). How far can we go in distributed hydrological modelling?. *Hydrology and Earth System Sciences*, 5(1), 1-12.

Booij, M. J., Schipper, T. C., & Marhaento, H. (2019). Attributing Changes in Stream flow to Land Use and Climate Change for 472 Catchment s in Australia and the United States. *Water*, 11(5), 1059.

Borah, D. K., & Bera, M. (2003). Watershed-scale hydrologic and nonpoint-source pollution models: Review of mathematical bases. *Transactions of the ASAE*, 46(6), 1553.

Borah, D. K., & M. Bera. (2004). Watershed-scale hydrologic and nonpoint-source pollution models: Review of applications. *Transactions of the ASAE*, 47(3): 789-803.

Brown, C., & Lall, U. (2006, November). Water and economic development: The role of variability and a framework for resilience. In *Natural resources forum* (Vol. 30, No. 4, pp. 306-317). Oxford, UK: Blackwell Publishing Ltd.

Camberlin, P. (2018). Climate of eastern Africa. In *Oxford Research Encyclopedia of Climate Science*.

Charlton, M. B., & Arnell, N. W. (2011). Adapting to climate change impacts on water resources in England—an assessment of draft water resources management plans. *Global Environmental Change*, 21(1), 238-248.

Che, Z. G., Chiang, T. A., & Che, Z. H. (2011). Feed-forward neural networks training: a comparison between genetic algorithm and back-propagation learning algorithm. *International Journal of Innovative Computing Information and Control*, 7(10), 5839-5850.

Chien, H., Yeh, P. J. F., & Knouft, J. H. (2013). Modeling the potential impacts of climate change on stream flow in agricultural watersheds of the Midwestern United States. *Journal of Hydrology*, 491: 73-88.

Cibin, R., Sudheer, K. P., & Chaubey, I. (2010). Sensitivity and identifiability of stream flow generation parameters of the SWAT model. *Hydrological Processes: An International Journal*, 24(9), 1133-1148.

Crowley, T. J. (2000). Causes of climate change over the past 1000 years. *Science*, 289(5477), 270-277.

Cubasch, U., D. Wuebbles, D. Chen, M.C. Facchini, D. Frame, N. Mahowald, and J.-G. Winther, 2013: Introduction. In: *Climate Change 2013: The Physical Science Basis. Contribution of Working Group I to the Fifth Assessment Report of the Intergovernmental Panel on Climate Change* [Stocker, T.F., D. Qin, G.-K. Plattner, M. Tignor, S.K. Allen, J. Boschung, A. Nauels, Y. Xia, V. Bex and P.M. Midgley (eds.)]. Cambridge University Press, Cambridge, United Kingdom and New York, NY, USA.

Cunderlik, J. (2003). *Hydrologic model selection for the CFCAS project: assessment of water resources risk and vulnerability to changing climatic conditions*. Department of Civil and Environmental Engineering, The University of Western Ontario.

Da Silva, I. N., Spatti, D. H., Flauzino, R. A., Liboni, L. H. B., & dos Reis Alves, S. F. (2017). Artificial neural network architectures and training processes. In *Artificial neural networks* (pp. 21-28). Springer, Cham.

Devia, G. K., Ganasri, B. P., & Dwarakish, G. S. (2015). A review on hydrological models. *Aquatic procedia*, *4*, 1001-1007.

Dingman, S. L., (2002). Physical Hydrology. 2nd Edition. Prentice Hall, New Jersey, USA page: 646.

Douglas-Mankin, K. R., Srinivasan, R., & Arnold, J. G. (2010). Soil and Water Assessment Tool (SWAT) model: Current developments and applications. *Transactions of the ASABE*, 53(5), 1423-1431.

Duch, W., & Jankowski, N. (1999). Survey of neural transfer functions. *Neural Computing Surveys*, 2(1), 163-212.

Elgaali, E. A. (2005). *Modeling regional climate change impacts on available water for Agriculture*. Colorado State University.

Folland, C. K., Karl, T. R. & Salinger, M. J. (2002). Observed climate variability and change. *Weather*, 57(8), 269-278.

Gamoyo, M., Reason, C., Oburu, D. (2015) Rainfall variability over the East Africa coast. *Theoretical and Applied climatology*, 120(1-2): 311-322

Gan, T. Y., Ito, M., Hülsmann, S., Qin, X., Lu, X. X., Liong, S. Y. & Koivusalo, H. (2016). Possible climate change/variability and human impacts, vulnerability of drought-prone regions, water resources and capacity building for Africa. *Hydrological Sciences Journal*, 61(7), 1209-1226.

Gao, P., Li, P., Zhao, B., Xu, R., Zhao, G., Sun, W., & Mu, X. (2017). Use of double mass curves in hydrologic benefit evaluations. *Hydrological Processes*, 31(26), 4639-4646.

Gassman, P. W., Reyes, M. R., Green, C. H., & Arnold, J. G. (2007). The soil and water assessment tool: historical development, applications, and future research directions. *Transactions of the ASABE*, 50(4), 1211-1250.

Gebrechorkos, S. H., Hülsmann, S., & Bernhofer, C. (2019). Long-term trends in rainfall and temperature using high-resolution climate datasets in East Africa. *Scientific Reports*, 9(1), 1-9.

Githui, F., Gitau, W., Mutua, F., & Bauwens, W. (2009). Climate change impact on SWAT simulated stream flow in western Kenya. *International Journal of Climatology: A Journal of the Royal Meteorological Society*, 29(12), 1823-1834.

Gocic, M., & Trajkovic, S. (2013). Analysis of changes in meteorological variables using Mann-Kendall and Sen's slope estimator statistical tests in Serbia. *Global and Planetary Change*, 100, 172-182.

Hagemann, S., Chen, C., Clark, D. B., Folwell, S., Gosling, S. N., Haddeland, I., & Wiltshire, A. J. (2013). Climate change impact on available water resources obtained using multiple global climate and hydrology models. *Earth System Dynamics*, 4(1), 129-144.

Hamilton, S. K., Hussain, M. Z., Lowrie, C., Basso, B., & Robertson, G. P. (2018). Evapotranspiration is resilient in the face of land cover and climate change in a humid temperate catchment. *Hydrological Processes*, 32(5), 655-663.

Hayati, M., & Shirvany, Y. (2007). Artificial neural network approach for short term load forecasting for Illam region. *World Academy of Science, Engineering and Technology*, 28, 280-284.

Hendriks, S. L. (2015). The food security continuum: a novel tool for understanding food insecurity as a range of experiences. *Food security*, 7(3), 609-619.

Herrnegger, M., Stecher, G., Schwatke, C., & Olang, L. (2021). Hydroclimatic Analysis of Rising Water Levels in the Great Rift Valley Lakes of Kenya.

IPCC. (2007). Climate Change 2007: The Physical Science Basis. Contribution of Working Group I to the Fourth Assessment Report of the Intergovernmental Panel on Climate Change (Solomon et al). *Cambridge University Press, Cambridge, United Kingdom and New York, NY*, 93-217.

IPCC. (2012). Glossary of terms. In: Managing the Risks of Extreme Events and Disasters to Advance Climate Change Adaptation [Field, C.B., V. Barros, T. F. Stocker, D. Qin, D. J. Dokken, K. L. Ebi, M. D. Mastrandrea, K. J. Mach, G.-K. Plattner, S. K. Allen, M. Tignor, and P. M. Midgley (Eds.)]. A Special Report of Working Groups I and II of the Intergovernmental Panel on Climate Change.

IPCC. (2013). Climate Change 2013: The Physical Science Basis. Contribution of Working Group I to the Fifth Assessment Report of the Intergovernmental Panel on Climate Change [Stocker, T. F., D. Qin, G. K. Plattner, M., Tignor, S. K. Allen, J. Boschung, A. Nauels, Y. Xia, V. Bex and P.M. Midgley (Eds.)]. Cambridge University Press.

IPCC. (2014). Annex II: Glossary [Mach, K.J., S. Planton and C. von Stechow (Eds.)]. In: Climate Change 2014: Synthesis Report. Contribution of Working Groups I, II and III to the Fifth Assessment Report of the Intergovernmental Panel on Climate Change [Core Writing Team, R.K. Pachauri and L.A. Meyer (Eds.)]. IPCC, Geneva, Switzerland, pp. 117-130.

IPCC. (2018). Summary for Policymakers. An IPCC Special Report on the impacts of global warming of 1.5°C above pre-industrial levels and related global greenhouse gas emission pathways, in the context of strengthening the global response to the threat of climate change, sustainable development, and efforts to eradicate poverty. World Meteorological Organization, Geneva, Switzerland.

Ise, T., & Oba, Y. (2019). Forecasting climatic trends using neural networks: an experimental study using global historical data. *Frontiers in Robotics and AI*, *6*, 32.

Jha, M. K., & Singh, A. K. (2013). Trend analysis of extreme runoff events in major river basins of Peninsular Malaysia. *International Journal of Water*, 7(1-2), 142-158.

Jun, W., Lingyu, T., Yuyan, L., & Peng, G. (2017). A weighted EMD-based prediction model based on TOPSIS and feed forward neural network for noised time series. *Knowledge-Based Systems*, 132, 167-178.

Kendall, M. G. (1975). Rank correlation methods: 10 tab.

Kerandi, N. M., Laux, P., Arnault, J., & Kunstmann, H. (2017). Performance of the WRF model to simulate the seasonal and interannual variability of hydrometeorological variables in East Africa: a case study for the Tana River basin in Kenya. *Theoretical and Applied Climatology*, 130(1-2), 401-418.

Khashei, M., & Bijari, M. (2010). An artificial neural network (p, d, q) model for timeseries forecasting. *Expert Systems with Applications*, 37(1), 479-489.

Kılıç, Z. (2020). The importance of water and conscious use of water. *International Journal of Hydrology*, 4(5), 239-241.

Kingston, D. G. & Taylor, R. G. (2010). Sources of uncertainty in climate change impacts on river discharge and groundwater in a headwater catchment of the Upper Nile Basin, Uganda. *Hydrology and Earth System Sciences,* 14(7), 1297-1308.

Kishiwa, P., Nobert, J., Kongo, V., & Ndomba, P. (2018). Assessment of impacts of climate change on surface water availability using coupled SWAT and WEAP models: case of upper Pangani River Basin, Tanzania. *Proceedings of the International Association of Hydrological Sciences*, 378, 23.

Kişi, Ö. (2008). River flow forecasting and estimation using different artificial neural network techniques. *Hydrology Research*, 39(1), 27-40.

Kouchi, D. H., Esmaili, K., Faridhosseini, A., Sanaeinejad, S. H., Khalili, D., & Abbaspour, K. C. (2017). Sensitivity of calibrated parameters and water resource estimates on different objective functions and optimization algorithms. *Water*, *9*(6), 384-396.

Kuok, K. K., Harun, S., & Shamsuddin, S. M. (2010). Particle swarm optimization feedforward neural network for modeling runoff. *International Journal of Environmental Science & Technology*, 7(1), 67-78.

Kundu, P. M. (2007). *Application of remote sensing and GIS techniques to evaluate the impact of land use and land cover change on stream flows in River Njoro catchment in Eastern Mau-Kenya* (Doctoral Thesis, Egerton University, Kenya).

Lee, W. K., & Tuan Resdi, T. A. (2016). Simultaneous hydrological prediction at multiple gauging stations using the NARX network for Kemaman catchment, Terengganu, Malaysia. *Hydrological Sciences Journal*, 61(16), 2930-2945.

Liebscher, H. J. (2009). The role of hydrology in water resources management. *International Association of Hydrological Sciences*, pp. 1-6.

Li, Y., Wang, N., Liu, J., & Hou, X. (2017). Demystifying neural style transfer. *arXiv preprint arXiv:1701.01036*.

Li, F., Jackson, T. J., Kustas, W. P., Schmugge, T. J., French, A. N., Cosh, M. H., & Bindlish, R. (2004). Deriving land surface temperature from Landsat 5 and 7 during SMEX02/SMACEX. *Remote Sensing of Environment*, 92(4), 521-534.

Liu, J. (2013). *Radial Basis Function (RBF) neural network control for mechanical systems: design, analysis and MATLAB simulation*. Springer Science & Business Media.

Loucks, D. P., & Van Beek, E. (2017). *Water resource systems planning and management: An introduction to methods, models, and applications*. Springer.

Lyon, B., & DeWitt, D. G. (2012). A recent and abrupt decline in the East African long rains. *Geophysical Research Letters*, 39(2).

Ma, L., Ascough Ii, J. C., Ahuja, L. R., Shaffer, M. J., Hanson, J. D., & Rojas, K. W. (2000). Root zone water quality model sensitivity analysis using Monte Carlo simulation. *Transactions of the ASAE*, 43(4), 883.

Mainuri, Z. G., & Owino, J. O. (2013). Effects of land use and management on aggregate stability and hydraulic conductivity of soils within River Njoro Watershed in Kenya. *International Soil and Water Conservation Research*, 1(2), 80-87.

Mango, L. M., Melesse, A. M., McClain, M. E., Gann, D., & Setegn, S. (2011). Land use and climate change impacts on the hydrology of the upper Mara River Basin, Kenya: results of a modeling study to support better resource management. *Hydrology and Earth System Sciences*, 15(7), 2245-2258.

Mann, H. B. (1945). Nonparametric tests against trend. *Econometrical: Journal of the Econometric Society*, 245-259.

Mati, B. M., Mutie, S., Gadain, H., Home, P., & Mtalo, F. (2008). Impacts of land□use/cover changes on the hydrology of the transboundary Mara River, Kenya/Tanzania. *Lakes & Reservoirs: Research & Management*, 13(2), 169-177.

Mbote, B. W. (2016). *Assessing the impacts of climate variability and climate change on biodiversity in Lake Nakuru, Kenya* (Doctoral dissertation, University of Nairobi, Kenya).

Mcsweeney, C., New, M., Lizcano, G., & Lu, X. (2010). The UNDP Climate Change Country Profiles: Improving the accessibility of observed and projected climate information for studies of climate change in developing countries. *Bulletin of the American Meteorological Society*, 91(2), 157-166.

Milly, P. C., Dunne, K. A., & Vecchia, A. V. (2005). Global pattern of trends in stream flow and water availability in a changing climate. *Nature*, 438(7066), 347-350.

Mishra, N., Soni, H. K., Sharma, S., & Upadhyay, A. K. (2018). Development and Analysis of Artificial Neural Network Models for Rainfall Prediction by Using Time-Series Data. *International Journal of Intelligent Systems & Applications*, 10(1).

Moriasi, D. N., Arnold, J. G., Van Liew, M. W., Bingner, R. L., Harmel, R. D., & Veith, T. L. (2007). Model evaluation guidelines for systematic quantification of accuracy in watershed simulations. *Transactions of the ASABE*, 50(3), 885-900.

Mukundan, R., Radcliffe, D. E., & Risse, L. M. (2010). Spatial resolution of soil data and channel erosion effects on SWAT model predictions of flow and sediment. *Journal of Soil and Water Conservation*, 65(2), 92-104.

Murshed, S. B., & Kaluarachchi, J. J. (2018). Scarcity of fresh water resources in the Ganges Delta of Bangladesh. *Water Security*, 4, 8-18.

Mwangi, H. M., Julich, S., Patil, S. D., McDonald, M. A., & Feger, K. H. (2016). Relative contribution of land use change and climate variability on discharge of upper Mara River, Kenya. *Journal of Hydrology: Regional Studies*, 5, 244-260.

Mwetu, K. K. (2010). *Modelling Responses of Hydrology to Land Use/Land Cover Change and Climate Variability: A case of River Njoro Catchment of Kenya* (Doctoral Thesis, University of Natural Resources and Applied Sciences, Vienna).

Mwetu, K. K. (2019). Influence of Land Cover Changes and Climatic Variability on Discharge Regime of Njoro River Catchment in Kenya. *Open Access Library Journal*, 6(7), 1-22.

Narsimlu, B., Gosain, A. K., Chahar, B. R., Singh, S. K., & Srivastava, P. K. (2015). SWAT model calibration and uncertainty analysis for stream flow prediction in the Kunwari

River Basin, India, using sequential uncertainty fitting. *Environmental Processes*, 2(1), 79-95.

Nastos, P. T., Paliatsos, A. G., Koukouletsos, K. V., Larissi, I. K., & Moustris, K. P. (2014). Artificial neural networks modeling for forecasting the maximum daily total precipitation at Athens, Greece. *Atmospheric Research, 144*, 141-150.

Neitsch, S. L., Arnold, J. G., Kiniry, J. R., & Williams, J. R. (2011). *Soil and water assessment tool theoretical documentation version 2009*. Texas Water Resources Institute.

New, M., Hewitson, B., Stephenson, D.B., Tsiga, A., Kruger, A., Manhique, A., Gomez, B., Coelho, C.A.S., Masisi, D.N., Kululanga, M.E., Adesina, F., Saleh, H., Kanyanga, J., Adosi, J., Bulane, L., Fortunata, L., Mdoka, M.L., Lajoie, R., (2006). Evidence of trends in daily climate extremes over Southern and West Africa. *Journal of Geophysic Research*, 111, 1-1.

Nicholson, S. (2002). A review of climate dynamics and climate variability in Eastern Africa.

Nicholson, S. E. (2017). Climate and climatic variability of rainfall over eastern Africa. *Reviews of Geophysics*, 55(3), 590-635.

Noori, N. & Kalin, L. (2016). Coupling SWAT and ANN models for enhanced daily stream flow prediction. *Journal of Hydrology*, 533, 141-151.

Ochieng, Justus, Lilian Kirimi, and Mary Mathenge. "Effects of climate variability and change on agricultural production: The case of small scale farmers in Kenya." *NJAS-Wageningen Journal of Life Sciences* 77 (2016): 71-78.

Odongo, V. O., van der Tol, C., van Oel, P. R., Meins, F. M., Becht, R., Onyando, J., & Su, Z. (2015). Characterisation of hydroclimatological trends and variability in the Lake Naivasha basin, Kenya. *Hydrological processes*, 29(15), 3276-3293.

Omondi, P. A. (2010). *Teleconnections between decadal rainfall variability and global sea surface temparatures and simulation of future climate scenarios over East Africa* (Doctoral dissertation, University of Nairobi, Kenya).

Omondi, P., Awange, J. L., Ogallo, L. A., Okoola, R. A., & Forootan, E. (2012). Decadal rainfall variability modes in observed rainfall records over East Africa and their relations to historical sea surface temperature changes. *Journal of Hydrology*, 464, 140-156.

Omwoyo, M. A., Muthama, N. J., Opere, A., & Onwonga, R. (2017). Simulating Streamflow in Response to Climate Change in the Upper Ewaso Ngiro Catchment, Kenya. *Journal of Climate Change and Sustainability*, 1(2), 12-29.

Ongoma, V., & Chen, H. (2017). Temporal and spatial variability of temperature and precipitation over East Africa from 1951 to 2010. *Meteorology and Atmospheric Physics*, 129(2), 131-144.

Ongoma, V., Chen, H., & Gao, C. (2018). Projected changes in mean rainfall and temperature over East Africa based on CMIP5 models. *International Journal of Climatology*, 38(3), 1375-1392.

Ouyang, F., Zhu, Y., Fu, G., Lü, H., Zhang, A., Yu, Z., & Chen, X. (2015). Impacts of climate change under CMIP5 RCP scenarios on stream flow in the Huangnizhuang catchment. *Stochastic Environmental Research and Risk Assessment*, 29(7), 1781-1795.

Özbay, Y., & Tezel, G. (2010). A new method for classification of ECG arrhythmias using neural network with adaptive activation function. *Digital Signal Processing*, 20(4), 1040-1049.

Ozoegwu, C. G. (2019). Artificial neural network forecast of monthly mean daily global solar radiation of selected locations based on time series and month number. *Journal of Cleaner Production*, 216, 1-13.

Pachauri, R. K., Allen, M. R., Barros, V. R., Broome, J., Cramer, W., Christ, R., & van Ypserle, J. P. (2014). *Climate change 2014: synthesis report. Contribution of Working Groups I, II and III to the fifth assessment report of the Intergovernmental Panel on Climate Change* (p. 151). Ipcc.

Partal, T., & Kahya, E. (2006). Trend analysis in Turkish precipitation data. *Hydrological Processes: An International Journal*, 20(9), 2011-2026.

Pinto, D. B. F., da Silva, A. M., Beskow, S., de Mello, C. R., & Coelho, G. (2013). Application of the Soil and Water Assessment Tool (SWAT) for sediment transport simulation at a headwater watershed in Minas Gerais state, Brazil. *Transactions of the ASABE*, 56(2), 697-709.

Rao, A. R., Hamed, K. H., & Chen, H. L. (2003). Nonstationarities in hydrologic and environmental time series. *Springer Science & Business Media.* (Vol. 45).

Recha, J. W., Lehmann, J., Walter, M. T., Pell, A., Verchot, L., & Johnson, M. (2012). Stream discharge in tropical headwater catchments as a result of forest clearing and soil degradation. *Earth Interactions*, 16(13), 1-18.

Renner, M., Brust, K., Schwärzel, K., Volk, M., & Bernhofer, C. (2014). Separating the effects of changes in land cover and climate: a hydro-meteorological analysis of the past 60 yr in Saxony, Germany. *Hydrology and Earth System Sciences*, 18(1), 389-405.

Roderick, M. L., & Farquhar, G. D. (2011). A simple framework for relating variations in runoff to variations in climatic conditions and catchment properties. *Water Resources Research*, 47(12).

Ruiz, L. G. B., Cuéllar, M. P., Calvo-Flores, M. D., & Jiménez, M. D. C. P. (2016). An application of non-linear autoregressive neural networks to predict energy consumption in public buildings. *Energies*, 9(9), 684-696.

Rwigi, S. K. (2014). *Analysis of Potential Impacts of Climate Change and Deforestation on Surface Water Yields from the Mau Forest Complex Catchment s in Kenya* (Doctoral dissertation, University of Nairobi, Kenya).

Sabiiti, G. (2008). *Simulation of climate scenarios over the Lake Victoria basin using the PRECIS Regional Climate Model* (Doctoral dissertation, University of Nairobi, Kenya).

Schulte, J. A., Najjar, R. G., & Li, M. (2016). The influence of climate modes on stream flow in the Mid-Atlantic region of the United States. *Journal of Hydrology: Regional Studies*, 5: 80-99.

Schulze, R. E. (2011). Approaches towards practical adaptive management options for selected water-related sectors in South Africa in a context of climate change. *Water SA,* 37*(5),* 621-646.

Schuol, J., Abbaspour, K. C., Srinivasan, R., & Yang, H. (2008). Estimation of freshwater availability in the West African sub-continent using the SWAT hydrologic model. *Journal of Hydrology*, 352(1-2), 30-49.

Senent-Aparicio, J., Jimeno-Sáez, P., Bueno-Crespo, A., Pérez-Sánchez, J., & Pulido-Velázquez, D. (2019). Coupling machine-learning techniques with SWAT model for instantaneous peak flow prediction. *Biosystems Engineering*, 177, 67-77.

Shumway, R. H., & Stoffer, D. S. (2017). ARIMA models. In *Time series analysis and its applications* (pp. 75-163). *Springer, Cham.*

Singh, A., Imtiyaz, M., Isaac, R. K., & Denis, D. M. (2014). Assessing the performance and uncertainty analysis of the SWAT and RBNN models for simulation of sediment yield in the Nagwa watershed, India. *Hydrological Sciences Journal*, 59(2), 351-364.

Skinner, J. (2019). *Global Warming Statistical Analysis.*

Somvanshi, V. K., Pandey, O. P., Agrawal, P. K., Kalanker, N. V., Prakash, M. R., & Chand, R. (2006). Modeling and prediction of rainfall using artificial neural network and ARIMA techniques. *Journal of Indian Geophysical Union*, 10(2), 141-151.

Teutschbein, C. (2013). *Hydrological modeling for climate change impact assessment: transferring large-scale information from global climate models to the catchment scale* (Doctoral dissertation, Department of Physical Geography and Quaternary Geology, Stockholm University).

Tomer, M. D., & Schilling, K. E. (2009). A simple approach to distinguish land-use and climate-change effects on watershed hydrology. *Journal of Hydrology*, 376(1-2), 24-33.

Tricoli, D. (2004). Use of gabions in small hydraulic works. *Website Tricardi (Italy)*.

Ummenhofer, C. C., Sen Gupta, A., England, M. H., & Reason, C. J. (2009). Contributions of Indian Ocean Sea surface temperatures to enhanced East African rainfall. *Journal of Climate*, 22(4), 993-1013.

UNEP. (2009). Climate Change Science Compendium 2009, edited by Mcmullen C.P.

Secretariat, U. N. F. C. C. C. (2005). Compendium on methods and tools to evaluate impacts of, and vulnerability and adaptation to, climate change. *Final Draft Report*.

Van Gerven, M., & Bohte, S. (2017). Artificial neural networks as models of neural information processing. *Frontiers in Computational Neuroscience*, 11, 114.

Van Liew, M. W., Arnold, J. G., & Garbrecht, J. D. (2003). Hydrologic simulation on agricultural watersheds: Choosing between two models. *Transactions of the ASAE*, 46(6), 1539.

Vishwakarma, V. P. (2012). A non-iterative learning based artificial neural network classifier for face recognition under varying illuminations. In: *International Conference on Contemporary Computing* (pp. 383-394). Springer, Berlin, Heidelberg.

Verma, O. (2020). Unit-12 Extreme Climate Events. IGNOU.

Wambua, R. M., Mutua, B. M., Nyaanga, D. M., & Kundu, P. M. (2008). Classification of catchment risk areas using spatially distributed event-based soil erosion: a case of Upper Njoro River catchment, Kenya. *International Journal of Design & Nature and Ecodynamics*, 3(4), 281-296.

Wang, Z. X., Zhao, Y. F., & He, L. Y. (2020). Forecasting the monthly iron ore import of China using a model combining empirical mode decomposition, non-linear autoregressive

neural network, and autoregressive integrated moving average. *Applied Soft Computing*, *94*, 106475.

(WMO) World Meteorological Organization. (2009). *Guide to hydrological practices, volume II management of water resources and application of hydrological practices*. Geneva, Switzerland: World Meteorological Organization.

(WMO) World Meteorological Organization. (2011). *Guide to climatological practices (WMO-No. 100)*. Geneva, Switzerland: World Meteorological Organization.

Xu, Y. P., Zhang, X., Ran, Q., & Tian, Y. (2013). Impact of climate change on hydrology of upper reaches of Qiantang River Basin, East China. *Journal of Hydrology*, 483, 51-60.

Yan, Z., Wang, S., Ma, D., Liu, B., Lin, H., & Li, S. (2019). Meteorological Factors Affecting Pan Evaporation in the Haihe River Basin, China. *Water*, 11(2), 317.

Yıldız, D. (2017). The importance of water in development. *World Water Diplomacy & Science News*, 10006(1-4), 1-7.

Zarrin, A. (2018). Climate Change; a Challenge for Sustainable Development. In *Water and Sustainable Development*.

Zhang, Q., Liu, J., Singh, V. P., Gu, X. & Chen, X. (2016). Evaluation of impacts of climate change and human activities on stream flow in the Jinghe basin, China. *Hydrological Processes*, 30(14), 2562-2576.

APPENDICES

APPENDIX A: TABLES

Table 1A: Stream flow data at 2FC05

Year	Jan	Feb	Mar	Apr	May	Jun	Jul	Aug	Sep	Oct	Nov	Dec	Sum
1970	0.16	0.08	0.59	2.27	3.37	1.77	0.6	1.53	1.39	0.82	0.42	0.12	13.12
1971	0.08	0.04	0.03	0.06	0.75	0.92	1.06	7.72	4.76	0.35	0.13	0.18	16.09
1972	0.14	0.46	0.21	0.04	0.05					0.11	0.72	0.12	1.853
1973	0.07	0.03	0.03	0.03	0.03		0.05	0.27	0.41	0.14	0.07		1.14
1974		0	0				1.43	0.41	0.94	0.44	0.35		3.579
1975		0.01	0.01	0.14	0.11	0.25					0.28	0.11	0.917
1976	0.04	0.03	0.02	0.03	0.03	0.03	0.35	0.87	0.97	0.14	0.05	0.05	2.613
1977	0.07	0.04	0.02	1.08	4.89	0.52	1.89	2.56	0.37	0.21	2.69	1.51	15.84
1978	0.98			1.93	1.08	0.68	1.42	1.54	1.82	0.77	0.62	0.63	11.47
1979							0.88	1.4	0.29		0.11	0.11	2.788
1980	0.07	0.05	0.04	0.07	1.16	0.28	0.24	0.08	0.06	0.03			2.071
1981							0.45	2.14		0.22	0.1	0.06	2.974
1982		0.05		0.01	0.24	0.24	0.04	0.72	0.34	0.28	1.72	3.83	7.463
1983	0.22	0.06					0.24	0.85	1.16	1.08	0.6	0.46	4.681
1984	0.17	0.03	0.02		0.01	0.01	0.08	0.04	0.01	0.02	0.03	0.02	0.455
1985		0.01	0.01	0.35	0.49	0.42	0.27			0.06	0.06	0.03	1.691
1986	0.02	0	0.01	0.02	0.07	0.08		0.18	0.51	0.09	0.01	0.09	1.077
1987	0.02	0	0.01	0.01	0.06	0.34	0.08	0.05	0.02	0	0.04	0.01	0.647
1988	0.02	0.01	0.01										0.038
1989			0.05	0.95	0.5	0.22	0.7	0.64	1.36	0.58	1.02		6.018
1990	2.96	0.18	0.38	5.26	1.41	0.36	0.17	0.11	0.11	0.1	0.07	0.08	11.18
1991	1.5	0.03	0.01	0.04	0.04	0.06	0.07	0.4	0.4	0.12	0.05	0.04	2.759
1992	0.01	0.01	0	0	0.03	0.05	0.06		0.28	0.19	0.3	0.11	1.045
1993	0.38	1.47	0.08	0.01	0.08	0.2		0.26	0.05	0.01	0.01	0.01	2.569
1994	0.01	0		0.05	0.05	0.12	0.96	2.06	0.65		0.75	0.46	5.1
1995	0.06	0.02	0.01	0	0.03	0.01	0.19	0.07	0.06		0.22	0.17	0.839
1996	0.08	0.06	0.04	0.02	0.02	0.05	0.28	0.76			0.08	0.08	1.456
1997	0.01			0.12	0.12			0.85	0.1	0.05	0.85	1.51	3.611
1998	5.75	2.62	0.33	0.12	5.49	0.9	0.6			1.37	0.57	0.1	17.86
1999	0.08	0.05	0.06	0.04	0.04								0.279

Table 2A: GPS points used for Geo-referencing in image classification

Latitude	Longitude	Description	Classified LULC
-0.489	35.878	Near Eastern Rift Escarpment	Forest
-0.468	35.922	Near Logomon	Forest & shrubs
-0.437	35.879	Above Nessuit center	Forest
-0.365	35.907	Beeston center	Bareland, shrubs & grassland
-0.3654	35.929	AGEN Depart EU weather station	Grassland& Buildings
-0.367	35.925	Keep left, Egerton University	Bareland & Buildings
-0.346	35.947	Farms opposite Njoro KARI	Agriculture
-0.330	35.943	Njoro town junction	Bareland & buildings
-0.327	35.921	Upper part of Njoro town	Agriculture
-0.301	35.988	Ngata besides River Njoro	Grassland & reparian
-0.283	36.061	Nakuru town roundabout	Buildings & bareland

Table 3A: GPS points used for Geo-referencing of stream digitization

Point		Description
Latitude	Longitude	
-0.321	36.072	Stream at 2FC16 river gauging station (Lake Nakuru)
-0.359	35.922	Stream at Botanic garden bridge
-0.338	35.944	River Njoro at the bridge near KARI
-0.371	35.941	Stream at 2FC19 river gauging station (Egerton bridge)
-0.371	35.924	Stream at 2FC05 river gauging station near Rivervier EU hostels
-0.375	35.933	River Njoro at Njokerio bridge
-0.374	35.927	River Njoro at Ahero bridge
-0.371	35.917	River Njoro at 2FC11 river gauging station (Little Shuru Tributary)
-0.394	35.913	River Njoro waterfall (at Njoro cave)
-0.402	35.913	Stream at River Njoro bridge on the main road from Nessuit
-0.428	35.859	At one of the tributary above Nessuit center

Table 4A: Precipitation MK trend results (Jan-Jun & Jul-Dec) in the period (1978-2017)

	S	Z_c	P-Value	Trend (at 95% level of significance)
Jan-Jun	-17	-0.19	0.8493	Dec & not Sig
Jul-Dec	216	2.51	0.0120	Inc & Sig

Dec: Decreasing; Inc: Increasing; Sig: Significant at $p < 0.05$-two tailed test

Table 5A: Monthly basis Catchment SWAT simulated values

Month	Rain (mm)	SURQ (mm)	LATQ (mm)	Water Yield (mm)	ET (mm)	PET(mm)
Jan	38.3	5	1.4	10.1	27.4	142.1
Feb	43.1	10.5	1.4	15.3	30.8	138.6
Mar	74.2	8.8	1.7	14.2	69.1	162.6
April	134.4	14.7	3.1	21.4	90.6	124.5
May	122.7	15.9	3.4	23.2	97.0	118.9
Jun	87.3	5.6	1.7	11.0	80.5	107.9
July	98.6	8.2	1.7	13.8	76.8	96.8
Aug	121.8	11.3	2.7	17.9	89.7	105.5
Sep	80.5	6.2	1.9	12.0	86.0	115.2
Oct	75.7	4.1	1.1	9.2	82.2	125.1
Nov	94.9	7.7	2.2	13.7	65.9	105.1
Dec	60.72	8.97	2.09	14.96	50.47	137.88

APPENDIX B: FIGURES

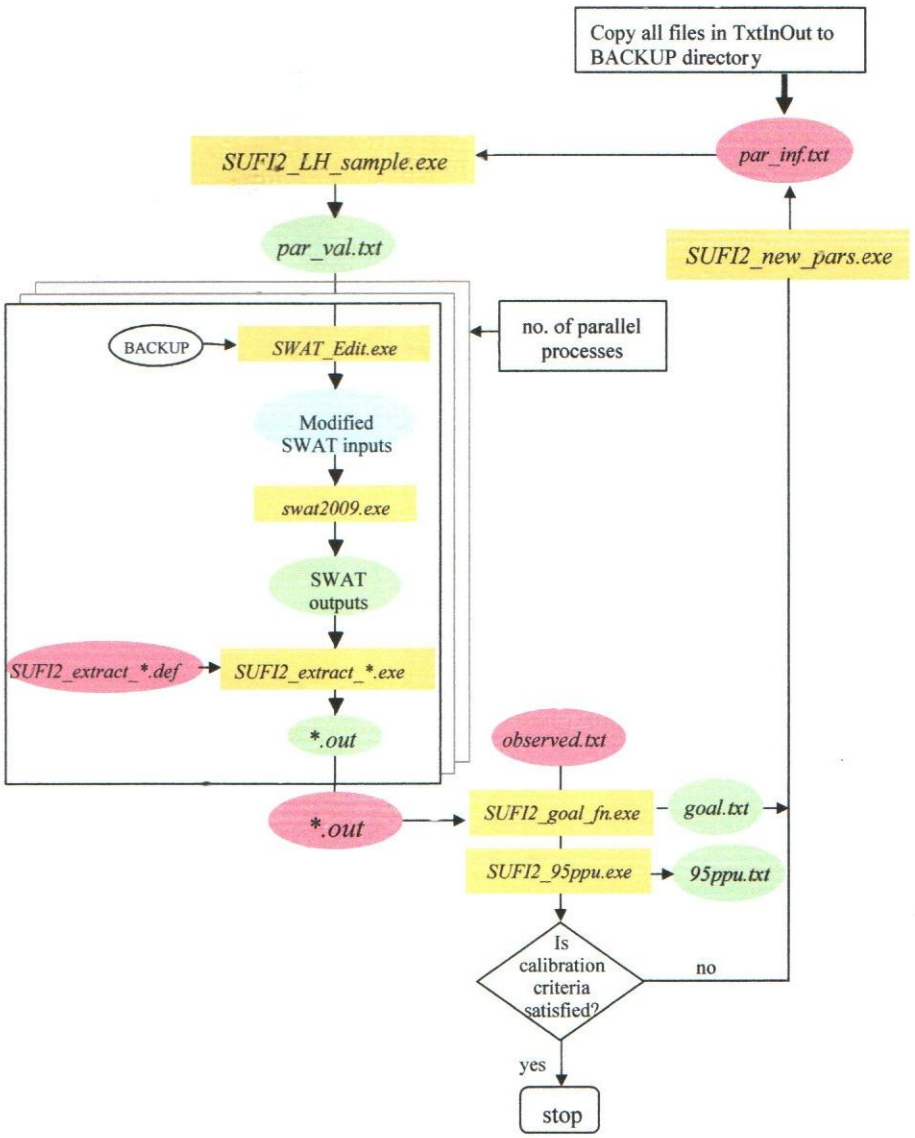

This figure is showing the link between SWAT (orange), iSWAT (green), and SUFI2 (yellow). The entire algorithm is run by two batch files: SUFI2_pre.bat and SUFI2_post.bat

Figure 1B: Flow chart of SWAT sensitivity analysis and calibration (Abbaspour *et al.*, 2015)

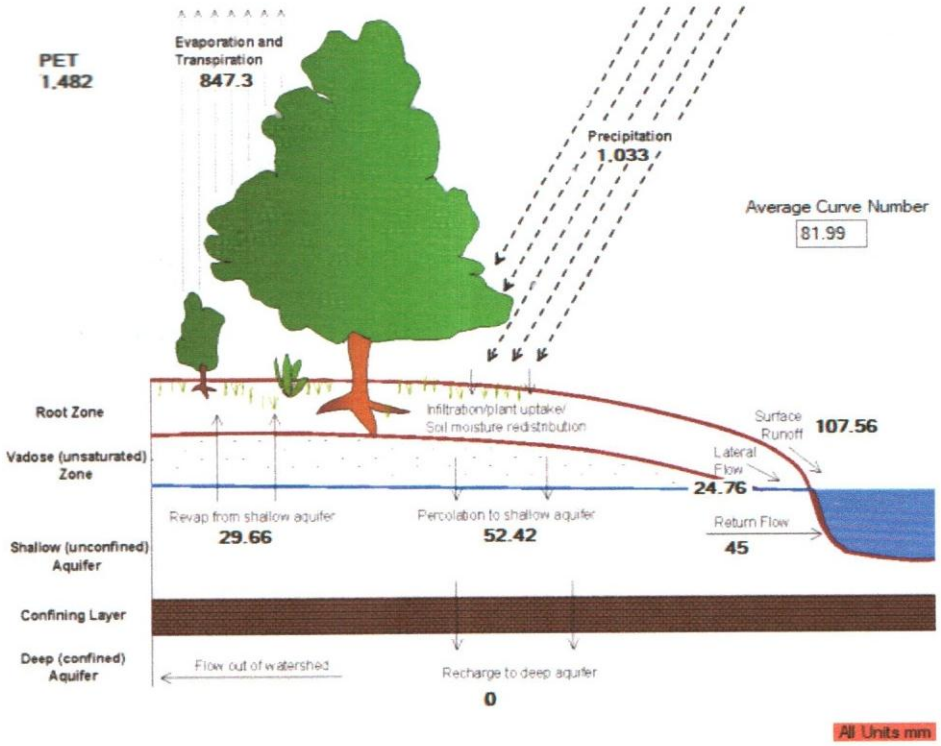

Figure 2B: Hydrologic processes simulated by SWAT for Njoro River catchment

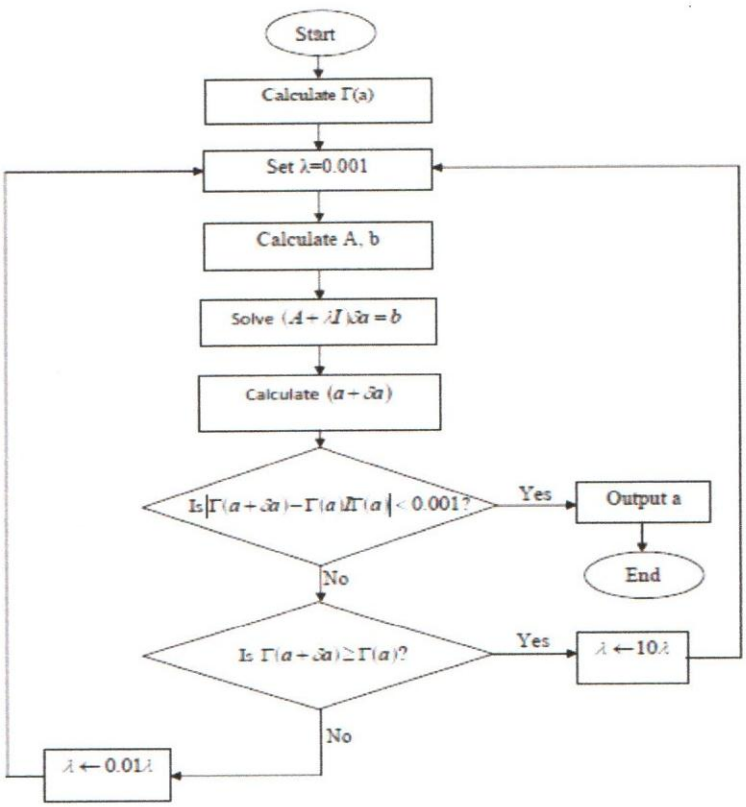

Figure 3B: Flow chart of Levernberg-Marquardt algorithm (Toushmalani, 2013)

APPENDIX C: Published Article and Research Permit

Appendix 1C: A Snapshot of the Abstract Page of the Published Paper

Modeling Climate Variability Influence on River Regime in Upper Njoro Catchment, Kenya

Edwin Otieno Amisi*, Peter Musula Kundu, Raphael Muli Wambua

Department of Agricultural Engineering, Egerton University, Nakuru, Kenya

Email address:
edwincamisi@gmail.com (E. O. Amisi)

*Corresponding author

To cite this article:
Edwin Otieno Amisi, Peter Musula Kundu, Raphael Muli Wambua. Modeling Climate Variability Influence on River Regime in Upper Njoro Catchment, Kenya. *Journal of Civil, Construction and Environmental Engineering*. Vol. 5, No. 5, 2020, pp. 126-137.
doi: 10.11648/j.jccee.20200505.14

Received: September 16, 2020; **Accepted**: October 5, 2020; **Published**: October 13, 2020

Abstract: To establish the effect of climate variability on annual discharge in Upper Njoro Catchment, hybrid models were developed by coupling Soil and Water Assessment Tool and Artificial Neural Networks. Daily surface runoff, lateral flow, and groundwater flow were first simulated with SWAT for the period (1978-1987) using climate variables from Egerton University weather station and LULC of 1978. The daily hydrologic variables simulated without calibration and validation of SWAT and observed discharge data were then used for ANN training, which led to the creation of discharge generation hybrid models for the dry, wet and wetter seasons. SWAT_ANN models generated discharges were compared with observed data and the performance rating were achieved at R^2 (0.94, 0.91, 0.92) and NSE (0.89, 0.87, 0.87) for DJFM, AMJJ, and ASON seasons respectively. SUFI-2 algorithm in SWAT-CUP was run separately to compare the performance of SWAT with that of SWAT_ANN. SWAT-CUP sensitivity analysis revealed satisfactory values of both the p-factor (0.61) and the r-factor (0.69). Calibration and validation of monthly streamflow were realized at R^2 (0.86 and 0.78) and NSE (0.83 and 0.74). The results showed that coupling SWAT and ANN improved flow prediction. Further, the potential of the SWAT_ANN modeling approach to separate the influence of climate variability on river regime from the effect of LULC was evaluated by comparing trends in the differences between observed and SWAT_ANN simulated monthly streamflow with trends of the quantified LULC changes. The findings provided sufficient evidence that the SWAT_ANN modeling approach was reliable and could also be applied to detect changes in LULC.

Keywords: Climate Variability, Land Use, River Regime, SWAT-CUP, SWAT, SWAT_ANN

Appendix 2C: Research License from NACOSTI

REPUBLIC OF KENYA

NATIONAL COMMISSION FOR SCIENCE,TECHNOLOGY & INNOVATION

Ref No: **260379**

Date of Issue: **11/February/2020**

RESEARCH LICENSE

This is to Certify that Mr.. EDWINE OTIENO AMISI of Egerton University, has been licensed to conduct research in Nakuru on the topic: EVALUATING CLIMATE VARIABILITY IMPACT ON SPATIO-TEMPORAL DISTRIBUTION OF STREAMFLOW IN RIVER NJORO CATCHMENT, KENYA for the period ending : 11/February/2021.

License No: **NACOSTI/P/20/3800**

260379

Applicant Identification Number

Director General
NATIONAL COMMISSION FOR SCIENCE,TECHNOLOGY & INNOVATION

Verification QR Code

NOTE: This is a computer generated License. To verify the authenticity of this document, Scan the QR Code using QR scanner application.